

**MIXING TIMES AND PHASE STATE WITHIN SECONDARY ORGANIC AEROSOL
IN THE TROPOSPHERE**

by

Adrian Mark Maclean

B.Sc., The University of Waterloo, 2015

A THESIS SUBMITTED IN PARTIAL FULFILLMENT OF
THE REQUIREMENTS FOR THE DEGREE OF

DOCTOR OF PHILOSOPHY

in

THE FACULTY OF GRADUATE AND POSTDOCTORAL STUDIES
(Chemistry)

THE UNIVERSITY OF BRITISH COLUMBIA
(Vancouver)

December 2020

©Adrian Mark Maclean, 2020

The following individuals certify that they have read, and recommend to the Faculty of Graduate and Postdoctoral Studies for acceptance, the dissertation entitled:

Mixing times and phase state within secondary organic aerosol in the troposphere

submitted by Adrian Maclean in partial fulfillment of the requirements for

the degree of Doctor of Philosophy

in Chemistry

Examining Committee:

Allan Bertram, Chemistry

Supervisor

Andrew MacFarlane, Chemistry

Supervisory Committee Member

Dan Bizzotto, Chemistry

University Examiner

Patrick Kirchen, Mechanical Engineering

University Examiner

Additional Supervisory Committee Members:

Mark Thachuk, Chemistry

Supervisory Committee Member

Mark MacLachlan, Chemistry

Supervisory Committee Member

Abstract

Physical properties such as phase state and the mixing times of water and organic molecules within secondary organic aerosol (SOA) are critical for predicting the formation, growth, and impact of SOA in the atmosphere. In the past, it has been assumed that SOA is liquid with rapid mixing times of water and organic molecules. However, recent laboratory measurements and field studies have shown that SOA may be semi-solid or solid in the atmosphere with long mixing times for certain conditions (i.e. low temperature and low relative humidity (RH)). Despite these recent measurements, the global distributions of phase state and mixing times within SOA are not well constrained. To address this knowledge gap, this thesis presents predictions of the global distribution of phase state and mixing times within SOA for the troposphere.

Global distributions of mixing times of organic molecules in SOA were predicted for the planetary boundary layer (PBL) for α -pinene SOA and sucrose-water particles based on literature viscosity data. The predicted mixing times in the PBL were fast, indicating the assumption of rapid mixing may be valid for this region of the atmosphere.

The viscosities of β -caryophyllene SOA were measured as a function of RH. These viscosities were used to calculate the mixing times of organic molecules in the SOA. Mixing times increased by 3-4 orders of magnitude as the RH decreased from 50 to 0%. However, the mixing times were rapid at RH values $\geq 15\%$, which indicated that β -caryophyllene SOA likely mixes rapidly in the PBL.

Finally, global distributions of phase states and mixing times of water and organic molecules were predicted based on room temperature viscosities for tree emission SOA and toluene SOA. Both of the SOA were predicted to be in a solid, glassy state in the upper troposphere with slow mixing times of water. Mixing times of organic molecules in SOA were predicted to be long in the middle and upper troposphere, with implications for the growth, formation, and impact of SOA in the atmosphere.

The results presented here increase our knowledge of the phase state and mixing times in SOA for the troposphere.

Lay Summary

Atmospheric aerosols impact climate, human health, visibility, and the long-range transport of pollutants. The effects of the aerosols depend on physical properties such as the aerosol phase state (i.e. liquid, semi-solid, or solid) and how quickly water and organic molecules mix within the aerosol particles. While these properties have been studied in the past, the distribution of these properties in the atmosphere has not been well defined. This thesis presents predictions of phase state and mixing times of water and organic molecules in several different types of aerosol particles. These results show that aerosols are expected to be liquid near the surface but become solid in the upper troposphere. In addition, mixing times of water and organic molecules in the aerosols are long in the middle and upper troposphere. These results improve the ability to predict the distribution of these properties in the atmosphere.

Preface

Chapter 3 is from a co-authored peer-reviewed journal article and Chapters 4 and 5 are co-authored work in preparation for submission as peer reviewed journal articles. The details of my specific contributions to each research chapter are below.

Chapter 3 (first author on a published journal article that was adapted for this thesis):

Maclean, A. M., Butenhoff, C. L., Grayson, J. W., Barsanti, K., Jimenez, J. L. and Bertram, A. K.: Mixing times of organic molecules within secondary organic aerosol particles: A global planetary boundary layer perspective, *Atmos. Chem. Phys.*, 17(21), 13037–13048, doi:10.5194/acp-17-13037-2017, 2017.

- Designed and formulated research aims with A. K. Bertram and J. L. Jimenez
- Developed parameterization used to predict viscosity and mixing times
- Prepared all figures in chapter
- Wrote the manuscript with A. K. Bertram
- Additional contributions from co-authors
 - C. L. Butenhoff provided the SOA concentrations as well as the RH and temperature fields from GEOS-Chem
 - C. L. Butenhoff, J. L. Jimenez and K. Barsanti also helped prepare the manuscript

Chapter 4 (first author on work submitted to ACS Earth and Space Chemistry): Maclean, A. M., Smith, N. R., Li, Y., Huang, Y., Hettiyadura, A. P. S., Crescenzo, G., Shiraiwa, M., Laskin, A., Nizkorodov, S. and Bertram, A. K.: Humidity-Dependent Viscosity of SOA From Ozonolysis of β -Caryophyllene: Measurements, Predictions, and Implications. Submitted to ACS Earth and Space Chemistry in October 2020.

- Formulated and designed research with A. K. Bertram
- Performed poke-flow measurements of β -caryophyllene SOA with Y. Huang and G. Crescenzo
- Performed analysis of experimental data
- Prepared figures for manuscript
- Wrote manuscript with A. K. Bertram

- Additional contributions from co-authors:
 - Y. Huang generated the β -caryophyllene SOA
 - Y. Huang and G. Crescenzo also analyzed experimental data
 - A. Hettiyadura and A. Laskin performed the mass spectrometry measurements
 - N. R. Smith and S. A. Nizkorodov analyzed the mass spectrometry data
 - Y. Li performed the calculations to predict viscosity based on mass spectrometry data
 - N. R. Smith also prepared figures for the manuscript
 - N. R. Smith, S. A. Nizkorodov, M. Shiraiwa, A. Laskin, and Y. Li also helped prepare the manuscript

Chapter 5 (first author on work in preparation for submission to a peer-reviewed journal):

Maclean, A. M., Li, Y., Smith, N., Crescenzo, G., Hettiyadura, A., Siemens, K., Faiola, C. L., Laskin, A., Nizkorodov, S., Shiraiwa, M. and Bertram, A. K.

- Formulated and designed research with A. K. Bertram
- Developed parameterization used to predict viscosity
- Prepared figures for manuscript
- Wrote manuscript with A. K. Bertram
- Additional contributions from co-authors:
 - G. Crescenzo performed poke-flow measurements to measure viscosity of healthy tree SOA
 - Data from previous study for comparison was provided by Y. Li and M. Shiraiwa
 - Y. Li and M. Shiraiwa also helped prepare the manuscript

Table of Contents

Abstract	iii
Lay Summary	iv
Preface	v
Table of Contents	vii
List of Tables	xi
List of Figures	xii
List of Symbols	xxi
List of Abbreviations	xxiii
List of Units	xxiv
Acknowledgements	xxv
Dedication	xxvii
Chapter 1: Introduction	1
1.1 Atmospheric aerosols.....	1
1.1.1 Aerosol formation and sources	1
1.1.2 Effects of aerosols on climate and health	2
1.2 Formation of secondary organic aerosol.....	3
1.3 Phase state of SOA.....	6
1.3.1 Importance of phase state of SOA	6
1.3.2 Previous studies on the phase state of SOA.....	6
1.4 Mixing time of water within SOA	7
1.4.1 Importance of the mixing time of water within SOA	7
1.4.2 Previous studies of mixing times of water	8
1.5 Mixing time of organic molecules	9
1.5.1 Importance of mixing time of organic molecules	9
1.5.2 Previous studies of mixing times of organic molecules.....	10
1.6 Overview of dissertation	11
Chapter 2: Viscosity and viscosity measurements.....	13
2.1 Viscosity	13
2.2 Viscosity measurements.....	14
2.2.1 Poke-flow technique for particle viscosity	14

2.2.2	Simulations of particle flow using COMSOL Multiphysics.....	17
Chapter 3: Mixing times of organic molecules within secondary organic aerosol particles: A global planetary boundary layer perspective		
3.1	Introduction.....	20
3.2	Materials and methods	21
3.2.1	Parameterization for the viscosity of α -pinene SOA as a function of temperature and RH	21
3.2.2	Parametrization for the viscosity of sucrose particles as a function of temperature and RH	24
3.2.3	Organic aerosol concentrations in the planetary boundary layer.....	25
3.2.4	RH and temperature in the PBL.....	26
3.3	Results and Discussion	27
3.3.1	Parameterization of viscosity and mixing times within α -pinene SOA particles as a function of RH and temperature.....	27
3.3.2	RH and temperature in the PBL.....	29
3.3.3	Mixing times of organic molecules within α -pinene SOA particles in the PBL..	31
3.3.4	Sensitivity analysis.....	34
3.3.5	Mixing times of organic molecules within anthropogenic SOA particles in the PBL	35
3.3.6	Comparison with previous studies	39
3.4	Summary and conclusions	40
Chapter 4: Humidity-dependent viscosity of SOA from ozonolysis of β -caryophyllene: Measurements, predictions, and implications.....		
4.1	Introduction.....	42
4.2	Experimental	44
4.2.1	SOA generation.....	44
4.2.2	Measurements of particle viscosity.....	45
4.2.3	Measurements of the chemical composition of SOA using mass spectrometry ...	48
4.2.4	Predictions of the viscosity of SOA from measurements of the chemical composition of the SOA.....	50
4.2.5	Prediction of viscosity using a mole-fraction based Arrhenius mixing rule.....	52

4.3	Results and discussion	53
4.3.1	Viscosity as a function of RH	53
4.3.2	Diffusion coefficients and mixing times of organic molecules within β - caryophyllene SOA as a function of RH.....	55
4.3.3	Chemical composition of the SOA based on mass spectrometry	58
4.3.4	Viscosity predictions from the measured chemical composition	60
4.3.5	Viscosity predictions from the mole-fraction based Arrhenius mixing rule.....	63
4.4	Summary and conclusions	65
Chapter 5: Global distribution of the phase state and mixing times within secondary organic aerosol particles in the troposphere based on room-temperature viscosity measurements		67
5.1	Introduction.....	67
5.2	Materials and methods	68
5.2.1	Parameterization for the viscosity of biogenic SOA as a function of RH and temperature	69
5.2.2	Parameterization for the viscosity of anthropogenic SOA as a function of RH and temperature	71
5.2.3	Predicting phase state and mixing times.....	72
5.2.4	Predicting phase state and mixing times from Shiraiwa et al. (2017b)	75
5.2.5	RH and temperature in the troposphere	76
5.3	Results and discussion	77
5.3.1	Parameterization of the viscosity, T_g/T , and mixing times of SOA particles as a function of temperature and RH.	77
5.3.2	Global distributions of the glass state.	79
5.3.3	Global distributions of water mixing times	80
5.3.4	Global distributions of organic mixing times	82
5.3.5	Possible reasons for the difference between the current results and Shiraiwa et al. (2017b).....	84
5.4	Summary and conclusions	85
Chapter 6: Conclusions and future work		88
6.1	Conclusions.....	88
6.1.1	Predicting mixing times of organic molecules in SOA in the troposphere.....	88

6.1.2	Room-temperature mixing times of organic molecules in SOA based on measured viscosities as a function of RH.....	89
6.1.3	Phase state and mixing time of water in SOA in the troposphere	89
6.2	Future work.....	90
References		92
Appendices.....		111
	Appendix A Appendix to Chapter 3	111
	A.1 Calculations of vertical profiles of temperature and RH in the boundary layer above Hyytiälä (boreal forest) and the Amazon (rainforest)	111
	A.2 Tables and figures.....	112
	Appendix B Appendix to Chapter 4.....	118
	B.1 OH reaction rates	118
	B.2 Mixing times of water within SOA	118
	B.3 Tables and figures.....	119
	Appendix C Appendix to Chapter 5.....	125
	C.1 Mole fraction-based viscosity mixing rule	125
	C.2 Viscosity of water as a function of temperature.....	125
	C.3 Figures.....	126

List of Tables

Table 5.1: Altitudes at which SOA reaches a glassy state, and altitude at which the mixing time of water and organics in SOA exceed 1 h.....	86
Table A.1: Room-temperature α -pinene SOA viscosity data from Grayson et al. (2016). Viscosity data corresponds to SOA generated with a mass concentration of $520 \mu\text{g m}^{-3}$	112
Table A.2: Low-temperature α -pinene SOA viscosity data from Järvinen et al. (2016). Viscosity data corresponds to SOA generated with a mass concentration of $707\text{-}1414 \mu\text{g m}^{-3}$	113
Table A.3: Liquid water viscosity data from Crittenden et al. (2012).	113
Table A.4: Initial guess parameters and fitting parameters used in Eq. 3.1 to predict the viscosity of α -pinene SOA as a function of temperature and RH. The fitting parameters were obtained by fitting Eq. 3.1 to the viscosity data listed in Tables A.1-A.3.....	113
Table A.5: Literature viscosity data used to create a parameterization for the viscosity of sucrose particles as a function of temperature and RH.....	114
Table A.6: Parameters from Zobrist et al. (2011) used in Eq. 3.5 to predict the weight fractions of sucrose and water in particles as a function of relative humidity.....	114
Table A.7: Fitting parameters used in Eq. 3.1 to predict the viscosity of sucrose particles as a function of temperature and RH. These parameters were obtained by fitting Eq. 3.1 to the viscosity data listed in Table A.6 as well as the guess values in the table.....	115
Table B.1: COMSOL parameters used when simulating the viscosity of β -caryophyllene SOA from poke-flow measurements	119
Table B.2: Calculated mixing times of water within the SOA particles ($\tau_{\text{mix,H}_2\text{O}}$) and experimental conditioning time for water vapor ($t_{\text{exp,H}_2\text{O}}$), which corresponds to the time the SOA particles were exposed to a given relative humidity before the poke-flow experiments. Viscosities are based on the upper limits of viscosity shown in Fig. 4.5 of the main text. Diffusion coefficients were calculated using the relation between viscosity and diffusion coefficients in sucrose-water from Price et al. (2016) (Eq. B.3). The variable d_p corresponds to the diameter of the SOA used in the poke-flow experiments.	120

List of Figures

Figure 1.1: Effective radiative forcing of atmospheric aerosols and greenhouse gases between 1750 and 2011. The values are based on estimations from both modelling and observations. The error bars represent the 90% confidence interval. The figure was adapted from Figure TS.6 from Stocker et al. (2013).....	3
Figure 1.2: Chemical structures of isoprene, α -pinene and β -caryophyllene.	4
Figure 1.3: Relative humidity (RH) and temperature change during an example atmospheric updraft. The starting RH and temperature conditions are dependent on the conditions in the atmosphere where the updraft starts. The mixing ratio of the water vapour is fixed and the temperature decreases at the dry adiabatic lapse rate.	7
Figure 1.4: Mixing times of water in SOA. Panel A shows slow mixing of water whereas panel B shows rapid mixing of water throughout the particle.....	8
Figure 1.5: Impact of mixing time of organic molecules within SOA on particle growth when exposed to a semi-volatile organic compound in the surrounding environment. Panel A shows particle growth with fast mixing and panel B shows particle growth with slow mixing.....	9
Figure 2.1: Laminar flow of a fluid between a 2-dimensional moving plate and a stationary plate.....	13
Figure 2.2: Diagram of the poke-flow experimental set-up.....	15
Figure 2.3: Optical images of a β -caryophyllene SOA particle taken during poke-flow experiments at a relative humidity of 48%. Image 1 was taken before the particle was poked. Image 2 was taken immediately after poking. Image 3 was taken during recovery and image 4 was taken at $\tau_{\text{exp, flow}}$ where the equivalent area diameter of the hole has decreased to 50% of its original size. The white scale bar in the pre-poking images corresponds to 50 μm . The circle in the centre of the particle in image 1 is an optical effect due to the hemispherical shape.	16
Figure 2.4: Geometry of the half-torus model used to simulate viscosity for the poke-flow experiments. Panel A shows the top view where R and r are the dimensions used to define the half-torus and panel B shows a side view. In panel B, surface 1 corresponds to the fluid-air interface, which can freely deform in all dimensions, and surface 2 corresponds to the fluid-substrate interface which can only deform parallel to the substrate surface.....	18

Figure 3.1: Temperature dependence of viscosity for strong and fragile glass-formers as T approaches T_g 23

Figure 3.2: Monthly averaged total organic aerosol concentrations (color scale) at the Earth’s surface in (a) January and (b) July, as calculated using GEOS-Chem. 26

Figure 3.3: Plot of RH vs temperature with contour lines representing (a) the viscosity parameterization for α -pinene SOA particles and (b) mixing times calculated for organic molecules within 200 nm diameter α -pinene SOA particles. The symbols in (a) represent the laboratory data used to develop the parameterization: squares represent the water viscosities from Crittenden et al. (2012); triangles represent the viscosity data of α -pinene SOA from Järvinen et al. (2016) and the circles represent the viscosity data from Grayson et al. (2016). The viscosity parameterization is based on α -pinene SOA generated using mass concentrations of $\sim 1000 \mu\text{g m}^{-3}$ 28

Figure 3.4: Six-hour normalized frequency counts of temperature and RH in the planetary boundary layer (PBL) (color scale) together with the mixing times for organic molecules within 200 nm α -pinene SOA particles (contours). Panel A shows the conditions for January and panel B shows the conditions for July. Mixing times (contours) are reported in hours. Frequency counts in the PBL were only included for the conditions where the mass concentration of total organic aerosol was $> 0.5 \mu\text{g m}^{-3}$ at the surface. The viscosity parameterization used to calculate mixing times was based on α -pinene SOA generated using mass concentrations of $\sim 1000 \mu\text{g m}^{-3}$ 30

Figure 3.5: Normalized frequency distributions of mixing times within α -pinene SOA in the planetary boundary layer (PBL). Black symbols correspond to January and red symbols corresponds to July. Frequency counts in the PBL were only included for the conditions where the mass concentration of total organic aerosol was $> 0.5 \mu\text{g m}^{-3}$ at the surface. The viscosity parameterization used to calculate mixing times was based on α -pinene SOA generated using mass concentrations of $\sim 1000 \mu\text{g m}^{-3}$ 31

Figure 3.6: RH, temperature and estimated mixing times for α -pinene SOA as a function of altitude for Hyytiälä (boreal forest) and the Amazon (rainforest). The temperature and RH at ground level are the average afternoon values in the driest month of the year for the respective locations. The vertical profiles of temperature and RH are plotted until the RH is 100 % for these locations. The height at which RH reaches 100 % is only slightly lower than the average height of the planetary boundary layer predicted by GEOS-5 meteorology data. For details see Section

A.1. The viscosity parameterization used to calculate mixing times was based on α -pinene SOA generated using mass concentrations of $\sim 1000 \mu\text{g m}^{-3}$ 32

Figure 3.7: Mixing times of organic molecules within 200 nm α -pinene SOA particles at the top of the planetary boundary layer as a function of latitude and longitude in (a) January and (b) July. The color scale represents mixing times. Mixing times are only shown for locations with total organic aerosol concentrations $> 0.5 \mu\text{g m}^{-3}$ at the surface. The viscosity parameterization used to calculate mixing times were based α -pinene SOA generated using mass concentrations of $\sim 1000 \mu\text{g m}^{-3}$ 33

Figure 3.8: Normalized frequency distributions of mixing times within 500 nm α -pinene SOA in the planetary boundary layer (PBL). Black symbols correspond to January and red symbols corresponds to July. Frequency counts in the PBL were only included for the conditions where the mass concentration of total organic aerosol was $> 0.5 \mu\text{g m}^{-3}$ at the surface. The viscosity parameterization used to calculate mixing times was based on α -pinene SOA generated using mass concentrations of $\sim 1000 \mu\text{g m}^{-3}$ 34

Figure 3.9: Normalized frequency distributions of mixing times within α -pinene SOA in the planetary boundary layer (PBL) for the parameterizations generated using the upper limit of the viscosity data from Grayson et al. (2016) and the upper RH limit from Järvinen et al. (2016). Blue symbols correspond to January and red symbols correspond to July. Frequency counts in the PBL were only included for the conditions where the mass concentration of total organic aerosol was $> 0.5 \mu\text{g m}^{-3}$ at the surface..... 35

Figure 3.10: Plot of RH vs temperature with contour lines representing (a) the viscosity parameterization for sucrose particles and (b) mixing times calculated for organic molecules within 200 nm diameter sucrose particles. The symbols in (a) represent the laboratory data used to develop the parameterization (Table A.5). Mixing times were calculated from the viscosity parameterization (Panel A) and Eq. 1.1 and 1.2. 36

Figure 3.11: Six-hour normalized frequency counts of temperature and RH in the planetary boundary layer (PBL) (color scale) together with the mixing times for organic molecules within 200 nm sucrose particles (as surrogates of anthropogenic SOA) (contours). Panels A and B show the conditions for January and July, respectively. Mixing times (contours) are reported in hours.

Frequency counts in the PBL were only included for the conditions when the mass concentration of total organic aerosol was $> 0.5 \mu\text{g m}^{-3}$ at the surface. 37

Figure 3.12: Normalized frequency distributions of mixing times within sucrose particles (as surrogates for anthropogenic SOA) in the planetary boundary layer (PBL). Red symbols correspond to January and blue symbols correspond to July. Frequency counts in the PBL were only included for the conditions where the mass concentration of total organic aerosol was $> 0.5 \mu\text{g m}^{-3}$ at the surface. The relatively large frequency count at 5×10^5 h is because all cases that had a viscosity greater than 10^{12} Pa s were assigned a value of 10^{12} Pa s. 38

Figure 3.13: Mixing times of organic molecules within 200 nm sucrose particles (as surrogates of anthropogenic SOA) at the top of the planetary boundary layer as a function of latitude and longitude. The color scale represents mixing times. Mixing times are only shown for locations with total organic aerosol concentrations $> 0.5 \mu\text{g m}^{-3}$ at the surface. Panels A and B correspond to January and July, respectively. 39

Figure 4.1: Chemical structure of β -caryophyllene. 43

Figure 4.2: Optical images of particles taken during poke-flow experiments at RH values of a) 48%, b) 28%, and c) 0%. Images a1, b1, and c1 correspond to images taken before the particle was poked. Images a2, b2, and c2 are images taken immediately after poking. Images a3, b3, and c3 are taken during recovery and images a4, b4, and c4 are taken at $\tau_{\text{exp, flow}}$ where the equivalent area diameter of the hole has decreased to 50% of its original size. The white scale bar in the pre-poking images corresponds to $50 \mu\text{m}$. The circle in the centre of the particle in b1 is an optical effect due to the hemispherical shape. 46

Figure 4.3: Viscosities as a function of particle conditioning time to the surrounding RH. Measurements were taken at RHs values of 48% in panel A, 28% in panel B, 15% in panel C, and 0% in panel D. 47

Figure 4.4: Particle 2-D projected area as a function of time during exposure to dry nitrogen flow with a secondary y-axis showing the percent change in projected particle area. The y-error bars correspond to the uncertainty in the measurement of the particle area in μm^2 . The straight line is a linear fit to the data and the shaded regions are the 95% confidence intervals for that fit. 48

Figure 4.5: Panel A shows the experimental flow time, $\tau_{\text{exp, flow}}$, for poked particles as a function of RH. Panel B shows simulated viscosities, diffusion coefficients and mixing times of organic

molecules in a 200 nm particle. The x-error bars correspond to uncertainties in the RH measurements and in panel B the y-error bars correspond to the upper and lower limits of the simulated viscosities at each RH and represent the uncertainties in the experimental flow times as well as the uncertainties in the parameters used to simulate the viscosities. The dotted line corresponds to a mixing time of 1 h. Also included in panel B are literature viscosity values for toluene SOA (Song et al., 2016a). Pictures of common substances have been added to panel B as points of reference per Koop et al. (2011). The tar pitch image is from the tar pitch experiment (image courtesy of Wikimedia Commons, GNU Free Documentation License, University of Queensland, John Mainstone). Panels C and D show the RH and temperature frequency distributions in the planetary boundary layer when the organic aerosol average concentration is $> 0.5 \mu\text{g m}^{-3}$ at the surface based on GEOS-Chem (Ullmann et al., 2019)..... 54

Figure 4.6: Viscosities of β -caryophyllene SOA and calculated mixing times within a 450 nm β -caryophyllene SOA particle. The y-error bars correspond to the upper and lower limits of the simulated viscosities at each RH and represent the uncertainties in the experimental flow times used to simulate the viscosity as well as the uncertainties in the parameters used to simulate the viscosities. The x-error bars correspond to uncertainties in the RH measurements. The horizontal line corresponds to a mixing time of 1 h..... 57

Figure 4.7: Total intensity of all molecular formula assignments based on carbon number for three ionization techniques (ESI, nano-ESI, and nano-DESI). In-source fragmentation resulted in increased abundance of smaller carbon compounds when using ESI and nano-ESI compared to nano-DESI..... 58

Figure 4.8: nano-DESI mass spectrum taken in positive mode (red spectrum) and negative mode (black spectrum). The signals were normalized to the highest intensity in each respective mode. The five most abundant peaks in each mode are labelled by the corresponding neutral (unionized) molecular formulas..... 60

Figure 4.9: Comparison of measured and predicted viscosities as a function of RH. The x-error bars correspond to uncertainties in the RH measurements, and the y-error bars correspond to the upper and lower limits of the simulated viscosities at each RH and represent the uncertainties in the experimental flow times used to simulate the viscosity as well as the uncertainties in the parameters used to simulate the viscosities. Panel A shows the viscosity predictions using the averaged positive and negative ion mode mass spectrometry data where it was assumed that the

weight fraction of the individual SOA species was proportional to the mass spectrum signal intensities (Eq. 4.3). Panel B shows the viscosity predictions using the averaged mass spectrometry data assuming a relation between weight fraction and intensity given in Eq. 4.13. 62

Figure 4.10: Measured viscosities and predicted viscosities using a mole-fraction based Arrhenius mixing rule. For the measurements, the x-error bars correspond to uncertainties in the RH, and the y-error bars correspond to the upper and lower limits of the simulated viscosities at each RH and represent the uncertainties in the experimental flow times used to simulate the viscosity as well as the uncertainties in the parameters used to simulate the viscosities. The uncertainties in the predictions are due to uncertainties in the hygroscopicity of the SOA. For the hygroscopicity, a range of CCN-derived kappa values of 0.04-0.001 was used (Asa-Awuku et al., 2009; Frosch et al., 2013). 64

Figure 5.1: Overview of method used to calculate the global distribution of SOA phase state and the mixing times of water and organics within SOA particles. 69

Figure 5.2: Log(viscosity) data from Smith et al. (2020) as a function of relative humidity for SOA produced via photooxidation of healthy tree emissions and the viscosity of pure water as well as a fit to the data using Eq. 5.1 and 5.2. The x-error bars represent uncertainties in the RH measurements and the y-error bars correspond to the 83% confidence interval for the upper and lower limit of viscosity. The points with upwards arrows correspond to data where only lower limits of viscosity were obtained. 70

Figure 5.3: Log(viscosity) data from Song et al. (2016a) as a function of relative humidity for SOA produced via the photooxidation of toluene and the viscosity of pure water as well as a fit to the data using Eq. 5.5. The x-error bars represent uncertainties in the RH measurements and the y-error bars correspond to the upper and lower limits of the viscosities. The point with an upwards arrow corresponds to data where only a lower limit of viscosity was obtained..... 72

Figure 5.4: Altitude profiles for a) temperature and b) relative humidity (RH) as a function of latitude calculated using the EMAC model for the years 2005-2009. 76

Figure 5.5: Parameterizations for viscosity (a, b), T_g/T (c, d), mixing time of water (e, f) and mixing time of organic molecules (g, h) as a function of temperature and RH for biogenic SOA (left-hand side) and anthropogenic SOA (right-hand side). The squares in panels (a, b) correspond to the viscosity of water as a function of temperature. Mixing times of water and organic molecules within SOA were calculated for 200 nm particles. 78

Figure 5.6: Annual average phase state of particles of a) biogenic SOA, b) anthropogenic SOA and c) SOA from Shiraiwa et al. (2017b) as a function of altitude and latitude. The particles are solid when $T_g/T > 1$ 79

Figure 5.7: Annual average altitude profiles of T_g/T for a) polar (latitude $>66.3^\circ$ and $<-66.3^\circ$), b) midlatitude ($66.3^\circ > \text{latitude} > 23.26^\circ$ and $-66.3^\circ < \text{latitude} < -23.26^\circ$) and c) tropical ($23.26^\circ > \text{latitude} > -23.26^\circ$) regions for biogenic SOA (red), anthropogenic SOA (black) and SOA from Shiraiwa et al. (2017b) (blue). 80

Figure 5.8: Annual average mixing time of water in a 200 nm particles for a) biogenic SOA, b) anthropogenic SOA and c) SOA for Shiraiwa et al. (2017b) as a function of altitude and latitude. The contour lines correspond to mixing times in hours. 81

Figure 5.9: Annual average altitude profiles of the mixing time of water in a 200 nm particle for a) polar (latitude $>66.3^\circ$ and $<-66.3^\circ$), b) midlatitude ($66.3^\circ > \text{latitude} > 23.26^\circ$ and $-66.3^\circ < \text{latitude} < -23.26^\circ$) and c) tropical ($23.26^\circ > \text{latitude} > -23.26^\circ$) regions for biogenic SOA (red), anthropogenic SOA (black) and SOA from Shiraiwa et al. (2017b) (blue). The vertical lines are included to highlight a mixing time of 1 h. Average mixing time values were calculated using the average of the log mixing time data as a function of latitude. 82

Figure 5.10: Annual average mixing time of organic molecules within SOA for a) biogenic SOA, b) anthropogenic SOA and c) SOA from Shiraiwa et al. (2017b) as a function of altitude and latitude. The contour lines correspond to mixing times in hours. 83

Figure 5.11: Annual average altitude profiles of the mixing time of organics in a 200 nm particle for a) polar (latitude $>66.3^\circ$ and $<-66.3^\circ$), b) midlatitude ($66.3^\circ > \text{latitude} > 23.26^\circ$ and $-66.3^\circ < \text{latitude} < -23.26^\circ$) and c) tropical ($23.26^\circ > \text{latitude} > -23.26^\circ$) regions for biogenic SOA (red), anthropogenic SOA (black), and SOA from Shiraiwa et al. (2017b) (blue). The vertical lines are included to highlight a mixing time of 1 h. Average mixing time values were calculated using the average of the log mixing time data as a function of latitude. 84

Figure A.1: Viscosities of different proxies of anthropogenic SOA as a function of RH. Data for toluene SOA taken from Song et al. (2016a). The data for sucrose-water mixtures was taken from Swindells (1958), Quintas et al. (2006), Telis et al. (2007), Forst et al. (2002), Migliori et al. (2007), Perry and Green (2008), and Power and Reid (2014). 115

Figure A.2: Monthly average relative humidity and temperature at the surface. Panels A and C correspond to January and panels B and D correspond to July. 116

Figure A.3: Monthly average relative humidity and temperature at the top of the planetary boundary layer. Panels A and C correspond to January, and panels B and D correspond to July. 117

Figure B.1: Schematic diagram of the UBC Environmental Chamber. There are sampling and measurement systems for ozone, temperature, relative humidity, and particle size distribution (scanning mobility particle sizer (SMPS) & optical particle counter (OPC)). 120

Figure B.2: The change of the ozone concentration inside the chamber with respect to time. Prior to a time of 0 h, the ozone concentration is at a steady state of approximately 325 ppb. At 0 h, the ozone injection is shut off, and the concentration of ozone starts to decrease afterwards. The ozone concentration drops to half of the initial value at approximately 1.5 h..... 121

Figure B.3: High-resolution mass spectrometry data taken with ESI, nano-ESI, and nano-DESI ionization sources in both positive and negative mode. The intensities were normalized to the largest peak within each ionization mode. 122

Figure B.4: Toluene SOA viscosity as a function of RH. The y-error bars correspond to the upper and lower limits of viscosity from the measurements. Shown in blue are the viscosity predictions based on nano-DESI positive mode mass spectrometry results from DeRieux et al. (2018) where it was assumed that the weight fraction of individual compounds was proportional to the mass spectrum signal intensity (Eq. 4.3). Shown in orange are the viscosity predictions from DeRieux et al. (2018) where a relation between weight fraction and intensity given in Eq. 4.13 of the main text was assumed. The shaded regions were calculated from nano-DESI mass spectrometry data collected at high and low RH separately (Hinks et al., 2018). 123

Figure B.5: Diesel fuel vapour SOA viscosities as a function of RH. The x-error bars correspond to uncertainties in the RH measurements and the y-error bars correspond to the upper and lower limits of viscosity at each RH from Song et al. (2019). Shown in blue are the viscosity predictions based on nano-DESI negative mode mass spectrometry results where it was assumed that the weight fraction of individual compounds was proportional to the mass spectrum signal intensity (Eq. 4.3). Shown in orange are the viscosity predictions where a relation between weight fraction and intensity given in Eq. 4.13 was assumed. 124

Figure C.1: Viscosity as a function of temperature for water fit using the VFT equation. Panel A shows the measured viscosities of water as a function of temperature from Hallett (1963) and Crittenden et al. (2012) and the red line is a fit to the data using Eq. C.5. Panel B shows the

difference between the measured values of viscosity and the predicted values from the VFT
equation (residuals)..... 126

List of Symbols

D	Diffusion coefficient
k	Boltzmann constant
T	Temperature
η	Viscosity
η_g	Viscosity at the glass transition
$\eta_{SOA,dry}$	Viscosity of dry SOA
η_{H2O}	Viscosity of pure water at 294 K
R_{diff}	Radius of the diffusing molecules
R_{matrix}	Radius of the matrix molecules
d_p	Diameter of the particle
τ_{mix}	Characteristic mixing time within an SOA particle due to diffusion
w	Weight fraction
w_{H2O}	Weight fraction of water
w_{suc}	Weight fraction of sucrose
k_{GT}	Gordon-Taylor constant
T_g	Glass transition temperature
$T_{g,SOA}$	Glass transition temperature of the dry SOA
$T_{g,suc}$	Glass transition temperature of sucrose
$T_{g,H2O}$	Glass transition temperature of water
n_{SOA}	Moles of SOA
n_{H2O}	Moles of water
i_{SOA}	van't Hoff factor
d	Diameter
A	Area
F	Force
m	Mass
v	Velocity
p	Momentum
t	Time
u	Flow velocity

τ	Stress tensor
P	Pressure
F_f	Force of friction
β	Slip length
$\tau_{exp, flow}$	Experimental flow time
M	Molecular weight
n_c	Number of carbon atoms
n_o	Number of oxygen atoms
n_H	Number of hydrogen atoms
I	Relative abundance in mass spectrum
m_{SOA}	Mass concentration of SOA
m_{H_2O}	Mass concentration of water
ρ_{SOA}	Density of SOA
ρ_{H_2O}	Density of water
a_w	Activity of water
κ	Hygroscopicity parameter
D_f	Fragility parameter
η_∞	Viscosity at infinite temperature
T_0	Vogel temperature
M_{SOA}	Molecular weight of SOA
M_{H_2O}	Molecular weight of water
D_0	Diffusion coefficient of a molecule in pure water
η_0	Viscosity of pure water
ζ	Fractional Stokes-Einstein exponent
H/C	Hydrogen to carbon ratio
D_{H_2O}	Diffusion coefficient of water
τ_{mix, H_2O}	Characteristic mixing time of water in an SOA particle due to diffusion
t_{exp, H_2O}	Experimental equilibration time
x_{SOA}	Mole fraction of SOA
x_{H_2O}	Mole fraction of water

List of Abbreviations

SOA	Secondary organic aerosol
CCN	Cloud condensation nuclei
PAH	Polycyclic aromatic hydrocarbon
SVOCs	Semi-volatile organic compounds
IVOC	Intermediate volatility organic compound
VOCs	Volatile organic compounds
RH	Relative humidity
O:C	Oxygen to carbon ratio
PBL	Planetary boundary layer
SMPS	Scanning mobility particle sizer
CPC	Condensation particle counter
OPS	Optical particle sizer

List of Units

h	hour
s	second
min	minute
Pa s	Pascal seconds
m	metre
cm	centimetre
km	kilometre
nm	nanometre
μm	micrometre
W	Watt
g	gram
μg	microgram
mol	mole
K	Kelvin
L	Litre
N	Newton
$^{\circ}$	degree
Da	Daltons

Acknowledgements

I am incredibly grateful to everyone who provided help and support over the past five years and made this dissertation possible.

I would like to start by thanking my PhD supervisor, Dr. Allan Bertram, for all of his thoughtfulness, knowledge and mentorship along the way. Thank you for giving me the space to experiment and troubleshoot as problems arose, but always being available when I needed it. You allowed me to pursue a variety of projects, both big and small, which allowed me to try different things and grow. I became a better scientist from working with Allan. I am incredibly grateful for all that you have done.

I would also like to thank all the members of the Bertram group, both past and present: Cedric, James, Kaitlin, Vickie, Meng, Stephen, Dagny, Erin, Yu, Jingwei, Kris, Yi, Yuanzhou, Soleil, Jesse, Shaun, Fabian and Anaand. Thank you for making the lab an enjoyable place to work, and all of the encouragement from everyone. I was able to collaborate with many members from the group and I learnt a great deal from them.

This work would not have been possible without the help of many other people at UBC. I would like to thank Dr. Saeid Kamal, who facilitated the work in the LASIR facility, helping me troubleshoot problems with the microscope or the data. I would also like to thank the staff from the UBC chemistry Mechanical and Electronics shops, who applied their expertise to many issues that arose during this work. The Chemistry administration staff and Chemistry Stores have also been a great deal of help.

Outside of UBC, I would like to thank all my collaborators. They provided knowledge and skillsets that strengthened this dissertation. They also provided different points of view and insights which helped my projects. I had the opportunity to work at Environment and Climate Change Canada for three months during my PhD work. I would like to thank Dr. Corinne Schiller for making this possible and for allowing me to gain experience in a non-academic setting. I would like to thank the whole team at Environment and Climate Change Canada for the welcoming atmosphere and everything they taught me while I was there.

I am extremely grateful to all of my friends who have supported me during this time. My friends have been a great source of fun and humor and have been a welcome distraction to help keep me grounded. In no particular order: Christina, Taylor, Ryan, Maria, Erin, Nicole, Paeton, Luke, Regina, Meng, Max, Vickie, Dagny, Calvin, Nick, James, Alyssa, Claire and others.

Thank you for the hikes, the camping trip, pub trivia, the board game nights, and the potlucks.
Thank you Allena for all the love and support to get this done.

My family has been one of my biggest supporters. Thank you to my brother, Nick, and both my parents for always believing that I could do this.

To my parents, Roger and Dinah, my brother, Nick, and my partner, Allena

Chapter 1: Introduction

1.1 Atmospheric aerosols

1.1.1 Aerosol formation and sources

Atmospheric aerosols are solid or liquid particles suspended in the atmosphere. Aerosols can be classified as either primary or secondary. Primary aerosols are directly emitted into the atmosphere whereas secondary aerosols are formed in the atmosphere via the oxidation of volatile compounds to form lower volatility products, which can then condense into the particle phase.

Aerosols originate from both natural and anthropogenic sources. Natural sources include wildfires, volcanic eruptions, and the oxidation of volatile compounds given off by plants (Seinfeld and Pandis, 2006). Anthropogenic sources include combustion of fossil fuels, agricultural activities, and industrial processes (Bauer et al., 2016; Seinfeld and Pandis, 2006).

The concentration of aerosols in the atmosphere varies both temporally and spatially. Aerosol concentrations can range from 10^2 - 10^6 particles cm^{-3} but are typically between 10^2 - 10^4 particles cm^{-3} in the troposphere (Seinfeld and Pandis, 2006). Concentrations of aerosols are generally highest in dense urban areas, lowest in remote and marine environments, and typically higher in the summer compared to the winter (Gallagher et al., 2011; Nguyen et al., 2016; Spracklen et al., 2010). The highest concentration of aerosols is found in the lowest part of the atmosphere, called the troposphere, which ranges from the Earth's surface to ~13 km in altitude. The bottom 1-2 km of the troposphere corresponds to planetary boundary layer (PBL) (Wallace and Hobbs, 2006) and the remainder of the troposphere corresponds to the free troposphere (FT). Vertical mixing of air masses within the PBL is rapid, on the order of 30 minutes (Wallace and Hobbs, 2006). Within the troposphere, the majority of the aerosol concentration is found within the PBL (Heald et al., 2011; Wagner et al., 2015).

The size of aerosols in the atmosphere can range from nanometers to tens of micrometers in diameter. The smallest particles are formed by homogeneous nucleation of semi-volatile gases in the atmosphere. These particles grow via coagulation with other aerosols or from the condensation of semi-volatile compounds onto existing particles and have short atmospheric lifetimes (< 1 h). Particles with diameters ranging from 100 nm to 2.5 μm are generally formed from the coagulation of smaller particles and have atmospheric lifetimes of days to weeks (Seinfeld and Pandis, 2006). The largest particles with diameters > 2.5 μm are typically formed

from mechanical processes and have atmospheric lifetimes of hours to days. Aerosol particles are typically removed from the atmosphere via wet and dry deposition. Aerosols containing volatile compounds can also lose mass to evaporation.

1.1.2 Effects of aerosols on climate and health

Atmospheric aerosols directly impact the climate by interacting with optical radiation, either via absorbing or scattering. Aerosols also indirectly impact the Earth's energy budget by serving as cloud condensation nuclei (CCN), which change the formation and properties of clouds (Stocker et al., 2013). For example, for two liquid clouds formed at identical water vapour concentrations, a cloud formed in a region with high concentrations of CCN will have smaller and more numerous water droplets than clouds formed at lower CCN concentrations. The smaller droplets will scatter more radiation and will increase the lifetime of the cloud because smaller droplets are less likely to precipitate. Some aerosols can serve as a nucleus for ice formation in the atmosphere, allowing for the formation of ice or mixed-phase clouds.

The magnitude of aerosols' impact on the climate is measured through the effective radiative forcing (Fig. 1.1). Effective radiative forcing is the difference between the energy of incoming solar radiation and outgoing radiation from the Earth, caused by a change in concentration of a climate stressor after allowing for adjustments in atmospheric temperatures, water vapour, and clouds caused by the concentration change (Stocker et al., 2013). Effective radiative forcing is measured in Watts per metre squared ($W m^{-2}$). A positive effective radiative forcing indicates the climate stressor has a warming effect whereas a negative effective radiative forcing indicates the climate stressor has a cooling effect.

Overall, the direct and indirect effect of aerosols are predicted to have a negative radiative forcing (Fig. 1.1). However, there is a large uncertainty in the radiative forcing of aerosols (Stocker et al., 2013). As a result, it is critical to gain more insight into the physical and chemical properties of aerosol particles to better understand their impact on the Earth's energy budget and reduce the associated uncertainty.

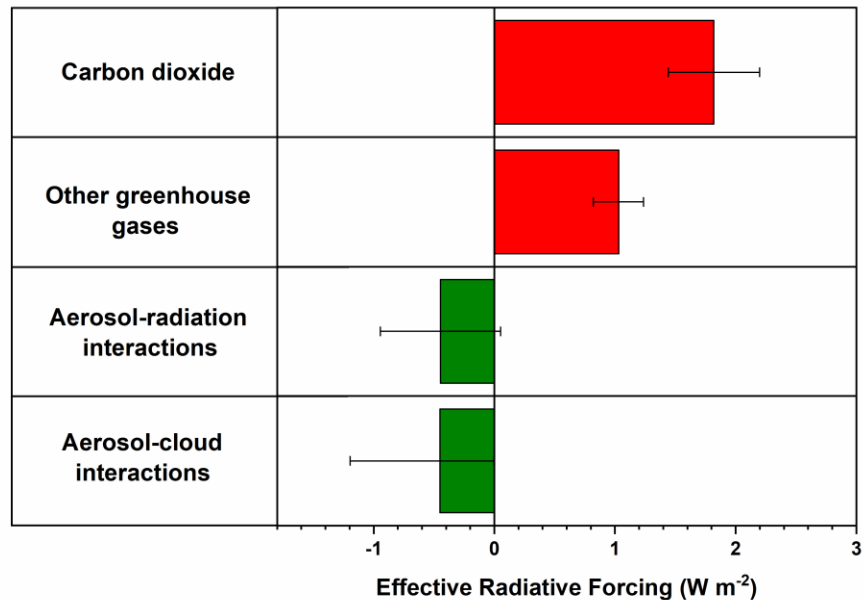


Figure 1.1: Effective radiative forcing of atmospheric aerosols and greenhouse gases between 1750 and 2011. The values are based on estimations from both modelling and observations. The error bars represent the 90% confidence interval. The figure was adapted from Figure TS.6 from Stocker et al. (2013).

Aerosols can also have detrimental effects on human health. Elevated aerosol concentrations have been associated with health problems such as cardiovascular disease and respiratory illnesses and have also been associated with an increase in daily mortality (Schwartz et al., 1996). Inhaled aerosols can deposit in the lungs and cause inflammation. The smallest particles (diameter < 0.1 μm) can pass through the lungs, enter the bloodstream, and travel to other organs such as the brain, resulting in adverse effects (Shiraiwa et al., 2017a).

Aerosols contribute to the long-range transport of pollutants such as polycyclic aromatic hydrocarbons (PAHs). During events such as forest fires where both PAHs and volatile aerosol precursors are emitted, the PAHs may become trapped inside the aerosol during particle formation (Zelenyuk et al., 2012). The PAHs can then be transported across long distances within the aerosol to remote locations such as the Arctic (Friedman et al., 2014).

1.2 Formation of secondary organic aerosol

This thesis focuses on secondary organic aerosol (SOA). SOA is formed when volatile organic compounds (VOCs) in the atmosphere are oxidized to form semi-volatile organic compounds (SVOCs) (Ervens et al., 2011; Hallquist et al., 2009). Oxidants include ozone and

OH radicals. Some of the products of these oxidation reactions can have sufficiently low volatility to partition into the particle phase forming SOA. SOA contributes significantly to the global particle concentration, contributing up to 70% of the mass of organic aerosols worldwide (Hallquist et al., 2009; Kanakidou et al., 2005).

Biogenic VOCs are emitted from a variety of sources such as trees and the ocean. Two of the most important types of biogenic VOCs are isoprene and terpenes. Terpenes are a class of compounds composed of unsaturated hydrocarbons containing two or more units of isoprene (C_5H_8). Examples of atmospherically relevant terpenes include α -pinene ($C_{10}H_{16}$), a monoterpene, and β -caryophyllene ($C_{15}H_{24}$), a sesquiterpene. Chemical structures for isoprene, α -pinene, and β -caryophyllene are given in Fig. 1.2. Emissions of isoprene are greater than emissions of monoterpenes and sesquiterpenes, making up ~49% of biogenic VOC emissions worldwide (Guenther et al., 2012). Monoterpenes are emitted in larger quantities compared to sesquiterpenes. However, sesquiterpenes are a major contributor to total SOA concentrations in several different regions (Bouvier-Brown et al., 2009; Sakulyanontvittaya et al., 2008; Yee et al., 2018). A dominant source of anthropogenic SOA precursors are alkanes and aromatic hydrocarbons such as benzene and toluene, which are produced during fossil fuel combustion (Gao et al., 2019; de Gouw et al., 2008). On a global scale, biogenic VOCs are the dominant contributor to SOA (Hallquist et al., 2009; Kanakidou et al., 2005).

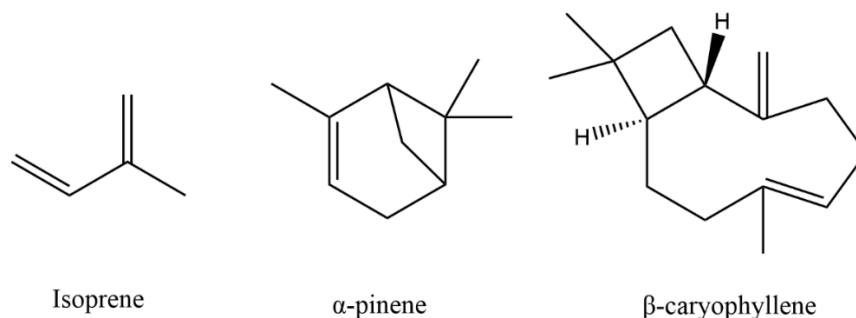


Figure 1.2: Chemical structures of isoprene, α -pinene and β -caryophyllene.

SOA is composed of thousands of different compounds due to the wide variety of VOC precursors in the atmosphere and the different possible oxidation pathways. It has been estimated that only 10-15 % of the organic species in aerosols have been identified (Hallquist et al., 2009; Prather et al., 2008). SOA contains molecules with a variety of functional groups including alcohols, ketones, and carboxylic acids (Alfarra et al., 2006; Forstner et al., 1997; Glasius et al.,

2000; Jang and Kamens, 2001; Jaoui and Kamens, 2003b; Larsen et al., 2001; Russell et al., 2011; Surratt et al., 2010). The average oxygen-to-carbon elemental ratio (O:C) of molecules in SOA generally ranges from 0.25-1 (Aiken et al., 2008; Cappa and Wilson, 2011; Dette et al., 2014; Jimenez et al., 2009; Ng et al., 2010).

The physical properties of the SOA depend on its chemical composition. An example of a chemical composition dependent parameter is hygroscopicity, which is the tendency for a substance to retain water. Consider two compounds with differing hygroscopicity exposed to the same relative humidity (RH). The less hygroscopic compound will absorb less water (thus having a lower water content) than the more hygroscopic compound. The hygroscopicity of SOA has been shown to vary with the type of VOC used to generate the aerosol (Asa-Awuku et al., 2009; Varutbangkul et al., 2006). As well, the hygroscopicity has been shown to change as the SOA is oxidized and aged (Berkemeier et al., 2014). Hygroscopicity of SOA is important as it impacts the water content in the aerosol particles. SOA will uptake water to remain in equilibrium with the water content of the surrounding gas phase or the RH. As a result, the water content of SOA will depend both on the external RH and the chemical composition of the particle.

Other important properties of SOA are the phase state (i.e. whether the SOA is a glass, semi-solid, or liquid) and the rate of mixing of water and organic molecules within the particles. These properties have been shown to depend on the chemical composition of the SOA (O:C ratio and molecular mass) and thus vary in SOA produced from different VOCs (DeRieux et al., 2018; Grayson et al., 2016, 2017; Rothfuss and Petters, 2017b). In addition, the phase state and rate of mixing of water and organic molecules in SOA are also influenced by the water content of the SOA and the atmospheric temperature.

It is difficult to predict the physical properties of SOA (such as phase state and mixing rates of water and organic molecules within the particles) due to its complex and variable composition. As a result, it is critical to perform laboratory studies measuring the physical properties of SOA and SOA proxies (compounds with similar functional groups, molecular weight and O:C ratios as SOA molecules). The results can then be used to test and make predictions of SOA properties in the atmosphere.

1.3 Phase state of SOA

1.3.1 Importance of phase state of SOA

An important property for predicting whether SOA can serve as a nucleus for ice formation in the atmosphere is the phase state. SOA can be in a glass state (viscosity $> 10^{12}$ Pa s), a semi-solid state (viscosity $> 10^2$ Pa s), or a liquid state (viscosity $< 10^2$ Pa s). A glass is an amorphous, non-crystalline solid lacking long-range order. Due to the complex mixture of compounds that make up SOA, it is not expected to form a crystalline solid and will instead form a glassy solid at low temperatures and low water content (Koop et al., 2011). The phase state of the SOA will be dependent on both temperature and RH. The temperature at which SOA, at a fixed composition, transitions to the glass state is the glass transition temperature (T_g). The T_g of SOA will vary based on the water content of the particle due to its plasticizing effect (Koop et al., 2011). Mixed phase particles can also form under certain conditions; however, the SOA is assumed to be a single phase for all calculations in this thesis.

Laboratory studies have shown that the surface of glassy particles can act as ice nuclei (Ignatius et al., 2016; Knopf et al., 2018; Murray et al., 2010; Wagner et al., 2012; Wang et al., 2012). As a result, information on the phase state of SOA is necessary to predict the formation of ice and mixed phase clouds in the atmosphere, and their subsequent effect on climate.

1.3.2 Previous studies on the phase state of SOA

In the past, it has been assumed that SOA in the atmosphere is in a liquid state (Hallquist et al., 2009; Jimenez et al., 2009; Pankow, 1994). However, it has been shown that SOA may be in a semi-solid or glassy state for some atmospherically relevant conditions (Virtanen et al., 2010), calling into question the validity of this assumption. The relationship between phase state and ice nucleating ability has been studied for SOA (Ignatius et al., 2016; Wang et al., 2012) and SOA proxies (Baustian et al., 2013; Murray et al., 2010; Wagner et al., 2012). Phase state has been directly investigated via bounce measurements (Bateman et al., 2015; Kidd et al., 2014; Pajunoja et al., 2015; Saukko et al., 2012b, 2012a; Virtanen et al., 2010), where SOA particles are impacted against a solid substrate to determine whether the particles will bounce off or stick to the substrate. Liquid particles stick to the substrate whereas semi-solid and solid particles are more likely to bounce. These measurements determine if the SOA is liquid or non-liquid but cannot distinguish between a semi-solid or glass state. The phase state has also been studied by

measuring glass forming properties and the glass transition temperature of a few components of SOA (Zhang et al., 2019b) and SOA proxies (Koop et al., 2011; Zobrist et al., 2008, 2011). Nevertheless, our understanding of the phase state of SOA under atmospheric conditions is far from complete. For example, measurement of the phase state has only been carried out for a relatively small number of SOA types at atmospheric temperatures and RHs. In addition, studies that have investigated the global distribution of phase states in the atmosphere are rare.

1.4 Mixing time of water within SOA

1.4.1 Importance of the mixing time of water within SOA

Another important parameter for predicting whether SOA will act as a nucleus for ice formation is the mixing time of water within the SOA, which determines whether SOA is in equilibrium with the water vapour in the surrounding air. Consider glassy SOA in a typical updraft, where temperature decreases, and RH increases (Fig. 1.3).

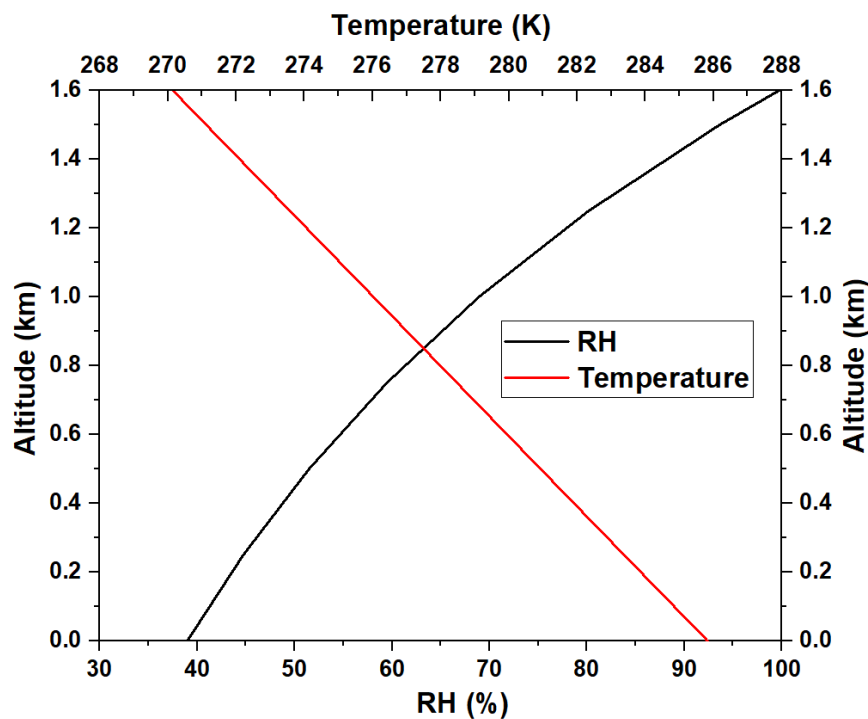


Figure 1.3: Relative humidity (RH) and temperature change during an example atmospheric updraft. The starting RH and temperature conditions are dependent on the conditions in the atmosphere where the updraft starts. The mixing ratio of the water vapour is fixed and the temperature decreases at the dry adiabatic lapse rate.

If the mixing of water within the SOA is slow (> 1 h) (Fig. 1.4a) then the glassy SOA core can persist and potentially cause ice nucleation when the supersaturation of water with respect to ice exceeds 1 (Berkemeier et al., 2014). However, if mixing of water is fast (< 1 s), the particle will maintain equilibrium with the surrounding RH during the updraft and quickly convert to a semi-solid or a liquid state (and thus not be expected to cause heterogeneous ice nucleation (Fig. 1.4b)). The timescales of atmospheric updrafts are on the order of 1 second to 1 hour (Berkemeier et al., 2014). If the mixing time of water is on the same timescale as the updraft, the lifetime of the glassy core as the RH changes will be more dependent on the updraft velocity (rate of change of temperature and RH in the updraft). The ice nucleating ability of glassy SOA becomes more important the longer the glassy SOA core persists. As a result, it is critical to understand the mixing times of water to properly predict when SOA particles can and cannot act as ice nuclei in the atmosphere.

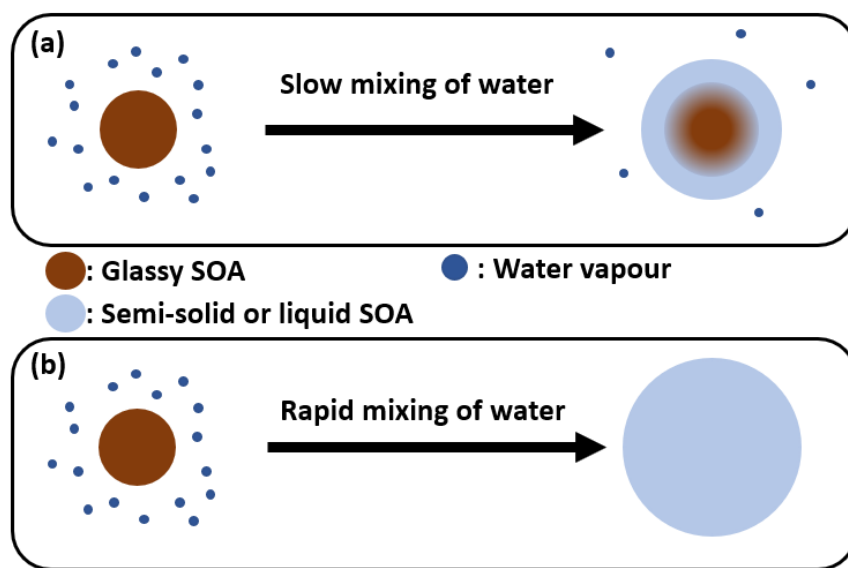


Figure 1.4: Mixing times of water in SOA. Panel A shows slow mixing of water whereas panel B shows rapid mixing of water throughout the particle.

1.4.2 Previous studies of mixing times of water

Measurements of water diffusivity for glassy organic particles used as proxies of SOA have shown that the glass state can inhibit the uptake and evaporation of water, slowing the particle from reaching equilibrium (Bones et al., 2012; Mikhailov et al., 2009; Tong et al., 2011). In addition, diffusion coefficients of water in SOA proxies (Price et al., 2014; Zobrist et al.,

2011) or SOA (Lienhard et al., 2015; Price et al., 2015) have been measured and show that mixing times of water can be slow (≥ 1 h) when SOA approaches the glass transition temperature compared to faster mixing times at higher temperatures (seconds or minutes). Studies extending these results to investigate the global distribution of water mixing times within SOA are rare.

1.5 Mixing time of organic molecules

1.5.1 Importance of mixing time of organic molecules

The time it takes for organic molecules to mix within the bulk of SOA is critical for accurately predicting factors such as growth rates, particle mass, and size distributions in the atmosphere. Mixing times of organic molecules determine whether SOA is in equilibrium with SVOCs in the surrounding air. If mixing times are fast, SVOCs can diffuse throughout the entire particle, and the concentration of the SVOC throughout the particle will quickly reach equilibrium with the concentration of the SVOC in the surrounding gas phase (Fig. 1.5a). Conversely, if mixing times are slow, the SVOCs cannot diffuse quickly throughout the bulk of the particle on short time scales assumed in models (< 1 h) (Hallquist et al., 2009), and so the SVOC concentration in the particle phase is more likely to be out of equilibrium with the concentration in the surrounding vapor (Fig. 1.5b).

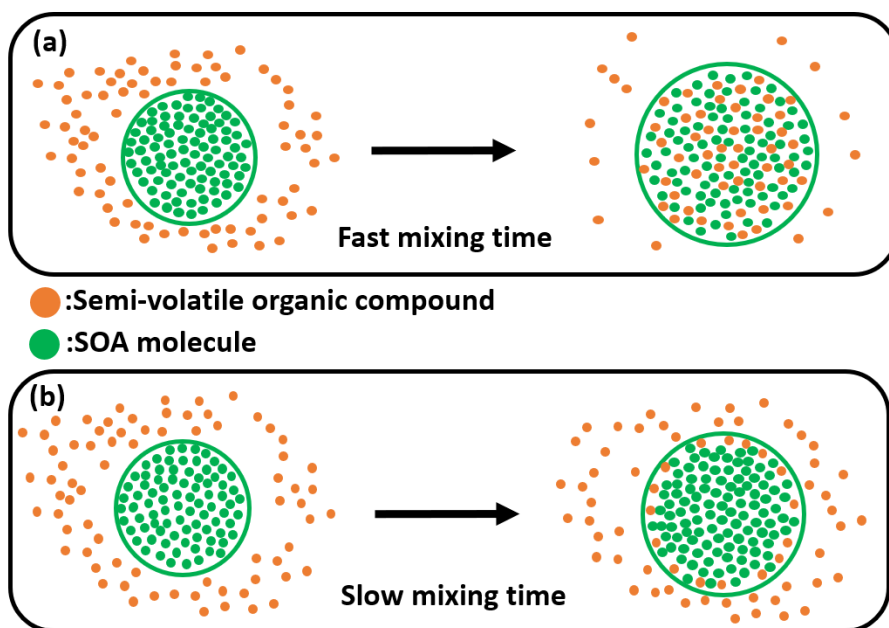


Figure 1.5: Impact of mixing time of organic molecules within SOA on particle growth when exposed to a semi-volatile organic compound in the surrounding environment. Panel A shows particle growth with fast mixing and panel B shows particle growth with slow mixing.

Mixing times of organic molecules also impact the reactivity within SOA. Consider a reaction constrained to the surface of the particles. When mixing times are rapid, the particle is well mixed and gas-phase oxidants can react with bulk phase molecules as they diffuse to the surface. However, when mixing times are slow, reaction rates will be slower, since gas phase oxidants cannot react with molecules in the bulk of the particle. An example of this is the reaction between ozone and pollutants, such as PAHs, embedded within SOA. PAHs have been detected in remote locations such as the Arctic at higher concentrations than local sources could account for, indicating they are being transported across long distances. Zhou et al. (2013) found that PAHs would rapidly degrade when contained in SOA with fast mixing times. However, when PAHs are contained in SOA with long mixing times the SOA shields the PAH molecules from ozone in the surrounding air, preventing the PAH from degrading (Zhou et al., 2013, 2019). In addition, a modelling study found that the only way to account for the PAH concentrations at remote locations was if they were being transported inside SOA with a high viscosity (and thus low diffusivity) (Zelenyuk et al., 2012).

1.5.2 Previous studies of mixing times of organic molecules

In the past it has been assumed that mixing times of organic molecules in SOA were short and that particles would reach equilibrium with the surrounding atmosphere on short times scales (< 1 h) (Hallquist et al., 2009). However, the recent research showing the SOA may be in a glass state has called the validity of this assumption into question.

Mixing times of organics in SOA have been measured directly by tracking the evaporation and absorption of SVOCs in SOA (Abramson et al., 2013; Ye et al., 2018). Another method to predict mixing times in SOA is to measure viscosity of SOA or diffusion coefficients of organic molecules in SOA. Viscosity measurements are converted into diffusion coefficients using the Stokes-Einstein equation:

$$D = \frac{kT}{6\pi\eta R_{diff}} \quad (\text{Eq. 1.1})$$

where k is the Boltzmann constant, T is the temperature, η is the viscosity and R_{diff} is the radius of the diffusing molecule.

Diffusion coefficients can be converted into characteristic mixing times of molecules with the SOA particle due to diffusion using the following equation (Seinfeld and Pandis, 2006):

$$\tau_{mix} = \frac{d_p^2}{4\pi^2 D} \quad (\text{Eq. 1.2})$$

where τ_{mix} is the mixing time, d_p is the diameter of the SOA particle and D is the diffusion coefficient of the diffusing molecule. The mixing time calculated with Eq. 1.2 corresponds to the time it takes for the concentration of the diffusing species at the centre of the particle to be approximately 1/e of the equilibrium concentration (~37%) for non-reactive partitioning (Zaveri et al., 2014). This approach has been used to predict mixing times in a variety of SOA (Grayson et al., 2016; Renbaum-Wolff et al., 2013; Shiraiwa et al., 2011, 2017b; Song et al., 2015, 2016a; Ullmann et al., 2019; Zhang et al., 2015) and SOA proxies (Evoy et al., 2019; Kiland et al., 2019; Rovelli et al., 2019; Song et al., 2016b) from viscosity or diffusion measurements. These studies have shown that mixing times of organic molecules in SOA can be long at room temperature and low RHs (Abramson et al., 2013; Grayson et al., 2016; Liu et al., 2016; Perraud et al., 2012; Renbaum-Wolff et al., 2013; Song et al., 2016a; Ye et al., 2016; Zhang et al., 2015).

While there have been several studies investigating mixing times of organic molecules in SOA, the majority have focused on SOA produced from a single VOC, while SOA in the atmosphere is far more complex. For biogenic SOA, the majority of studies have focused on SOA produced from isoprene and monoterpenes. In addition, the global distribution of mixing times of organic molecules in SOA has only been investigated in a few studies.

1.6 Overview of dissertation

Chapter 1 (current chapter) introduces atmospheric aerosols, SOA, phase state, and mixing times of water and organic molecules. In addition to providing necessary background, it provides the motivation for research chapters 3-5. Chapter 2 provides a definition for viscosity and describes the poke-flow technique combined with fluid simulations that is used to measure viscosity in Chapter 4. Chapter 3 describes the development of parameterizations to predict the viscosity and mixing time of organic molecules within α -pinene SOA and sucrose particles (a proxy for anthropogenic SOA), as a function of temperature and RH. The parameterizations were applied to atmospheric RH and temperature fields to predict the global distributions of viscosity and mixing times in the PBL. Chapter 4 describes viscosity measurements as a function of RH for SOA generated from the ozonolysis of β -caryophyllene, a sesquiterpene and an important biogenic VOC in the atmosphere. The viscosity of β -caryophyllene SOA has not been previously

studied as a function of RH. The measured viscosities were compared to predictions based on the chemical composition of the SOA determined with mass spectrometry. The viscosities were converted into mixing times of organic molecules to evaluate mixing in β -caryophyllene SOA in the PBL. Chapter 5 describes the development of parameterizations for viscosity, phase state, and mixing time of organic molecules and water in SOA generated via the photooxidation of tree emissions and SOA generated from the photooxidation of toluene. The parameterizations were applied to RH and temperature fields for the troposphere to predict global distributions of phase state and the mixing times of water and organic molecules within SOA. Finally, Chapter 6 summarizes the overall conclusions and suggests directions for future research into phase state and mixing times in SOA to improve knowledge of SOA properties and improve the accuracy of predictions of phase state and mixing times in SOA.

Chapter 2: Viscosity and viscosity measurements

2.1 Viscosity

Viscosity is the measurement of the resistance of a fluid to shear stress caused by intermolecular forces within the fluid (Viswanath et al., 2007). Viscosity is reported as either kinematic viscosity (ν) or dynamic viscosity (η), but this thesis will focus only on dynamic viscosity.

Dynamic viscosity is a measure of the tangential force required to move a layer of a fluid across another layer, measured in Pascal seconds (Pa s) (Viswanath et al., 2007). Consider a fluid film sandwiched between two 2D stationary plates (Fig. 2.1) (Viswanath et al., 2007). If the top plate is moved laterally at a constant velocity (v), it will exert a shear stress (σ) on the fluid. This will cause the top layer of the fluid to begin moving in the same direction as the plate. The velocity of the fluid layers decreases with increasing distance from the moving plate due to the resistance to flow between the layers of the fluid. The dynamic viscosity is related to the shear stress (σ) and the rate of change in the velocity with liquid depth ($\frac{dv}{dy}$) by the following equation:

$$\eta = \frac{\sigma}{\frac{dv}{dy}} \quad (\text{Eq. 2.2})$$

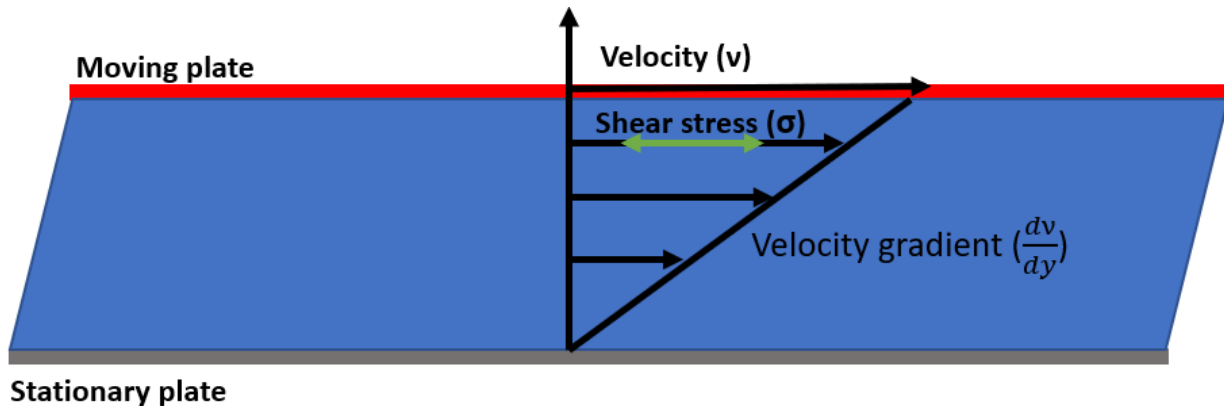


Figure 2.1: Laminar flow of a fluid between a 2-dimensional moving plate and a stationary plate.

The reason that this thesis focuses on dynamic viscosity is because diffusion of molecules within SOA is an atmospherically important process and dynamic viscosity can be converted into a diffusion coefficient assuming the validity of the Stokes-Einstein equation (Eq. 1.1). The

Stokes-Einstein equation assumes that the diffusing molecule experiences a continuous and homogenous fluid during diffusion. This can be achieved for a spherical molecule diffusing in a low viscosity matrix and when the radius of the diffusing molecule is larger than the matrix molecules. It has been shown to break down at high viscosities ($> 10^6$ Pa s) (Bastelberger et al., 2017; Chenyakin et al., 2017; Power et al., 2013). Nonetheless, it is able to predict diffusion coefficients in organic-water matrixes with reasonable agreement with measured diffusion coefficients when the radius of the diffusing molecule is larger than the radius of the matrix molecules and when the viscosity is between 10^{-3} and 10^6 Pa s (Evoy et al., 2020). It has been shown that the Stokes-Einstein equation is able to predict viscosities from diffusion coefficients of organic molecules in SOA generated from the ozonolysis of limonene (a monoterpene) (Ullmann et al., 2019) and is assumed to be applicable to other SOA as well.

2.2 Viscosity measurements

Viscosity is typically measured using viscometers such as capillary or rotational viscometers. These techniques cannot be used to measure the viscosity of SOA as these traditional viscometers require larger sample volumes than are available for laboratory or ambient SOA (typically 1-2 μ L of SOA material can be collected for reasonable timescales). Micro-viscometers have been developed that can handle much smaller sample volumes (Han et al., 2007; Rosencranz and Bogen, 2006; Srivastava and Burns, 2006), however the highest viscosity that these micro-viscometers can measure is on the order of 0.1-10 Pa s. The viscosity of SOA covers a wide range (10^{-3} - 10^{12} Pa s) and as a result, current micro-viscometers cannot be used. The poke-flow technique combined with fluid simulations was developed to measure the viscosity of samples with small volumes and high viscosities (Grayson et al., 2015; Renbaum-Wolff et al., 2013). This technique, which is detailed below, is used in Chapter 4 to measure the viscosity of SOA generated via the ozonolysis of β -caryophyllene.

2.2.1 Poke-flow technique for particle viscosity

The poke-flow technique is used along with fluid simulations to determine the viscosity of the collected SOA material at room temperature (292-294 K). This technique, which is based, in part, on early experiments by Murray et al. (2012), has been described and validated by Renbaum-Wolff et al. (2013) and Grayson et al. (2016). It has been validated using sucrose-

water solutions at several different water activities as well as polybutene viscosity standards (N450000 and N2700000; Cannon Instrument Company, USA) (Grayson et al., 2015).

For these experiments, the SOA is collected on a hydrophobic glass coverslip coated with Trichloro (1H,1H,2H,2H-perfluorooctyl) silane or FluoroPel 800 (Cytonix USA). The coverslip containing the SOA is mounted in a flow cell coupled to an optical microscope (Fig. 2.2).

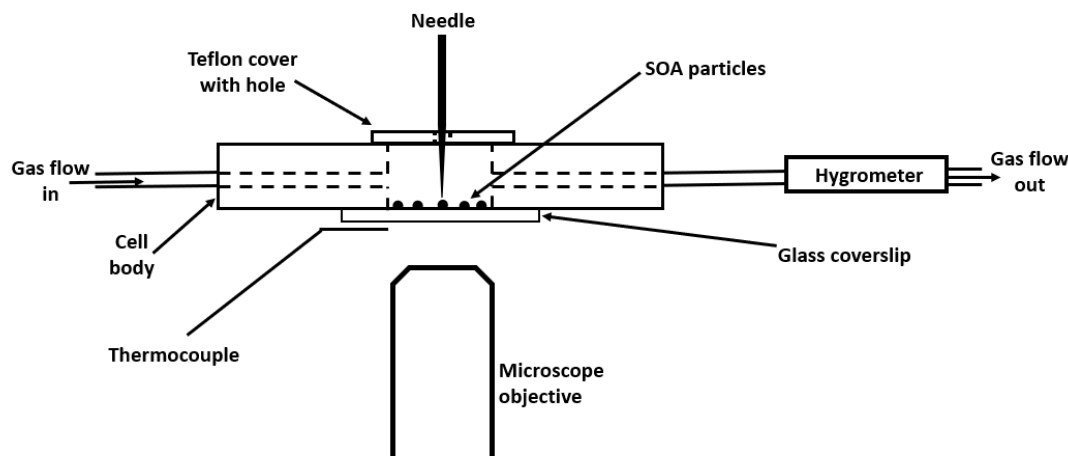


Figure 2.2: Diagram of the poke-flow experimental set-up.

The SOA within the flow cell is left to equilibrate to a chosen relative humidity (RH) for 2-24 h. Lower RHs require longer equilibration times. Viscosity is measured as a function of equilibration time to ensure the final viscosity does not change with conditioning time. In addition, once viscosity is determined from the fluid simulations, the mixing time of water is calculated at that viscosity to ensure the equilibration time was enough (see Section B.2 for more details on calculating the mixing time of water). The RH within the flow cell is controlled with a humidified flow of ultrapure N_2 (0.5 L/min). The N_2 gas flow first passes through a temperature-controlled water bath, which controls the RH. The RH is measured with a chilled mirror hygrometer (General Eastern model D-2), calibrated by measuring the deliquescence RH (DRH) of two different standards: ammonium sulphate (80% DRH based on Martin (2000)) and potassium carbonate (43% DRH based on Greenspan (1977)). The temperature of the cell is measured using a thermocouple probe in contact with the flow cell, calibrated using the temperature-controlled water bath.

In the experiments, the needle is aligned with the centre of the SOA particle ($\sim 10 \mu\text{m}$ for the tip of the needle) (Becton, Dickinson and Company, USA) with a micromanipulator. The

micromanipulator allows the needle to be moved in the x, y, and z direction. The needle is lowered and passes through the centre of the particle to touch the glass coverslip underneath. The needle is quickly raised out of the particle, leaving a hole. Prior to poking, the SOA particles have a spherical-cap geometry. After poking, the SOA material shape is changed to a half-torus geometry and slowly flows back to the spherical-cap geometry to reduce its surface energy (e.g. Fig. 2.3). Images are recorded of the SOA as it flows. Typical particle sizes used in the poke-flow experiment are 50-70 μm in diameter

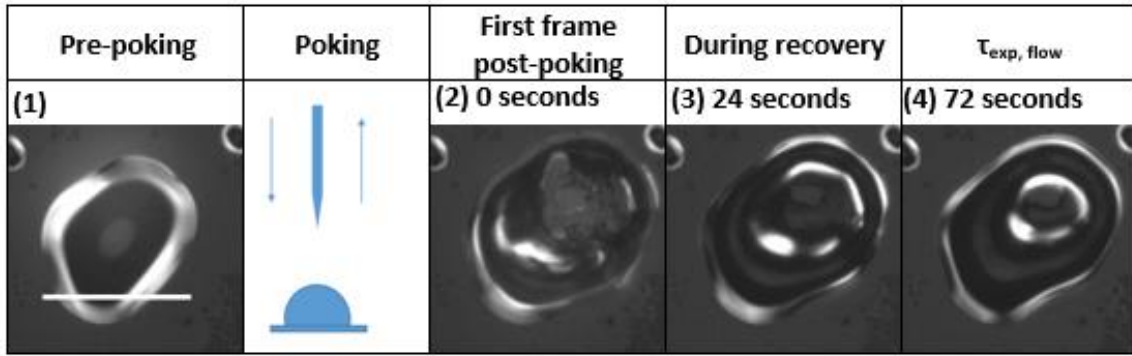


Figure 2.3: Optical images of a β -caryophyllene SOA particle taken during poke-flow experiments at a relative humidity of 48%. Image 1 was taken before the particle was poked. Image 2 was taken immediately after poking. Image 3 was taken during recovery and image 4 was taken at $\tau_{\text{exp, flow}}$ where the equivalent area diameter of the hole has decreased to 50% of its original size. The white scale bar in the pre-poking images corresponds to 50 μm . The circle in the centre of the particle in image 1 is an optical effect due to the hemispherical shape.

From images recorded during the poke-flow experiments, the experimental flow time $\tau_{\text{exp, flow}}$, defined as the time taken for the area of the hole in the half-torus geometry ($A_{\text{particle, hole}}$) to decrease to 25% of its original area, is determined. The value of $A_{\text{particle, hole}}$ is measured from the images using the microscope's software, Zen (Zeiss, <https://www.zeiss.com/microscopy/int/products/microscope-software/zen-lite.html>). Also measured from the images is the area of the entire particle including the hole (A_{particle}). The values for $A_{\text{particle, hole}}$ and A_{particle} are used to calculate the equivalent area diameter of the hole and the particle using the formula $d = \left(\frac{4A}{\pi}\right)^{\frac{1}{2}}$, where d is the equivalent area diameter of area A (Reist, 1992). The equivalent area diameter is the diameter of circle that has area A . The three parameters measured from the poke-flow

experiment used in the fluid simulations to determine viscosity are: the equivalent area diameter of the hole, the equivalent area diameter of the entire particle, and $\tau_{\text{exp,flow}}$.

2.2.2 Simulations of particle flow using COMSOL Multiphysics

The fluid simulations are carried out with a laminar two-phase flow with a moving mesh using the Microfluidics module of COMSOL Multiphysics (version 5.2a). The finite element method is used to approximate the flow in the simulations. The movement of the small, finite regions can be solved using simple equations which can then be used to approximate larger regions.

Fluid flow, in general, is governed by the Navier-Stokes equation, which for an incompressible fluid can be written in the form:

$$\rho \left(\frac{\partial u}{\partial t} + u \cdot \nabla u \right) = -\nabla P + \eta \nabla^2 u \quad (\text{Eq. 2.3})$$

where ρ is the density, u is the flow velocity, P is pressure and η is the viscosity. This equation is based on Newton's second law of motion and Newton's law of viscosity. The left-hand side of Eq. 2.3 corresponds to the product of mass and acceleration of the fluid. The right-hand side of Eq. 2.3 corresponds to all the forces acting upon the bulk of the fluid, including the frictional forces due to viscosity. In addition to the Navier-Stokes equation, other equations (i.e. boundary conditions) are solved simultaneously to take into account forces that apply to the boundaries rather than the entire fluid. An example of a surface force acting upon the fluid is the frictional force at the fluid-substrate interface (F_f):

$$F_f = \frac{-\eta u}{\beta} \quad (\text{Eq. 2.4})$$

where β is the slip length. The slip length defines the resistance to flow at the fluid-substrate interface, a larger slip length means less resistance to flow at the surface. A slip length of zero corresponds to a no-slip condition where the velocity of the fluid at the substrate is zero. Other boundary conditions include the force due to surface tension and the force due to the particle having the incorrect contact angle. COMSOL Multiphysics uses the Navier-Stokes equation, as well as the boundary conditions, to simulate the flow of a fluid.

The flow of the fluid is simulated using an arbitrary Lagrangian Eulerian method (ALE). The flow of individual volume elements of the fluid in the form of the mesh are modelled using Lagrangian flow. During the simulation, the mesh elements may become distorted, and the ALE

method will smooth the deformation of the mesh to ensure accurate results without the computational requirements of a pure Lagrangian method.

The $\tau_{\text{exp, flow}}$ values and equivalent area diameters of the hole and particle determined in the poke-flow experiments are converted to viscosities using fluid simulations of the SOA particle. The flow of the SOA material is simulated using a moving mesh consisting of ~ 5800 elements. The initial geometry in the simulations is a half-torus (Fig. 2.4a) consistent with the experiments. The dimensions of the half-torus are: R , the distance from the centre of the hole to the middle of the half torus ring, and r , the radius of the ring of the material. Shown in Fig. 2.4b are the two interfaces defined in the simulation. Interface 1 corresponds to the fluid-air interface and can deform in all directions. Interface 2 corresponds to the fluid-substrate interface and can only deform parallel to the substrate. In the simulations, the fluid flows axisymmetrically to fill the hole and return to the spherical cap shape.

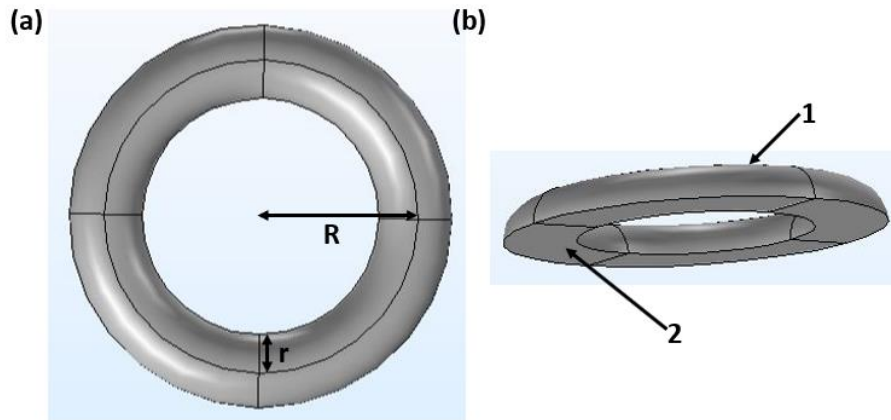


Figure 2.4: Geometry of the half-torus model used to simulate viscosity for the poke-flow experiments. Panel A shows the top view where R and r are the dimensions used to define the half-torus and panel B shows a side view. In panel B, surface 1 corresponds to the fluid-air interface, which can freely deform in all dimensions, and surface 2 corresponds to the fluid-substrate interface which can only deform parallel to the substrate surface.

The equivalent area diameter of the hole and the particle determined from the poke-flow experiment are used to calculate the values of R and r . The input values for the fluid simulations are R and r , $\tau_{\text{exp, flow}}$, and literature values of contact angle, surface tension, slip length, and density. The final input value for the simulations is the viscosity. From each simulation, the area of the hole at $\tau_{\text{exp, flow}}$, $A_{\text{model, flow}}$, is determined. The value of the input viscosity is varied until the

value of $A_{\text{model,flow}}$ at $\tau_{\text{exp,flow}}$ is $25\pm 1\%$ of the starting area of the hole (consistent with the definition of $\tau_{\text{exp,flow}}$).

To estimate the uncertainty in the extracted viscosity due to the input parameters, separate simulations are performed to determine upper and lower limits of viscosity based on a range of literature data for the contact angle, surface tension, slip length and density of the SOA. The upper and lower limits of viscosity from the simulations often differ by roughly 2 orders of magnitude. This uncertainty is the result of the range of possible input values for contact angle, surface tension, and slip length available in the literature. The viscosities simulated using the same literature values are typically within a factor of 2-7 of each other, meaning the variability in viscosity from particle to particle is low.

Chapter 3: Mixing times of organic molecules within secondary organic aerosol particles: A global planetary boundary layer perspective

3.1 Introduction

As outlined in Chapter 1, knowledge of the mixing time of organic molecules in SOA particles is important for predicting processes such as SOA formation, growth, and evaporation. When simulating these processes with chemical transport models, it is often assumed that semi-volatile organic compounds (SVOCs) are well mixed within SOA particles on the time scale of 1 h (Hallquist et al., 2009). If this assumption is invalid, chemical transport models could incorrectly predict SOA mass concentrations and size (Shiraiwa and Seinfeld, 2012; Zaveri et al., 2014). However, recent research has shown that mixing times of organic molecules within SOA particles can be > 1 h at room temperature and low relative humidities (RHs) (Abramson et al., 2013; Grayson et al., 2016; Liu et al., 2016; Perraud et al., 2012; Renbaum-Wolff et al., 2013; Song et al., 2016a; Ye et al., 2016; Zhang et al., 2015) and that proxies of SOA particles can form glasses at low RHs and low temperatures (Koop et al., 2011; Zobrist et al., 2008).

In the planetary boundary layer (PBL), the temperature varies from roughly 265 K to 305 K and the RH varies from roughly 20 % to 100 % (see below). This region of the atmosphere has rapid vertical mixing, on the order of 30 minutes, meaning that SOA may experience a wide range of RH and temperature conditions in a short period of time. Nevertheless, the conditions that lead to slow mixing times in SOA may be infrequent on a global scale in the PBL. If this is the case, then the assumption of well-mixed SOA particles in chemical transport models should be reasonable. Given that SOA concentrations are on average the highest in the PBL, properly modelling SOA in this region is important (Heald et al., 2011; Wagner et al., 2015). How often mixing times are > 1 h under ambient conditions in the PBL is not well constrained, in part due to the lack of information on mixing times of organic molecules in SOA particles as a function of both RH and temperature.

Recently it has been shown that the diffusion rates of organic molecules are slower in SOA from toluene photooxidation than SOA from α -pinene ozonolysis at room temperature (Liu et al., 2016; Song et al., 2016a; Ye et al., 2016). These results indicate that that mixing times are longer in some types of anthropogenic SOA than some types of biogenic SOA, at least at room temperature. SOA derived from anthropogenic sources can be a significant contributor over polluted regions (Hallquist et al., 2009; Spracklen et al., 2011).

In this chapter, parameterizations were developed for the viscosity of α -pinene SOA particles and sucrose particles (a proxy for anthropogenic SOA) as a function of both RH and temperature. As well, the distribution of RH and temperature in the PBL were determined from an archive of meteorological fields. The conditions in the PBL when SOA concentrations are significant were determined using a chemical transport model. Using the parameterizations and the conditions in the PBL, the frequency of mixing times of SVOCs > 1 h within α -pinene SOA and sucrose particles were quantified for ambient temperatures and RHs.

3.2 Materials and methods

3.2.1 Parameterization for the viscosity of α -pinene SOA as a function of temperature and RH

The following data was used to develop a parameterization of the viscosity of α -pinene SOA as a function of temperature and RH: a) room-temperature measurements of viscosity of SOA derived from α -pinene ozonolysis by Grayson et al. (2016) (Table A.1), b) low-temperature measurements of viscosity for SOA derived from α -pinene ozonolysis by Järvinen et al. (2016) (Table A.2), and c) temperature-dependent measurements of viscosity for water from Crittenden et al. (2012) (Table A.3). Järvinen et al. (2016) measured the RH range where α -pinene SOA had a viscosity of approximately 10^7 Pa s at different temperatures. In these experiments, SOA was generated with a mass concentration of 707-1414 $\mu\text{g m}^{-3}$. Grayson et al. (2016) measured viscosity of α -pinene SOA as a function of RH at 295 K. In these experiments, the SOA was generated with mass concentrations of 121 $\mu\text{g m}^{-3}$ and 520 $\mu\text{g m}^{-3}$. The viscosity measurements from Grayson et al. (2016) determined with a mass concentration of 520 $\mu\text{g m}^{-3}$ were used to be more consistent with the mass concentrations used by Järvinen et al. (2016). Although there are other room-temperature measurements of the viscosity of α -pinene SOA (Bateman et al., 2015; Hosny et al., 2016; Kidd et al., 2014; Pajunoja et al., 2014; Renbaum-Wolff et al., 2013), the room-temperature measurements from Grayson et al. (2016) were used because 1) viscosity was measured over a range of RHs in this study, 2) the mass concentrations used by Grayson et al. (2016) to generate the SOA were similar to the mass concentrations used by Järvinen et al. (2016), and 3) Grayson et al. (2016) measured the viscosity of the total SOA (both the water soluble component and the water insoluble component).

Due to the experimental conditions used by Grayson et al. (2016) and Järvinen et al. (2016), the parameterization developed here is applicable to SOA generated using a mass concentration of $\sim 1000 \mu\text{g m}^{-3}$.

To develop a parameterization for viscosity as function of temperature and RH, the following equation was fit to the measurements by Grayson et al. (2016), Järvinen et al. (2016), and Crittenden et al. (2012) (Table A.1-A.3):

$$\log(\eta) = 12 - \frac{C_1 * (T - \frac{w_{SOA} T_{g,SOA} + w_{H_2O} T_{g,H_2O} k_{GT}}{w_{SOA} + w_{H_2O} k_{GT}})}{C_2 + (T - \frac{w_{SOA} T_{g,SOA} + w_{H_2O} T_{g,H_2O} k_{GT}}{w_{SOA} + w_{H_2O} k_{GT}})} \quad (\text{Eq. 3.1})$$

where C_1 and C_2 are constants, k_{GT} is the Gordon-Taylor fitting parameter, $T_{g,SOA}$ and T_{g,H_2O} are the glass transition temperatures of dry SOA and water, and w_{SOA} and w_{H_2O} are the weight fractions of the dry SOA and water in the particles. The weight fractions of the dry SOA and water in the particles were determined from the RH using the following equation (Koop et al., 2011):

$$\frac{RH}{100} = \frac{1}{(1 + i_{SOA} \frac{n_{SOA}}{n_{H_2O}})} \quad (\text{Eq. 3.2})$$

where i is the dimensionless van't Hoff factor and n_{SOA} and n_{H_2O} are the number of moles of the SOA and water, respectively. A value of 1 was assumed for the van't Hoff factor (Koop et al., 2011) and a molecular weight for SOA of 175 g mol^{-1} (Huff Hartz et al., 2005).

Since the glass transition temperature of water is known (135 K) (Corti et al., 2008), the unknowns in Eq. 3.1 (and hence fitting parameters) were C_1 , C_2 , k_{GT} and $T_{g,SOA}$. The values for these parameters retrieved by fitting the equation to the viscosity data discussed above (using a least squares non-linear curve fitting function in Matlab) are reported in Table A.4.

Equation 3.1 was based on the Williams, Landel, and Ferry (WLF) equation and the Gordon-Taylor equation. The WLF equation provides an empirical relationship between viscosity and temperature:

$$\log\left(\frac{\eta}{\eta_g}\right) = \frac{-C_1(T - T_g)}{C_2 + (T - T_g)} \quad (\text{Eq. 3.3})$$

where C_1 and C_2 are fitting parameters, T is the temperature, T_g is the glass transition temperature, η is the viscosity and η_g is the viscosity at the glass transition (assumed to be 10^{12} Pa s).

The temperature dependence of the viscosity of a glass-forming fluid near the glass transition can be described as strong or fragile (Fig. 3.1) (Angell, 1991, 1995). A strong glass-former linearly relates $\ln \eta$ with T_g/T as T approaches T_g and is described as having Arrhenius behavior. A fragile fluid shows non-Arrhenius type behavior as T approaches T_g . The fitting parameters in the WLF equation account for the fragility of the fluid.

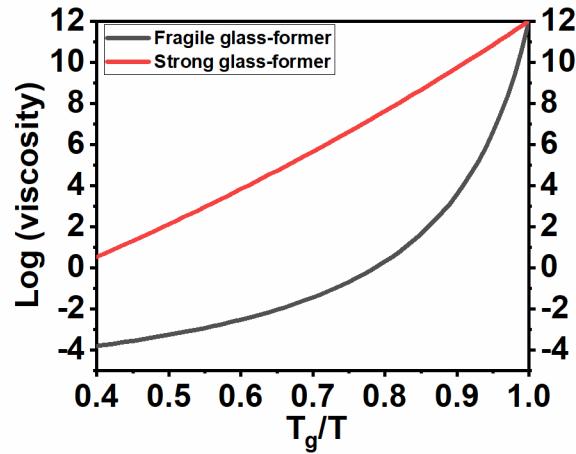


Figure 3.1: Temperature dependence of viscosity for strong and fragile glass-formers as T approaches T_g .

The Gordon-Taylor equation provides an empirical relationship between the glass transition temperature of a mixture and the weight fractions of its components. For a binary mixture of SOA and water it can be expressed as:

$$T_{g,mix} = \frac{w_{SOA}T_{g,SOA} + w_{H_2O}T_{g,H_2O}k_{GT}}{w_{SOA} + w_{H_2O}k_{GT}} \quad (\text{Eq. 3.4})$$

where $T_{g,mix}$ is the glass transition temperature of the SOA-water mixture, k_{GT} is the Gordon-Taylor fitting parameter, $T_{g,SOA}$ and T_{g,H_2O} are the glass transition temperatures of dry SOA and water, and w_{SOA} and w_{H_2O} are the weight fractions of the dry SOA and water in the particles. Equations 3.3 and 3.4 can be combined to give Eq. 3.1. Equation 3.3 (and hence Eq. 3.1) is valid only at or above the glass transition temperature. As a result, Eq. 3.1 was not used to predict viscosities $> 10^{12}$ Pa s (which corresponds to mixing times $> 5 \times 10^5$ h). If the temperature and RH in the PBL were such that the viscosity was greater than 10^{12} Pa s, the viscosity was assigned a value of 10^{12} Pa s and a mixing time of 5×10^5 hours. This assignment does not affect the conclusions in this manuscript since a mixing time of 5×10^5 hours is already well above the residence time of SOA particles in the atmosphere.

3.2.2 Parametrization for the viscosity of sucrose particles as a function of temperature and RH

Viscosities or diffusion rates within toluene SOA or other types of anthropogenic SOA have yet to be measured at temperatures lower than room temperature. As a result, sucrose was used as a proxy of anthropogenic SOA, since the viscosity of sucrose is similar to the viscosity of toluene SOA at room temperature (Fig. A.1) (Power and Reid, 2014; Song et al., 2016a), and since a parameterization of the viscosity of sucrose as a function of temperature and RH can be developed using literature data. While toluene SOA is assumed to be a proxy for anthropogenic SOA (Pandis et al., 1992; Robinson et al., 2013), anthropogenic SOA is likely more complex and can be from both aromatic and non-aromatic sources (Gao et al., 2019; de Gouw et al., 2008; Song et al., 2019).

A parameterization for the viscosity of sucrose was developed using: a) room-temperature viscosity data as a function of RH (Först et al., 2002; Migliori et al., 2007; Perry and Green, 2008; Power and Reid, 2014; Quintas et al., 2006; Swindells and States., 1958; Telis et al., 2007) (Table A.5), b) low-temperature viscosity data as a function of RH (Zobrist et al., 2008), and c) viscosity of water as a function of temperature (Crittenden et al., 2012).

To develop a parameterization as a function of RH and temperature, the sucrose viscosity data was fit to Eq. 3.1 using sucrose as the SOA. The weight fractions of dry sucrose and water in the particles were determined from the RH using the following equation (Zobrist et al., 2011):

$$\frac{RH}{100} = \frac{1+aw_{Suc}}{1+bw_{Suc}+cw_{Suc}^2} + (T - T^\theta)(dw_{Suc} + ew_{Suc}^2 + fw_{Suc}^3 + gw_{Suc}^4) \quad (\text{Eq. 3.5})$$

where $a-g$ are fitting parameters, w_{suc} is the weight fraction of sucrose, T is the temperature in Kelvin, and T^θ is a reference temperature. The values for T^θ and $a-g$ can be found in Table A.6.

When fitting Eq. 3.1 to the viscosity data for sucrose, the parameters C_1 , C_2 , k_{GT} and $T_{g,SOA}$ were included as fitting parameters, while the glass transition temperature of water was fixed at 135 K (Longinotti and Corti, 2008). The values for these parameters retrieved by fitting are reported in Table A.7. The $T_{g,SOA}$ value obtained by fitting was within the range measured experimentally (319-335K) (Dette et al., 2014; Roos, 1993; Simperler et al., 2006).

As mentioned in Section 3.2.1, Eq. 3.1 is based on the WLF equation. Since the WLF equation is only valid at or above the glass transition temperature, Eq. 3.1 was not used to predict viscosities above 10^{12} Pa s (which corresponds to mixing times longer than 5×10^5 h) (Fig. 3.10).

Similarly to α -pinene, if the temperature and RH in the PBL were such that the viscosity was greater than 10^{12} Pa s, the viscosity was assigned a value of 10^{12} Pa s and the mixing time was assigned a value of 5×10^5 hours. This assignment does not affect the conclusions in this manuscript since a mixing time of 5×10^5 hours is already well above the residence time of SOA particles in the atmosphere. However, this assignment did lead to a relatively large frequency count at 5×10^5 hours in Fig. 3.12.

3.2.3 Organic aerosol concentrations in the planetary boundary layer

The global chemical transport model GEOS-Chem was used to determine conditions in the PBL when SOA concentrations were significant (<http://acmg.seas.harvard.edu/geos/>). The version of GEOS-Chem used (v10-01) includes organic aerosol formation from semi-volatile and intermediate volatility organic compounds (SVOC and IVOC) (Pye and Seinfeld, 2010), plus new aerosol production from nitrate radical oxidation of isoprene and terpenes and NO_x -dependent aerosol yields from terpenes (Pye et al., 2010). In this version IVOC emissions are spatially distributed based on naphthalene. To estimate SVOC emissions the default GEOS-Chem primary organic aerosol emissions inventory was scaled by 1.27 following Pye and Seinfeld (2010). GEOS-Chem was run at a horizontal grid resolution of 4° latitude by 5° longitude using GEOS-5 meteorology with 47 vertical layers with a 3-year spin-up period. Shown in Fig. 3.2 are the monthly averaged total organic aerosol concentrations at the surface for the months of January and July 2006. These monthly averaged total organic aerosol concentrations were used to remove times and locations where SOA concentrations are not expected to be of major importance for climate, health or visibility.

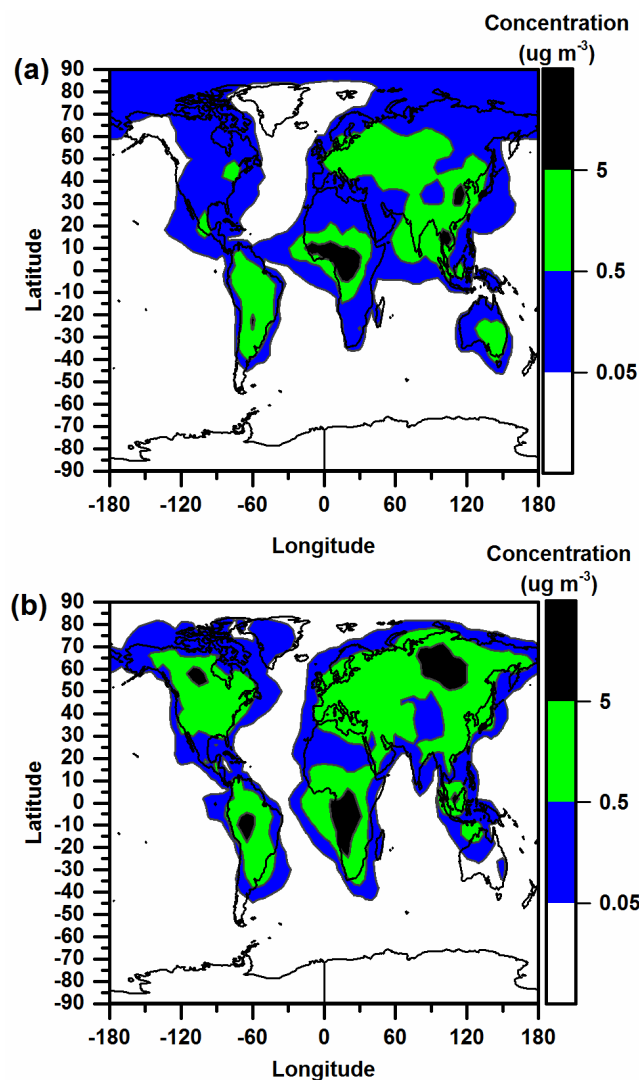


Figure 3.2: Monthly averaged total organic aerosol concentrations (color scale) at the Earth's surface in (a) January and (b) July, as calculated using GEOS-Chem.

3.2.4 RH and temperature in the PBL

Information on the RH and temperature distributions in the global PBL in different seasons were also needed to assess mixing times within SOA particles. First, the PBL heights were determined globally using the 6-h averaged GEOS-5 meteorology fields. Then, temperature and RH in each grid cell within the PBL were determined globally using the 6-h averaged GEOS-5 meteorology fields and the previously determined PBL heights. The GEOS-5 archive provides temperature and RH at a horizontal grid resolution of 4° latitude by 5° longitude and 47 vertical layers.

3.3 Results and Discussion

3.3.1 Parameterization of viscosity and mixing times within α -pinene SOA particles as a function of RH and temperature

Shown in Fig. 3.3a (contours) is the RH and temperature-dependent parameterization for α -pinene SOA viscosity based on viscosities measured at room temperature (Grayson et al., 2016) and low temperature (Järvinen et al., 2016), as well as the viscosity of water as a function of temperature (Crittenden et al., 2012). From the viscosity parameterization, the diffusion coefficients of organic molecules within α -pinene SOA particles were calculated using the Stokes-Einstein equation (Eq. 1.1). It is assumed that the SOA and water remain miscible and that the particle has a single phase. For the calculations, a value of 0.38 nm was used for the radius of the diffusing organic molecules within SOA, based on an assumed molecular weight of 175 g mol⁻¹ (Huff Hartz et al., 2005), a density of 1300 kg m⁻³ (Chen and Hopke, 2009; Saathoff et al., 2009) and spherical symmetry. The Stokes-Einstein equation assumes that the diffusing molecule experiences a homogenous and continuous fluid during diffusion. This can be achieved at low viscosities and when the radius of the diffusing molecule (R_{diff}) is larger than the radius of the matrix molecules (R_{matrix}). The Stokes-Einstein relation has been shown to break down and underpredict diffusion coefficients at high viscosities ($>10^6$ Pa s) (Bastelberger et al., 2017; Chenyakin et al., 2017; Power et al., 2013). Nevertheless, a recent study showed that diffusion coefficients predicted with the Stokes-Einstein equation in organic-water matrices were in reasonable agreement with measured diffusion coefficients in most cases when the radius of the diffusing molecule (R_{diff}) was greater than or equal to the radius of the matrix molecules (R_{matrix}) and when the viscosities were between 10⁻³ and 10⁶ Pa s (Evoy et al., 2020). Since the majority of the predicted viscosities in this chapter are less than or equal to 10⁶ Pa s (see below) the use of the Stokes-Einstein equation in this chapter is reasonable. Break-down of the Stokes-Einstein equation at viscosities greater than 10⁶ Pa s leads to larger diffusion coefficients and hence shorter mixing times.

From the diffusion coefficients, the characteristic mixing times of organic molecules within an α -pinene SOA particle were calculated using Eq. 1.2. For these calculations, it was assumed that the α -pinene SOA particles have a diameter of 200 nm, which is roughly the median diameter in the volume distribution of ambient SOA-containing particles (Martin et al., 2010; Pöschl et al., 2010; Riipinen et al., 2011). Once the mixing time has elapsed, the

concentration of the diffusing molecules at the centre of the particle is approximately 1/e of the equilibrium concentration (Seinfeld and Pandis, 2006; Zaveri et al., 2014). The calculated mixing times (Fig. 3.3b) illustrate that, as expected, inverse relationships exist between both mixing time and RH, as well as mixing time and temperature.

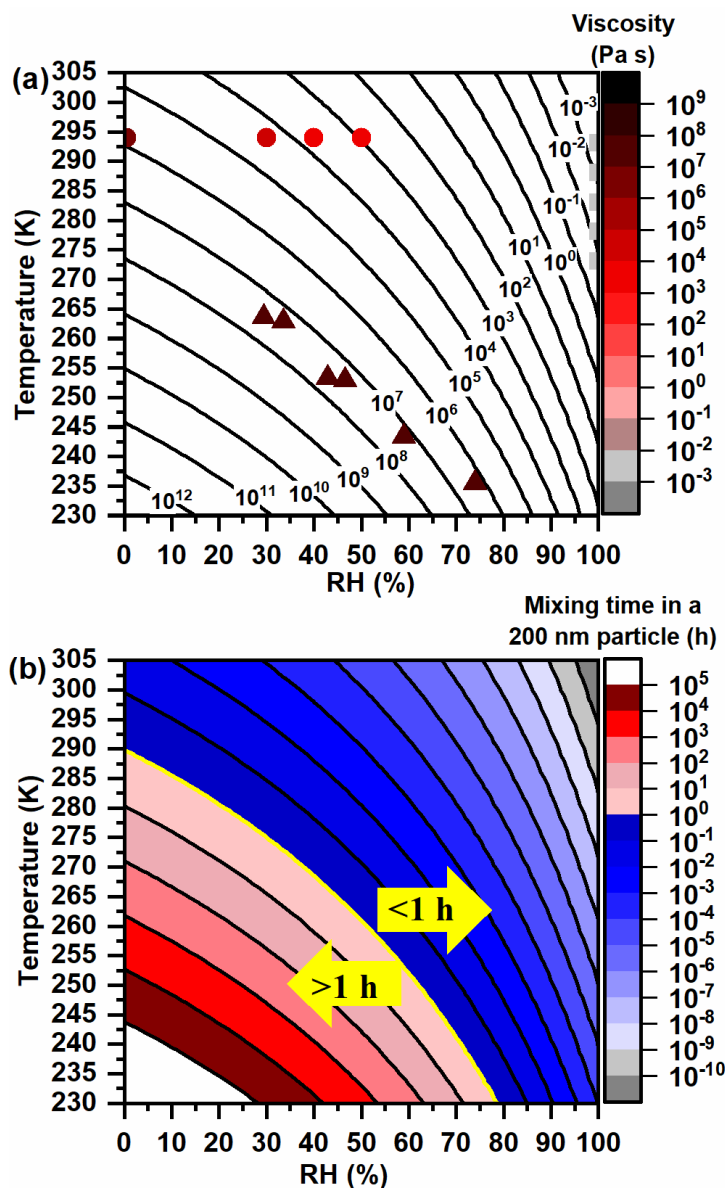


Figure 3.3: Plot of RH vs temperature with contour lines representing (a) the viscosity parameterization for α -pinene SOA particles and (b) mixing times calculated for organic molecules within 200 nm diameter α -pinene SOA particles. The symbols in (a) represent the laboratory data used to develop the parameterization: squares represent the water viscosities from Crittenden et al. (2012); triangles represent the viscosity data of α -pinene SOA from Järvinen et al. (2016) and the circles represent the viscosity data from Grayson et al. (2016). The viscosity parameterization is based on α -pinene SOA generated using mass concentrations of $\sim 1000 \mu\text{g m}^{-3}$.

3.3.2 RH and temperature in the PBL

Shown in Fig. 3.4a and 3.4b are the normalized frequency counts of temperature and RH in the PBL for the months of January and July, 2006, respectively, based on the archive of meteorological fields (GEOS-5) used in the global chemical transport model, GEOS-Chem, v10-01. Grid points were only included in the analysis if the grid points were within the PBL and the monthly average mass concentration of total organic aerosol was $> 0.5 \mu\text{g m}^{-3}$ at the surface, based on GEOS-Chem, v10-01 (Fig. 3.2). In other words, all the grid points were included in a column up to the top of the PBL when determining frequency counts if the monthly averaged total organic aerosol concentration was $> 0.5 \mu\text{g m}^{-3}$ at the surface. This filtering removes cases where SOA concentrations are not expected to be of major importance for climate, health or visibility. This mass concentration was chosen for the filtering because the mass concentration of total organic aerosol at the surface was $> 0.5 \mu\text{g m}^{-3}$ in all but one of the previous field measurements at remote locations (Spracklen et al., 2011).

The normalized frequency counts illustrate that the temperature and RH in the PBL are often in the range of 290-300 K and > 50 % RH for the month of January (Fig. 3.4a) and in the range of 285-300 K and > 30 % RH for the month of July (Fig. 3.4b). For reference, shown in Fig. A.2 and A.3 are the average temperature and RH conditions at the Earth's surface and top of the PBL, respectively, for January and July, based on the archive of meteorological fields for 2006 (GEOS-5).

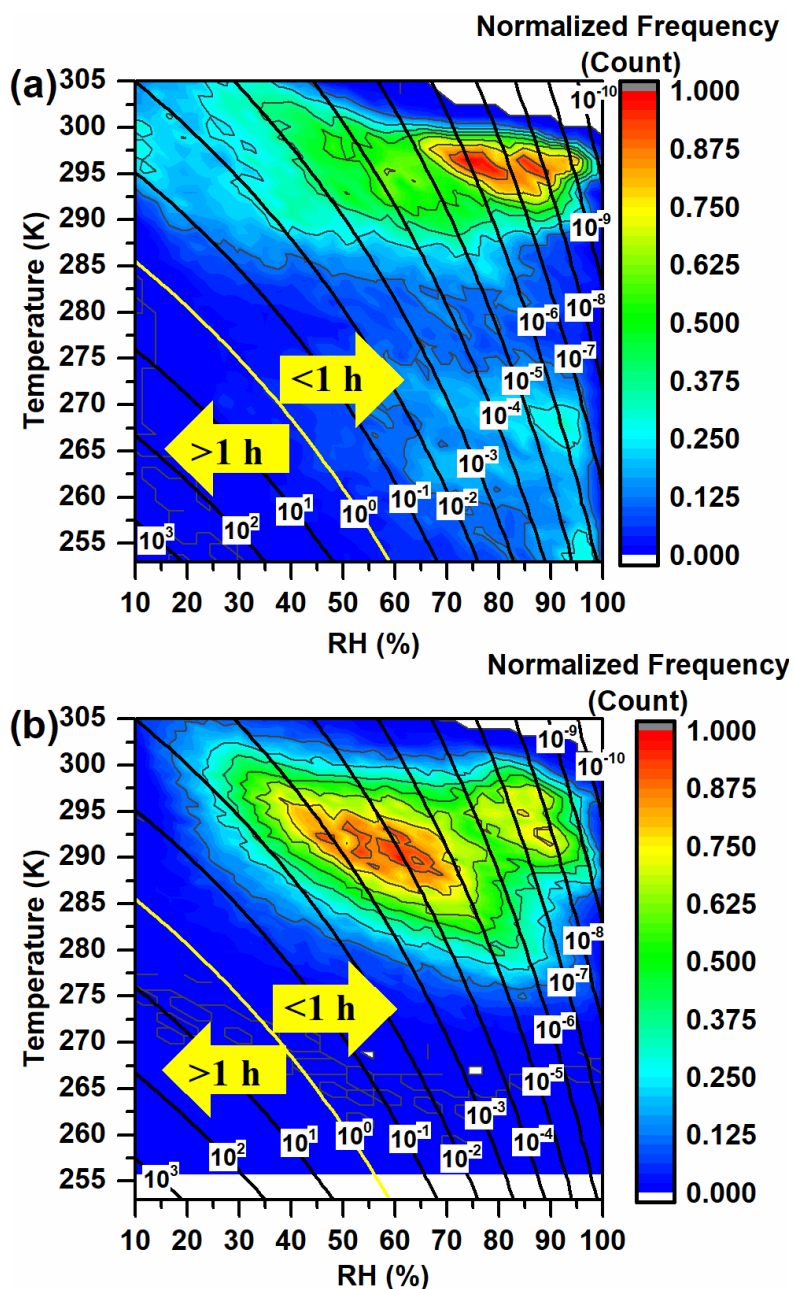


Figure 3.4: Six-hour normalized frequency counts of temperature and RH in the planetary boundary layer (PBL) (color scale) together with the mixing times for organic molecules within 200 nm α -pinene SOA particles (contours). Panel A shows the conditions for January and panel B shows the conditions for July. Mixing times (contours) are reported in hours. Frequency counts in the PBL were only included for the conditions where the mass concentration of total organic aerosol was $> 0.5 \mu\text{g m}^{-3}$ at the surface. The viscosity parameterization used to calculate mixing times was based on α -pinene SOA generated using mass concentrations of $\sim 1000 \mu\text{g m}^{-3}$.

3.3.3 Mixing times of organic molecules within α -pinene SOA particles in the PBL

Also shown in Fig. 3.4a and 3.4b are the mixing times within 200 nm α -pinene SOA particles predicted with the parameterization (contours). These results, together with the frequency counts of temperature and RH throughout the vertical column of the PBL, indicate that the mixing times of organic molecules within α -pinene SOA are often $< 1 \times 10^{-1}$ h for conditions in the PBL.

Shown in Fig. 3.5 are the normalized frequency distributions of mixing times within α -pinene SOA for January and July, based on the data in Fig. 3.4a and 3.4b. Figure 3.5 suggests that the mixing times within α -pinene SOA are < 1 h for 98.5 % and 99.9 % of the occurrences in the PBL during January and July, respectively, when monthly average total organic aerosol concentrations are $> 0.5 \mu\text{g m}^{-3}$ at the surface.

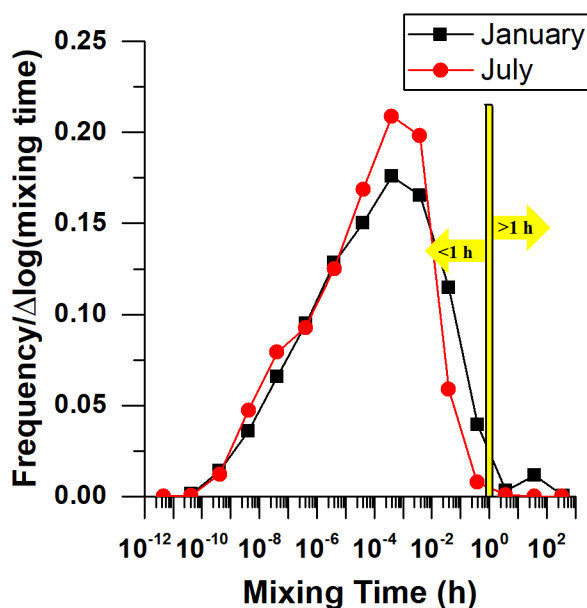


Figure 3.5: Normalized frequency distributions of mixing times within α -pinene SOA in the planetary boundary layer (PBL). Black symbols correspond to January and red symbols corresponds to July. Frequency counts in the PBL were only included for the conditions where the mass concentration of total organic aerosol was $> 0.5 \mu\text{g m}^{-3}$ at the surface. The viscosity parameterization used to calculate mixing times was based on α -pinene SOA generated using mass concentrations of $\sim 1000 \mu\text{g m}^{-3}$.

Within the PBL, RH increases and temperature decreases with altitude, with both changes being substantial and impacting mixing times in opposite directions. Shown in Fig. 3.6a-c are

calculated monthly average afternoon (13:00-15:00, local time) vertical profiles of temperature, RH, and mixing times within α -pinene SOA over Hyytiälä (boreal forest), and the Amazon (rainforest) for the driest month of the year at each location (the method used to calculate vertical profiles is described in the Section A.1). Afternoon vertical profiles were chosen since this is the time of the day when RH is typically lowest and thus mixing times are the longest. Figure 3.6c shows that mixing times within α -pinene SOA decrease significantly with altitude for these two locations. This is because the plasticizing effect of water on viscosity dominates the temperature effect for these conditions.

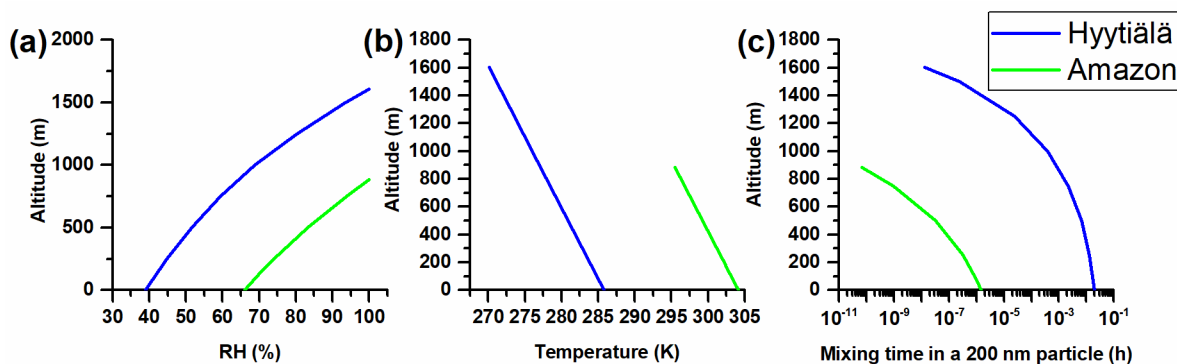


Figure 3.6: RH, temperature and estimated mixing times for α -pinene SOA as a function of altitude for Hyytiälä (boreal forest) and the Amazon (rainforest). The temperature and RH at ground level are the average afternoon values in the driest month of the year for the respective locations. The vertical profiles of temperature and RH are plotted until the RH is 100 % for these locations. The height at which RH reaches 100 % is only slightly lower than the average height of the planetary boundary layer predicted by GEOS-5 meteorology data. For details see Section A.1. The viscosity parameterization used to calculate mixing times was based on α -pinene SOA generated using mass concentrations of $\sim 1000 \mu\text{g m}^{-3}$.

Shown in Fig. 3.7 are global maps of the monthly averaged mixing times of organic molecules within α -pinene SOA for conditions at the top of the PBL for the months of January and July. Figure 3.7 shows that 92 % and 98 % of the locations for January and July, respectively, have a mixing time < 0.1 h for conditions at the top of the PBL when monthly averaged total organic aerosol surface concentrations are $> 0.5 \mu\text{g m}^{-3}$. Within the PBL, vertical mixing of air masses occurs on the order of 30 min. Since the mixing times within α -pinene SOA particles for conditions at the top of the PBL are < 0.1 h for most locations where the SOA concentrations are significant (total organic aerosol concentration $> 0.5 \mu\text{g m}^{-3}$ at the surface), a

reasonable upper limit to the mixing time within the α -pinene SOA studied here for most locations in the PBL is 30 min. During this 30 min interval, mixing times within α -pinene SOA particles can cycle between short and long values, though rarely being > 1 h (Fig. 3.4 and 3.5).

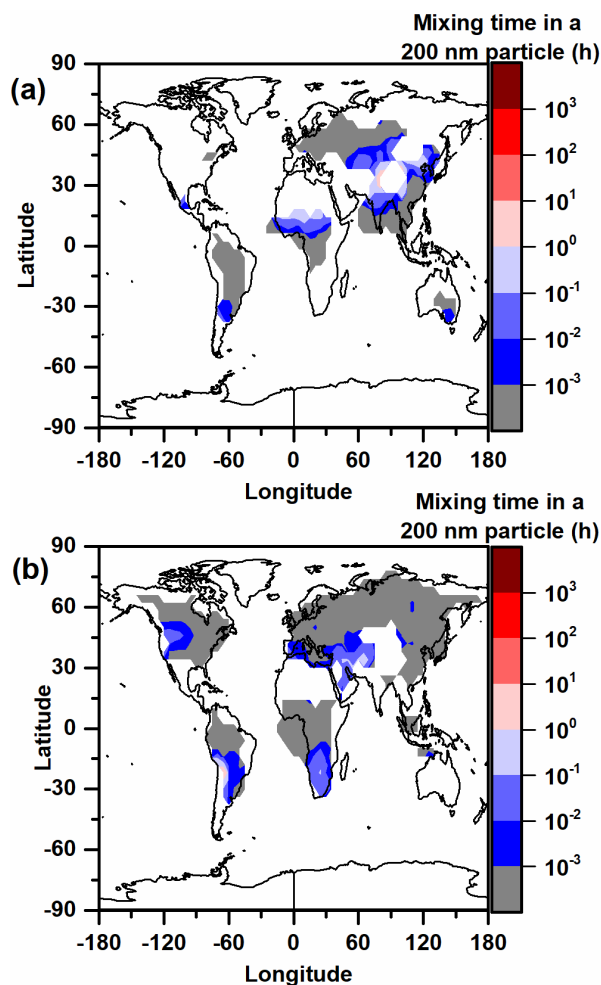


Figure 3.7: Mixing times of organic molecules within 200 nm α -pinene SOA particles at the top of the planetary boundary layer as a function of latitude and longitude in (a) January and (b) July. The color scale represents mixing times. Mixing times are only shown for locations with total organic aerosol concentrations $> 0.5 \mu\text{g m}^{-3}$ at the surface. The viscosity parameterization used to calculate mixing times were based α -pinene SOA generated using mass concentrations of $\sim 1000 \mu\text{g m}^{-3}$.

The percentages presented here are expected to be upper limits as the SOA was generated at high mass concentrations. Grayson et al. (2016) showed that under dry conditions the viscosity of α -pinene SOA may increase by a factor of 5 as the production mass concentration decreased from 1200 to $120 \mu\text{g m}^{-3}$. In addition, mass concentrations of biogenic SOA are typically $\leq 10 \mu\text{g m}^{-3}$.

m^{-3} in the atmosphere (Spracklen et al., 2011). As a result, mixing times in α -pinene SOA in the PBL may be higher than presented here, and these results should be considered a starting point for understanding the mixing times in the PBL.

3.3.4 Sensitivity analysis

To calculate the mixing times discussed above, the α -pinene SOA particles was assumed to have a diameter of 200 nm. These calculations were repeated assuming a diameter of 500 nm, since aged organic aerosol can have larger diameters (Takegawa et al., 2006). Based on the viscosity parameterization shown in Fig. 3.3a, mixing times within 500 nm α -pinene SOA particles are < 1 h for 95.9 % and 99.4 % of the occurrences in the PBL during January and July, respectively (Fig. 3.8).

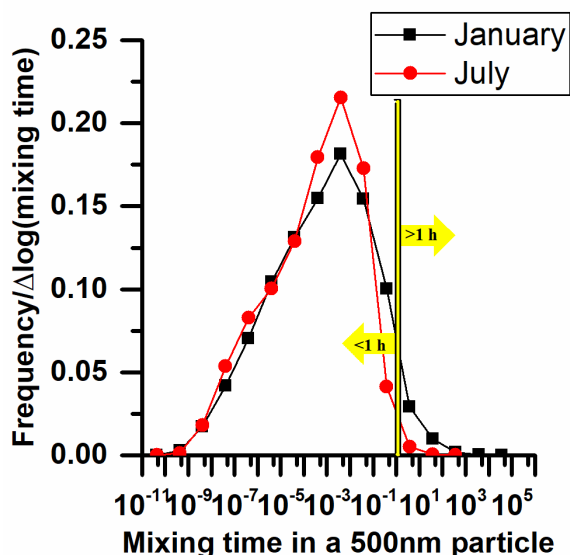


Figure 3.8: Normalized frequency distributions of mixing times within 500 nm α -pinene SOA in the planetary boundary layer (PBL). Black symbols correspond to January and red symbols corresponds to July. Frequency counts in the PBL were only included for the conditions where the mass concentration of total organic aerosol was $> 0.5 \mu\text{g m}^{-3}$ at the surface. The viscosity parameterization used to calculate mixing times was based on α -pinene SOA generated using mass concentrations of $\sim 1000 \mu\text{g m}^{-3}$.

The parameterization of viscosity used above was developed using viscosity measurements by Grayson et al. (2016), Järvinen et al. (2016), and Crittenden et al. (2012). As a sensitivity analysis, a second parameterization was developed, using the same procedure as describe above, but using the upper limits to the viscosities reported by Grayson et al. (2016) and

the upper limits to the RH ranges reported by Järvinen et al. (2016). This should result in an upper limit to the viscosity parameterization discussed above. The uncertainties in the measurements by Crittenden et al. (2012) were not considered since they are small compared to the uncertainties reported by Grayson et al. (2016) and Järvinen et al. (2016). Based on this second parameterization, mixing times are < 1 h for 96.6 % and 99.5 % of the occurrences in the PBL during January and July, respectively, when the total organic aerosol was $> 0.5 \mu\text{g m}^{-3}$ at the surface (Fig. 3.9).

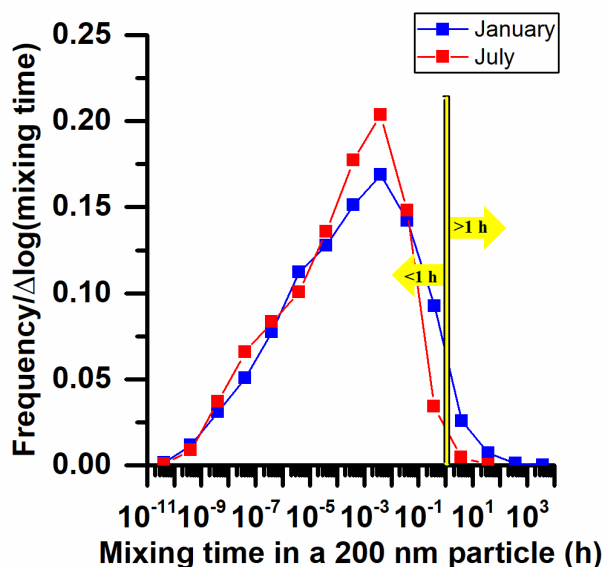


Figure 3.9: Normalized frequency distributions of mixing times within α -pinene SOA in the planetary boundary layer (PBL) for the parameterizations generated using the upper limit of the viscosity data from Grayson et al. (2016) and the upper RH limit from Järvinen et al. (2016). Blue symbols correspond to January and red symbols correspond to July. Frequency counts in the PBL were only included for the conditions where the mass concentration of total organic aerosol was $> 0.5 \mu\text{g m}^{-3}$ at the surface.

3.3.5 Mixing times of organic molecules within anthropogenic SOA particles in the PBL

Shown in Fig. 3.10a (contours) is the RH and temperature-dependent parameterization for sucrose particle viscosity based on room-temperature viscosity measurements (Först et al., 2002; Migliori et al., 2007; Perry and Green, 2008; Power and Reid, 2014; Quintas et al., 2006; Swindells and States., 1958; Telis et al., 2007), low temperature measurements (Zobrist et al., 2008), and the viscosity of water as a function of temperature (Crittenden et al., 2012). From the viscosity parameterization, the diffusion coefficients of organic molecules within the sucrose

particles were calculated using the Stokes-Einstein equation (Eq. 1.1). The hydrodynamic radius was assumed to be 0.38 nm, the same as for the α -pinene SOA.

From the diffusion coefficients, the characteristic mixing times of organic molecules within sucrose particles were calculated using Eq. 1.2 assuming a particle diameter of 200 nm (Fig. 3.10b).

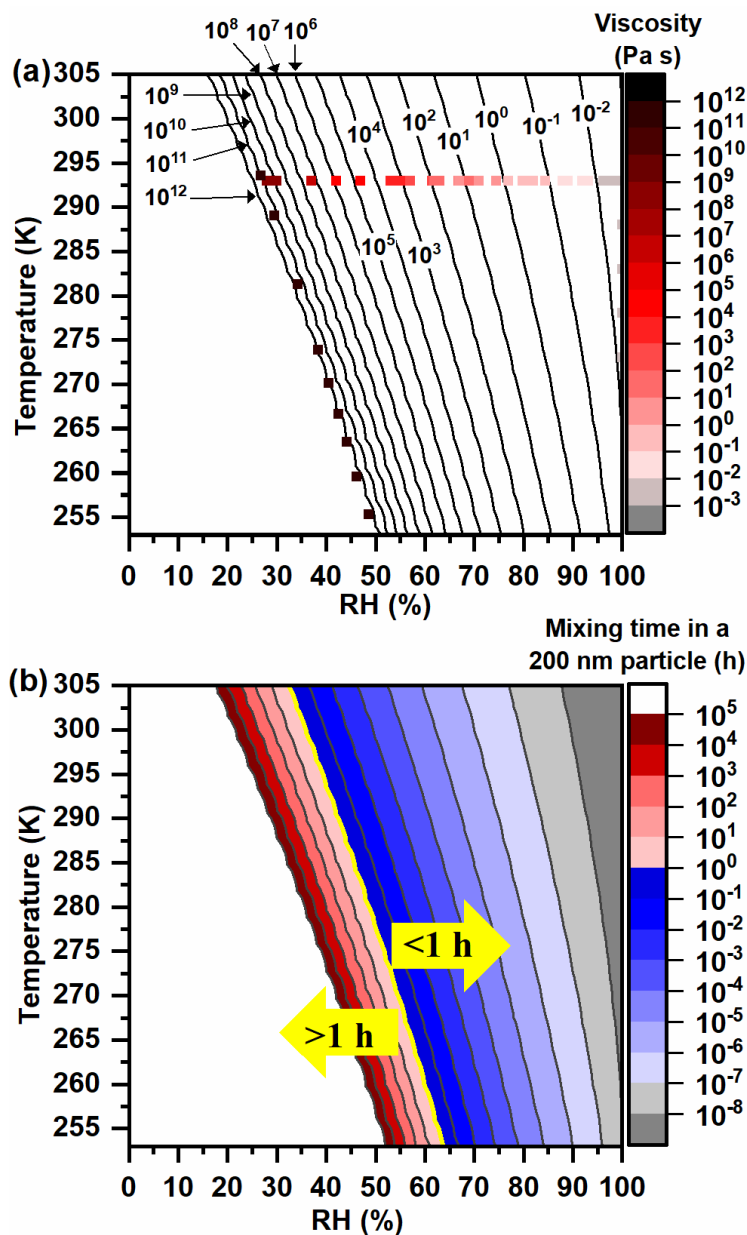


Figure 3.10: Plot of RH vs temperature with contour lines representing (a) the viscosity parameterization for sucrose particles and (b) mixing times calculated for organic molecules within 200 nm diameter sucrose particles. The symbols in (a) represent the laboratory data used to develop the parameterization (Table A.5). Mixing times were calculated from the viscosity parameterization (Panel A) and Eq. 1.1 and 1.2.

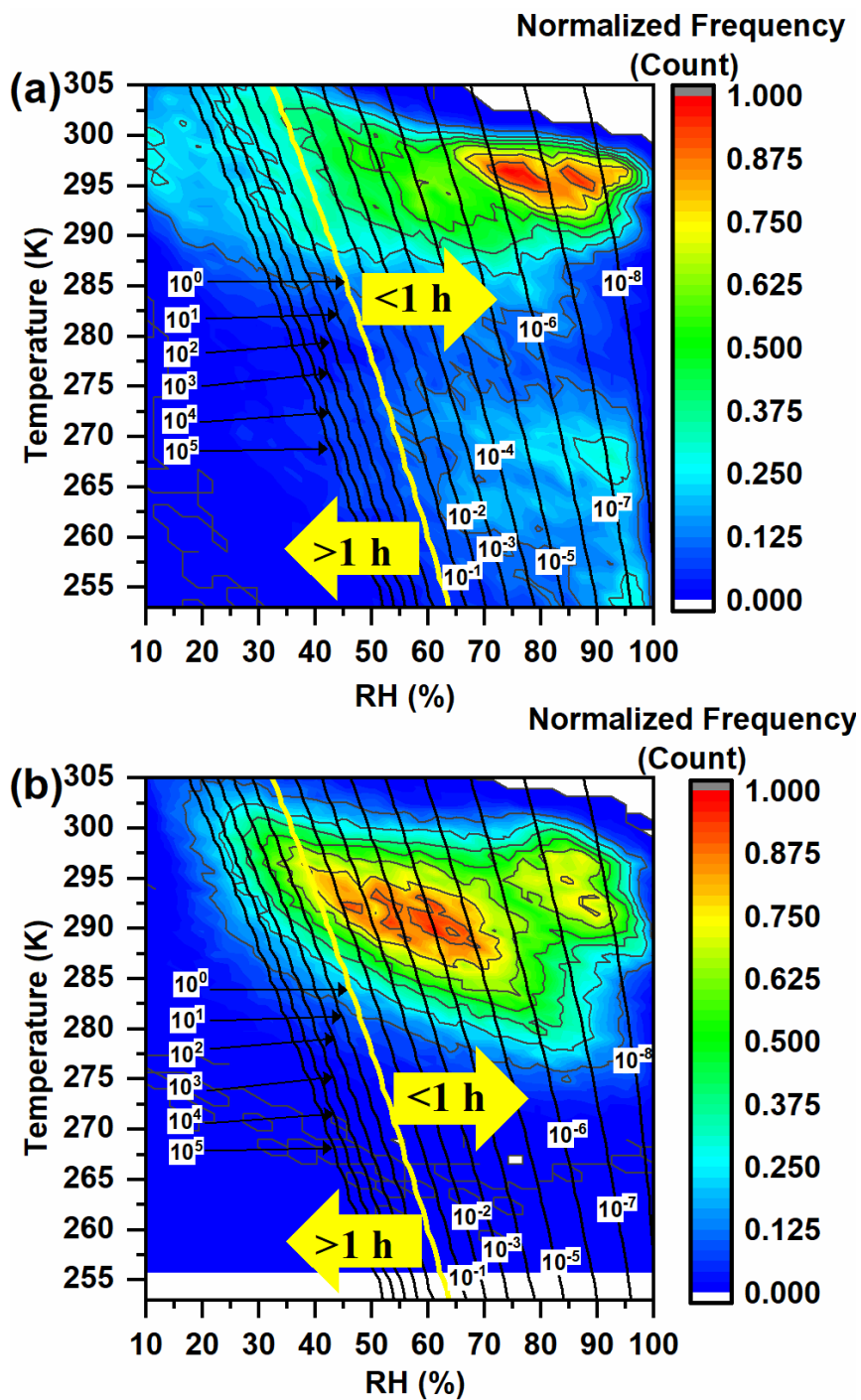


Figure 3.11: Six-hour normalized frequency counts of temperature and RH in the planetary boundary layer (PBL) (color scale) together with the mixing times for organic molecules within 200 nm sucrose particles (as surrogates of anthropogenic SOA) (contours). Panels A and B show the conditions for January and July, respectively. Mixing times (contours) are reported in hours. Frequency counts in the PBL were only included for the conditions when the mass concentration of total organic aerosol was $> 0.5 \mu\text{g m}^{-3}$ at the surface.

Shown in Fig. 3.11 are the normalized frequency counts of temperature and RH in the PBL for the months of January and July, 2006, respectively (See Section 3.3.2 for more information). Also included are the mixing times of organic molecules within 200 nm sucrose particles predicted by the parameterization (contours). Combine with the frequency counts of the temperature and RH throughout the vertical column of the PBL, these results indicate that the mixing times of organic molecules within sucrose particles are frequently < 1 h, however some conditions do lead to mixing times > 1 h.

Shown in Fig. 3.12 are the normalized frequency distributions of the mixing times within sucrose particles for January and July, based on the data from Fig.3.11a and 3.11b. Assuming sucrose is a good proxy for anthropogenic SOA, Fig. 3.12 suggests that 70 % and 83 % of the mixing times within anthropogenic SOA in the PBL are < 1 h for January and July, respectively, when SOA concentrations are significant (total organic aerosol concentration $> 0.5 \mu\text{g m}^{-3}$ at the surface).

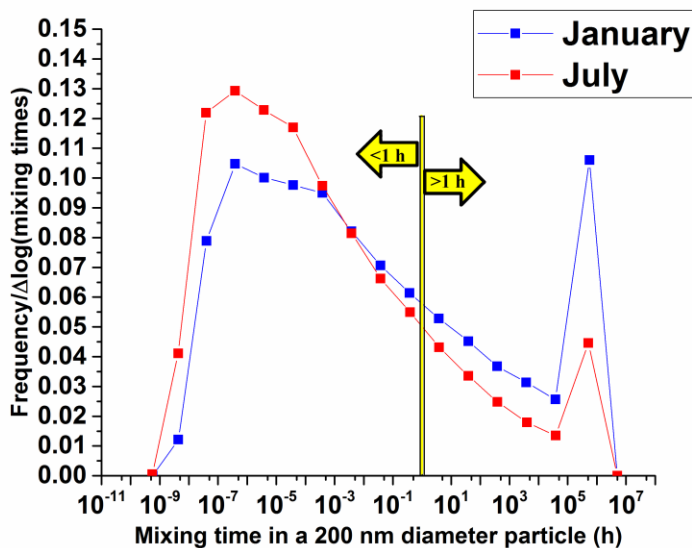


Figure 3.12: Normalized frequency distributions of mixing times within sucrose particles (as surrogates for anthropogenic SOA) in the planetary boundary layer (PBL). Red symbols correspond to January and blue symbols correspond to July. Frequency counts in the PBL were only included for the conditions where the mass concentration of total organic aerosol was $> 0.5 \mu\text{g m}^{-3}$ at the surface. The relatively large frequency count at 5×10^5 h is because all cases that had a viscosity greater than 10^{12} Pa s were assigned a value of 10^{12} Pa s.

Shown in Fig. 3.13 are global maps of the monthly averaged mixing times of organic molecules within sucrose particles for conditions at the top of the PBL for the months of January and July. Figure 3.13 shows that 81 % and 87 % of the locations for January and July, respectively, have a mixing time < 0.1 h at the top of the PBL when surface concentrations of total organic aerosol are $> 0.5 \mu\text{g m}^{-3}$.

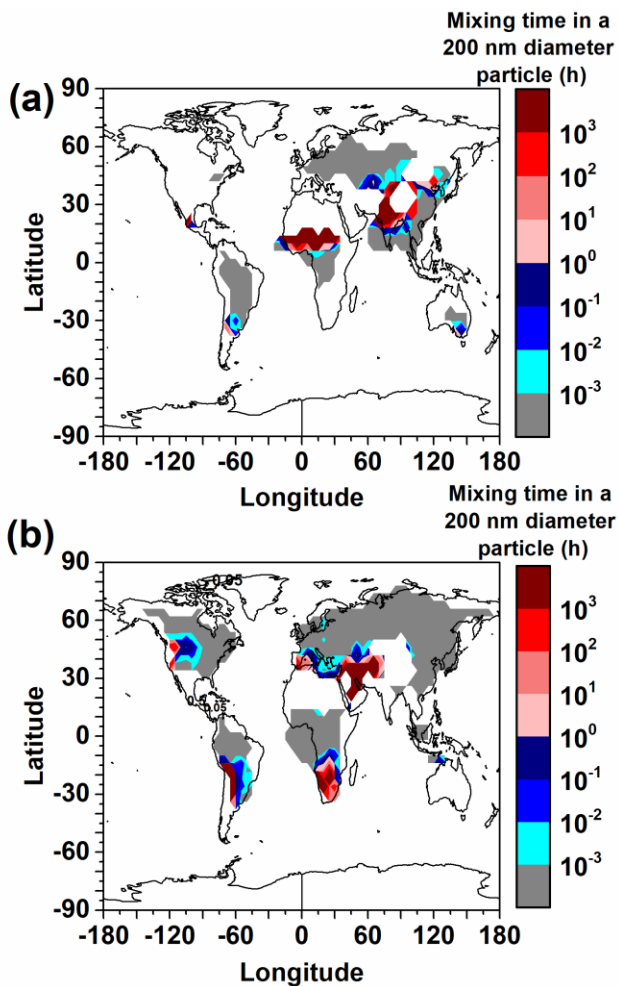


Figure 3.13: Mixing times of organic molecules within 200 nm sucrose particles (as surrogates of anthropogenic SOA) at the top of the planetary boundary layer as a function of latitude and longitude. The color scale represents mixing times. Mixing times are only shown for locations with total organic aerosol concentrations $> 0.5 \mu\text{g m}^{-3}$ at the surface. Panels A and B correspond to January and July, respectively.

3.3.6 Comparison with previous studies

Shiraiwa et al. (2017b) recently estimated mixing times of organic molecules within SOA in the troposphere using a global chemistry climate model and a relationship between glass

transition temperatures, molar mass, and oxygen-to-carbon elemental ratios. Their results suggest mixing times of organic molecules within SOA are short (< 1 min) over the oceans, tropics, and high latitudes at the surface and 850 hPa. On the other hand, their results suggest mixing times are long (> 1 h) over dry regions (i.e. major deserts) at the surface and at 850 hPa and over most continental regions at 850 hPa. The general trends observed by Shiraiwa et al. (2017b) are consistent with the trends observed here. However, the mixing times predicted by Shiraiwa et al. (2017b) appear to be longer than the mixing times predicted here using viscosities of α -pinene SOA generated with a mass concentration $\sim 1000 \mu\text{g m}^{-3}$. Quantitative differences between the current work and the work by Shiraiwa et al. (2017b) are not surprising since Shiraiwa et al. (2017b) considered both anthropogenic SOA and biogenic SOA simultaneously, and since they used a very different approach to estimate viscosities of atmospheric SOA.

3.4 Summary and conclusions

A parameterization for viscosity as a function of temperature and RH was developed for α -pinene SOA based on room-temperature and low-temperature viscosity data of α -pinene SOA generated in the laboratory using mass concentrations of $\sim 1000 \mu\text{g m}^{-3}$. A mass concentration of $\sim 1000 \mu\text{g m}^{-3}$ was focused on because low-temperature and room-temperature viscosity measurements have been carried out using this mass concentration. Based on this parameterization, as well as RH and temperatures in the PBL, the mixing times within α -pinene SOA are < 1 h for 98.5 % and 99.9 % of the occurrences in the PBL during January and July, respectively, when monthly average total organic aerosol concentrations are $> 0.5 \mu\text{g m}^{-3}$ at the surface. Also based on this parameterization, 92 % and 98 % of the locations for January and July, respectively, have a mixing time < 0.1 h for conditions at the top of the PBL when monthly averaged total organic aerosol surface concentrations are $> 0.5 \mu\text{g m}^{-3}$. The impact of mass concentration of the SOA on the mixing times of organic molecules within SOA needs further study.

As a starting point to quantify how often mixing times of organic molecules are < 1 h within anthropogenic SOA, a parameterization for viscosity as a function of temperature and RH was developed using sucrose-water viscosity data. Based on this parameterization and assuming sucrose is a good proxy for anthropogenic SOA, 70 % and 83 % of the mixing times within

anthropogenic SOA in the PBL are < 1 h for January and July, respectively, when SOA concentrations are significant (total organic aerosol concentration > 0.5 $\mu\text{g m}^{-3}$ at the surface).

Chapter 4: Humidity-dependent viscosity of SOA from ozonolysis of β -caryophyllene: Measurements, predictions, and implications

4.1 Introduction

As outlined in Chapter 1, SOA is formed from the oxidation of volatile organic compounds from biogenic or anthropogenic sources. Many studies for the viscosity and mixing times of organic molecules in biogenic SOA focus on SOA derived from isoprene and monoterpenes. However, a recent modelling study showed that the global burden of SOA increased by 48% relative to the base case when sesquiterpenes were included in the model (Khan et al., 2017). Field measurements and modelling studies have also illustrated that sesquiterpenes can contribute significantly to atmospheric SOA (Bouvier-Brown et al., 2009; Sakulyanontvittaya et al., 2008; Yee et al., 2018; Ying et al., 2015). Examples of atmospherically relevant sesquiterpenes include β -caryophyllene, α -cedrene, α -humulene, and longifolene (Guenther et al., 2012; Helmig et al., 2007).

Only two studies have reported diffusion rates or viscosities within sesquiterpene SOA. Zhao et al. (2016) measured a diffusion coefficient of $3 \times 10^{-19} \text{ m}^2 \text{ s}^{-1}$ under dry conditions of 2-ethylhexyl nitrate within SOA generated from α -cedrene ozonolysis. Champion et al. (2019) measured viscosities under dry conditions of SOA generated from β -caryophyllene photooxidation. Measurements of diffusion rates or viscosities within sesquiterpene SOA as a function of RH are still required. Such RH-dependent measurements are critical since RH varies from 0 to over 100% in the atmosphere and viscosity and diffusion rates have a strong dependence on RH (Koop et al., 2011).

Several studies have detailed semi-empirical methods for predicting viscosities of SOA from its chemical composition (DeRieux et al., 2018; Gervasi et al., 2020; Li et al., 2020; Shiraiwa et al., 2017b), which can be used with chemical transport models to predict the viscosity of atmospheric SOA (Schmedding et al., 2020; Shiraiwa et al., 2017b). These methods have been used to predict the viscosity and glass transition temperatures of several types of SOA (isoprene SOA, α -pinene SOA, toluene SOA, diesel fuel SOA and ambient SOA) (DeRieux et al., 2018; Ditto et al., 2019; Gervasi et al., 2020; Pratap et al., 2018; Riva et al., 2019; Schum et al., 2018; Slade et al., 2019; Song et al., 2019; Wolf et al., 2019; Zhang et al., 2019b, 2019a). However, their predictive accuracy has only been tested in a few cases and has never been tested for sesquiterpene SOA.

The viscosity of SOA as a function of RH can also be predicted using mixing rules and measured viscosities of water and dry SOA (Centeno et al., 2011; Gervasi et al., 2020; Rovelli et al., 2019; Song et al., 2016b). Recently, Gervasi et al. (2020) showed that a mole-fraction based mixing rule is the best choice among simple mixing rules for predicting viscosity in a binary aqueous system. However, the accuracy of mixing rules for predicting the viscosity of SOA as a function of RH has only been tested in a few cases (Gervasi et al., 2020; Rovelli et al., 2019; Song et al., 2016b).

To address the knowledge gaps mentioned above, the viscosity as a function of RH was measured for SOA generated via ozonolysis of β -caryophyllene (see Fig. 4.1 for the chemical structure of β -caryophyllene). β -caryophyllene is a biogenic volatile organic compound emitted from vegetation such as Scots pine trees, maize, and grasses (Faiola et al., 2019; Muchlinski et al., 2019). The measured viscosities were converted to characteristic mixing times of organic molecules within β -caryophyllene SOA for typical RH conditions found in the PBL with temperatures above ~ 290 K. In addition to measuring viscosity, the chemical composition of the SOA was measured using high resolution mass spectrometry with three different types of direct-infusion ionization sources. The chemical composition and the measured RH-dependent viscosities for β -caryophyllene SOA were used to test the accuracy of the parameterization from DeRieux et al. (2018) for predicting viscosities of β -caryophyllene SOA. Finally, the ability of a simple mole-fraction based Arrhenius mixing rule to predict the viscosity of the β -caryophyllene SOA as a function of RH from knowledge of the viscosity of water and the dry SOA was evaluated.

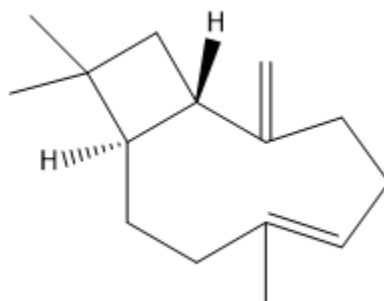


Figure 4.1: Chemical structure of β -caryophyllene.

4.2 Experimental

4.2.1 SOA generation

SOA was generated in an environmental chamber at the University of British Columbia via dark ozonolysis of β -caryophyllene. The chamber was based on the design by Parsons et al. (2011) and consisted of a 1.8 m³ Teflon bag (Ingeniven) housed in a reflective aluminum enclosure (Fig. B.1). The enclosure had 24 UV lights (40 W Sylvania black lights, peak UV wavelength of \sim 360 nm) mounted on the inside of the enclosure for photochemical studies; however, the lamps were not used in the current study except for cleaning the Teflon bag. The chamber bag was periodically cleaned by passing dry air, ozone (1.2 ppm), and water vapor through the chamber with the UV lights on. Particles were continuously generated and collected by running the environmental chamber in a continuous-flow mode, similar to other continuous-flow environmental chambers (King et al., 2007, 2009; Kleindienst et al., 1999; Shilling et al., 2008). The flow rates into and out of the chamber were \sim 18.2 L min⁻¹, resulting in a calculated residence time of 1.7 h, consistent with residence time measurements (Fig. B.2).

A zero-air generator (Aadco 737) provided dry and hydrocarbon free air for SOA generation. The RH of the air from the generator was $<$ 1% based on measurements with a humidity meter (Vaisala HMT 330). Ozone was generated externally to the chamber by flowing 0.5-1 L min⁻¹ of the dry air through an ozone generator (Jelight 600). A mixture of 2 wt % β -caryophyllene (Sigma-Aldrich, \geq 98%) was prepared in 2-butanol (Sigma-Aldrich, \geq 99% purity) and the resulting solution was continuously added (flow rate of 25 μ l h⁻¹) with a syringe pump (Cole-Parmer Model 100) to a round bottom flask heated to 70 °C. A flow of 17.2-17.7 L min⁻¹ of the dry air was passed through the heated flask and carried the β -caryophyllene and 2-butanol vapours into the chamber. The 2-butanol was added to the chamber as a scavenger of OH radicals, which can be produced during some reaction pathways for the ozonolysis of β -caryophyllene (Kroll et al., 2002). The 2-butanol was estimated to scavenge \sim 83% of OH radicals produced in the chamber based on the reaction rates of OH with 2-butanol and β -caryophyllene (see Section B.1).

Ozone and β -caryophyllene entered the chamber through two separate 0.63 cm diameter tubes (outer diameter) that had exits \sim 0.2 cm apart within the chamber to facilitate mixing. Prior to reaction, ozone and β -caryophyllene concentrations in the chamber were 400-1200 ppb and 40 ppb, respectively. After SOA formation, aerosols exited the chamber through a 0.63 cm tube \sim 1

m away from the chamber inlets. Part of the exit flow was sampled with an ozone detector (49i, Thermo Scientific, USA). The remaining flow passed through an ozone denuder (Ozone Solutions, ODS-1) and was sampled with either an impactor to collect material for the viscosity and mass spectrometry measurements or with a scanning mobility particle sizer (SMPS) (TSI 3080 DMA and 3782 CPC) and an optical particle sizer (GRIMM OPC, Model 11-S) to measure the number-diameter distribution of the SOA. From the number-diameter and an assumed SOA density of 990 kg m^{-3} (Tasoglou and Pandis, 2015), the mass concentration of the SOA in the chamber was $50\text{--}60 \text{ }\mu\text{g m}^{-3}$.

To collect SOA for viscosity or mass spectrometry measurements, the flow was sampled with a multi-orifice single-stage impactor (MSP Corporation) operated at a constant flow rate of 15 L min^{-1} and a cut-size below $0.18 \text{ }\mu\text{m}$ (aerodynamic particle diameter). The impactor functions by directing the SOA in the gas stream directly at an impaction plate with a sample substrate on top of it. The gas flow direction changes sharply at the impaction plate. Sufficiently large SOA particles have enough momentum that they aren't able to adjust to the change in flow direction rapidly enough and instead hit the sample substrate, depositing the SOA on the surface. The diameter of the SOA particles collected on the impactor is determined by factors such as the gas flow rate and the distance between the inlet nozzles and the impaction plate. The sample collection time ranged from 16-24 h, resulting in 0.7 mg to 1 mg of SOA collected per sample, assuming 100% collection efficiency. For the viscosity measurements, SOA was collected on fluorinated glass coverslips coated with Trichloro (1H,1H,2H,2H-perfluorooctyl) silane or FluoroPel 800 (Cytonix USA). For mass spectrometry measurements, SOA was collected on PTFE filters (47 mm, Whatman).

4.2.2 Measurements of particle viscosity

The viscosity of the β -caryophyllene SOA was measured using the poke-flow technique with fluid simulations as described in Sections 2.2.1 and 2.2.2. The fluorinated glass coverslips used in the impactor were mounted in the flow cell. Examples of the recovery of poked particles are shown in Fig. 4.2. The values of the surface tension, slip length, density and contact angle used in the simulations are in Table B.1.

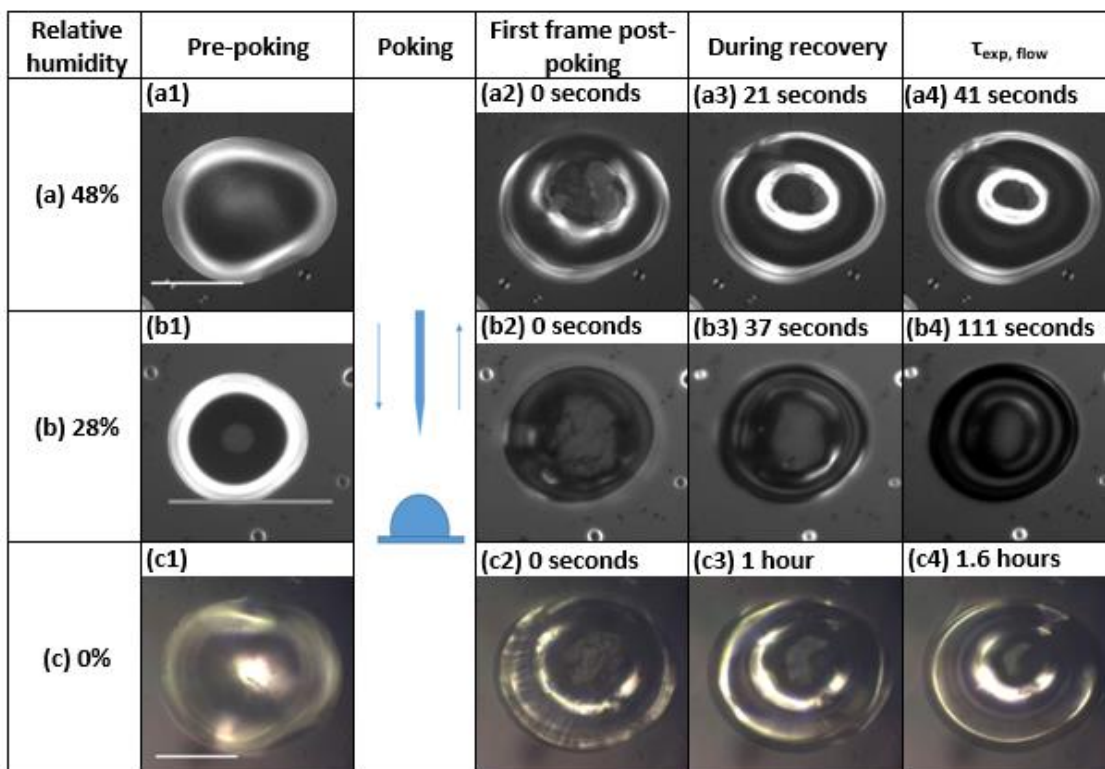


Figure 4.2: Optical images of particles taken during poke-flow experiments at RH values of a) 48%, b) 28%, and c) 0%. Images a1, b1, and c1 correspond to images taken before the particle was poked. Images a2, b2, and c2 are images taken immediately after poking. Images a3, b3, and c3 are taken during recovery and images a4, b4, and c4 are taken at $\tau_{\text{exp, flow}}$ where the equivalent area diameter of the hole has decreased to 50% of its original size. The white scale bar in the pre-poking images corresponds to 50 μm . The circle in the centre of the particle in b1 is an optical effect due to the hemispherical shape.

Prior to poking the SOA, the particles were conditioned to the surrounding RH for 3-5, 5-25, 20, and 2-22 h for RH-values of 48, 28, 15 and 0 %, respectively (Table B.2). These conditioning times were a factor of 0.08 to 10 greater than the estimated mixing times of water within the SOA (Section B.2 and Table B.2). Viscosities were not dependent on the conditioning times used (Fig. 4.3). Based on this information, it was assumed that the SOA was near equilibrium with the gas-phase water vapour prior to poking the particles for the viscosity measurements.

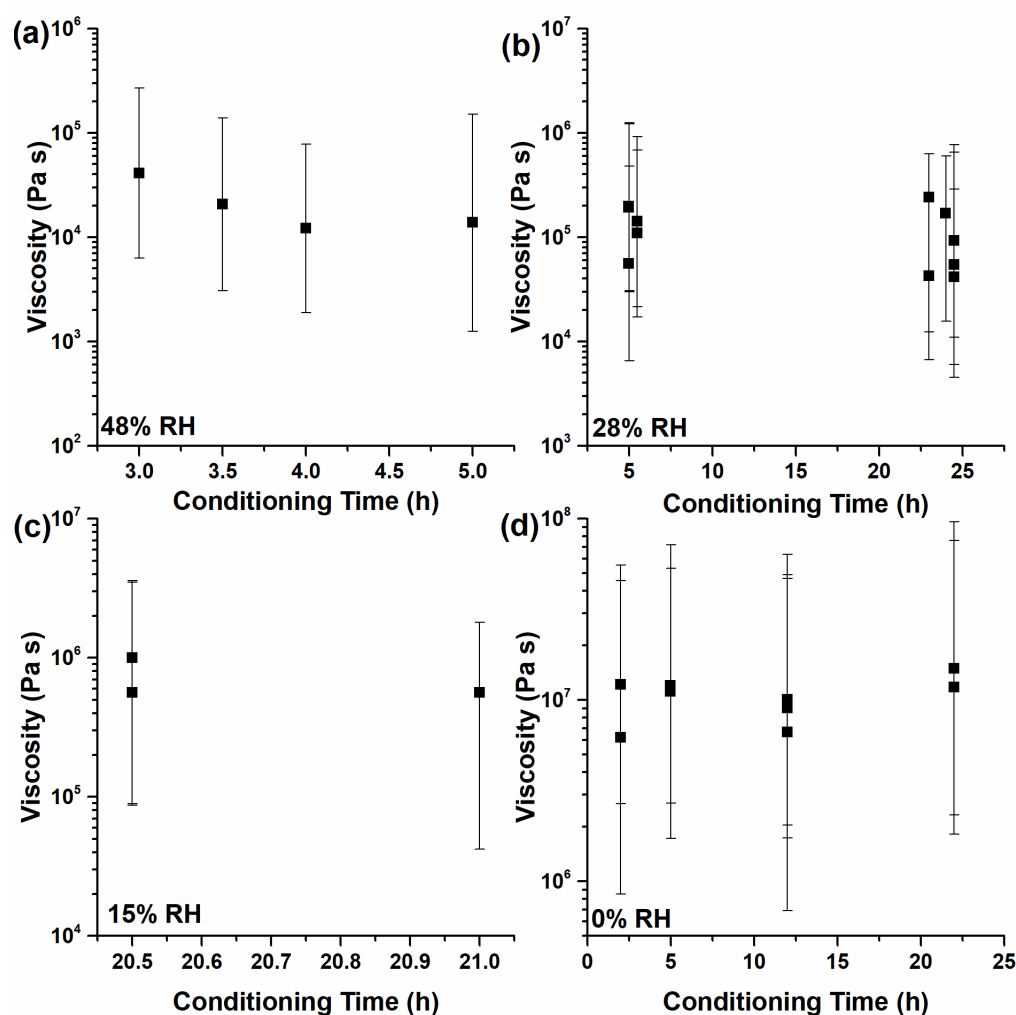


Figure 4.3: Viscosities as a function of particle conditioning time to the surrounding RH. Measurements were taken at RHs values of 48% in panel A, 28% in panel B, 15% in panel C, and 0% in panel D.

When the particles were conditioning to the surrounding RH, semi-volatile organic material could evaporate, potentially leading to a change in the viscosity of the particles (Buchholz et al., 2019; Wilson et al., 2015; Yli-Juuti et al., 2017). To determine if evaporation of semi-volatile organic material was important in the poke-flow experiments, a newly collected SOA sample was added to the flow cell and exposed to a dry flow of N_2 gas (0.25 L min^{-1}) for 24 h, and images were recorded every hour to quantify evaporation of the SOA particles. In this experiment, the maximum change in the 2-D projected area of the SOA particles was $-1.4 \pm 0.4 \%$. (Fig. 4.4). It was concluded that the composition change due to evaporation during the poke-

flow experiments was minimal. This is consistent with expectations since the volume of N₂ gas exposed to the particles in the poke-flow experiments ($\approx 1.2 \times 10^3$ L) was small compared to the volume of air sampled from the environmental chamber when collecting SOA for the poke-flow experiments (1.6×10^4 - 2.4×10^4 L).

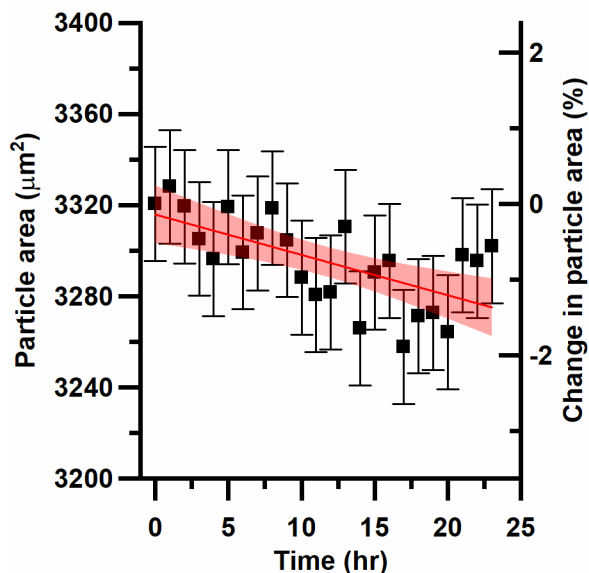


Figure 4.4: Particle 2-D projected area as a function of time during exposure to dry nitrogen flow with a secondary y-axis showing the percent change in projected particle area. The y-error bars correspond to the uncertainty in the measurement of the particle area in μm^2 . The straight line is a linear fit to the data and the shaded regions are the 95% confidence intervals for that fit.

4.2.3 Measurements of the chemical composition of SOA using mass spectrometry

High resolution mass spectrometry data of the collected samples were obtained in positive and negative ion mode separately using nano-desorption electrospray ionization (nano-DESI) (Roach et al., 2010), nano-electrospray ionization (nano-ESI), and electrospray ionization (ESI) sources attached to a Q-Exactive HF-X Orbitrap mass spectrometer (Thermo Scientific) with a mass resolving power of 2.4×10^5 at m/z 200. Data were acquired from 80 to 1200 m/z in the full scan mode. A low mass calibration was performed prior to analysis using commercial mass calibration solutions (Thermo scientific, PI-88323 and PI-88324) in both positive (+) and negative (-) ion mode, separately. A spray voltage of (+ or -) 3.5 kV, funnel RF level of 80 and a capillary temperature of 250 °C were used in all ionization modes. Samples were delivered using a syringe pump at $1 \mu\text{L min}^{-1}$ (nano-DESI), $2 \mu\text{L min}^{-1}$ (nano-ESI), and $5 \mu\text{L min}^{-1}$ (ESI).

Nitrogen gas (99.995% purity) flow rates used in the ESI source include a sheath gas of 10-12 units and an auxiliary gas of 0-1 units. For nano-DESI, half of the PTFE filter ($1/2 \times 47$ mm, Whatman) of each sample was taped to a glass slide. A stable solvent droplet (1:1; acetonitrile: water) was formed at a juncture between the solvent capillary and spraying capillary. The substrate containing the SOA sample was brought in contact with the droplet using micromanipulators, and the droplet was dragged over the sample while acquiring mass spectra for approximately 2-3 minutes. In addition to the samples, a solvent blank consisting of a clean substrate was analyzed following the same procedure in both positive and negative mode. For nano-ESI and regular ESI, the remaining filter halves were solvent extracted with 2 mL of a 1:1 mixture of acetonitrile and water under sonication for 15 min. The extracted solution was then passed through a $0.45 \mu\text{m}$, PTFE membrane syringe filter (Fisherbrand) to remove any undissolved material. An additional 1 mL of solvent was passed through the PTFE membrane filter and collected with the filtered extracts to limit the loss of extracts on the filter surface. Data were acquired for approximately 2 min for nano-ESI and ESI. A solvent blank (a clean filter treated the same way as described above) was also analysed for nano-ESI and ESI in positive and negative mode.

The analysis procedure of the mass spectrometry data was performed as described in Nizkorodov et al. (2011). The Decon2LS software program (<https://omics.pnl.gov/software/decontools-decon2ls>) was used to extract centre positions for all peaks in the mass spectra. Only peaks below m/z 700 were considered in analysis because peaks at larger m/z values had negligibly small abundances. Peaks that were present in the solvent blank with abundance in excess of 10% of sample peak abundance were considered impurities and excluded from further analysis. All positive ions were assigned to formulas $\text{C}_{1-40}\text{H}_{2-80}\text{O}_{0-35}\text{N}_{0-3}\text{Na}_{0-1}^+$ with a m/z accuracy of 0.001. Protonation was the most common ionization mechanism in the positive ion mode although a small fraction of the ions were monosodium adducts. All negative ions were assigned to formulas $\text{C}_{1-40}\text{H}_{2-80}\text{O}_{0-35}\text{N}_{0-3}^-$ assuming deprotonation was the only ionization mechanism. Only closed-shell ions were permitted, and the elemental ratios were constrained to be $0.30 < \text{H}/\text{C} < 2.25$ and $0.00 < \text{O}/\text{C} < 2.30$ to ensure elemental formula assignments were physically reasonable. Peaks that could not be assigned with the above constraints were assigned manually using the MIDAS molecular calculator (<http://magnet.fsu.edu/~midas/>). The ^{13}C isotope and other obvious impurities, signified by

unreasonably high mass defects, were examined and removed from the final data set. The N-containing species made up a small portion (<1%) of the total signal and were therefore treated as impurities and excluded. The assignments are reported in neutral mass of each species. The datasets for the positive and negative modes were aligned based on neutral mass and each mode was normalized, so the sum of the intensities over all masses in a single mode would add up to one and then the intensities were averaged between the modes for each mass for the combined dataset. The combined dataset was then used to predict the viscosity.

4.2.4 Predictions of the viscosity of SOA from measurements of the chemical composition of the SOA

To predict viscosity of the SOA from the mass spectra, the approach of DeRieux et al. (2018) was used. First, the glass transition temperature (T_g) of compound i was predicted from the mass spectra using the following equation (DeRieux et al., 2018):

$$T_{g,i} = (n_C^0 - \ln(n_C))b_C + \ln(n_H) b_H + \ln(n_C) \ln(n_H) b_{CH} + \ln(n_O) b_O + \ln(n_C) \ln(n_O) b_{CO} \quad (\text{Eq. 4.1})$$

Values of the coefficients [n_C^0 , b_C , b_H , b_{CH} , b_O , and b_{CO}] are [1.96, 61.99, -113.33, 28.74, 0, 0] for CH compounds and [12.13, 10.95, -41.82, 21.61, 118.96, -24.38] for CHO compounds (DeRieux et al., 2018). This parameterization can be used to predict the glass transition temperature of compounds with molar mass up to $\sim 1100 \text{ g mol}^{-1}$.

Next, the T_g of the SOA under dry conditions ($T_{g,SOA}$) was estimated using the Gordon-Taylor equation assuming a Gordon-Taylor constant (k_{GT}) of 1 (Dette et al., 2014; Koop et al., 2011):

$$T_{g,SOA} = \sum_i w_i T_{g,i} \quad (\text{Eq. 4.2})$$

where w_i is the mass fraction of compound i . Following DeRieux et al. (2018), it was assumed that w_i values were proportional to the relative abundances in the combined mass spectra dataset, I_i (Eq. 4.3), which is a known limitation of this approach:

$$w_i = I_i \quad (\text{Eq. 4.3})$$

T_g of organic-water mixtures ($T_{g,mix}$) was then calculated by the Gordon-Taylor equation:

$$T_{g,mix} = \frac{w_{SOA} T_{g,SOA} + w_{H_2O} T_{g,H_2O} k_{GT}}{w_{SOA} + w_{H_2O} k_{GT}} \quad (\text{Eq. 4.4})$$

where w_{SOA} and w_{H2O} are the weight fractions of the SOA and water and $T_{g,H2O}$ is the glass transition temperature of water. A value of 2.5 was used for k_{GT} (Koop et al., 2011; Zobrist et al., 2008) and a value of 136 K was used for $T_{g,H2O}$ (Kohl et al., 2005).

The value of w_{SOA} can be calculated based on the mass concentration of water (m_{H2O}) and the SOA (m_{SOA}):

$$w_{SOA} = \frac{m_{SOA}}{m_{SOA} + m_{H2O}} \quad (\text{Eq. 4.5})$$

Under humid conditions, m_{H2O} was estimated using the effective hygroscopicity parameter (κ) and Eq. 4.6 (Petters and Kreidenweis, 2007):

$$m_{H2O} = \frac{\kappa \rho_w m_{SOA}}{\rho_{SOA} \left(\frac{1}{a_w} - 1 \right)} \quad (\text{Eq. 4.6})$$

where ρ_w and ρ_{SOA} are the densities of water and the SOA, and a_w is the water activity, which corresponds to RH/100. The density of the SOA particles was assumed to be 990 kg m^{-3} (Tasoglou and Pandis, 2015) and the hygroscopicity parameter was assumed to be 0.04-0.001 (Asa-Awuku et al., 2009; Frosch et al., 2013).

Viscosity as a function of temperature (T) was then calculated from $T_{g,mix}$ using the modified Vogel-Fulcher-Tammann (VFT) equation (DeRieux et al., 2018):

$$\eta = \eta_{\infty} e^{\frac{T_0 D_f}{T - T_0}} \quad (\text{Eq. 4.7})$$

where η_{∞} is the viscosity at infinite temperature, T_0 is the Vogel temperature and D_f is the fragility parameter. This equation is similar to the WLF equation introduced in Chapter 3 and provides an empirical relationship between viscosity and temperature. The VFT equation has been shown to fit the temperature dependence of viscosity of organic compounds (Angell, 2002) and organic water mixtures (Longinotti and Corti, 2008; Marsh et al., 2018; Recondo et al., 2006).

Equation 4.7 includes the parameter D_f which describes the fragility (strong or fragile) of the glass former (Angell, 1997). Large values for D_f corresponding to strong glass formers and small values corresponding to fragile glass formers. The fragility parameters for organic compounds are typically in the range of ~5-30 (Angell, 1997). Furthermore, for molar masses $> 200 \text{ g mol}^{-1}$, D_f is typically in the range of 5-20 and approaches a limit of ~10 at molar masses $> 400 \text{ g mol}^{-1}$ (DeRieux et al., 2018). As a result, a value of 10 was assumed for D_f . The value of D_f is assumed to be independent of RH (DeRieux et al., 2018; Marsh et al., 2018; Rothfuss and

Petters, 2017a; Shiraiwa et al., 2017b). This assumption is consistent with previous studies that found that the value of D_f in sucrose and citric acid were independent of water content, except for anhydrous sucrose (Angell, 2002; Kasparoglu et al., 2020; Longinotti and Corti, 2008). The viscosity at infinite temperature was assumed to be 10^{-5} Pa s based on previous studies (Angell, 1991, 2002).

The Vogel temperature can be calculated using Eq. 4.8:

$$T_0 = \frac{39.17 T_{g,mix}}{D_f + 39.17} \quad (\text{Eq. 4.8})$$

Equation 4.8 was obtained by solving the VFT equation where $T=T_g$, using a viscosity of 10^{12} Pa s as the viscosity of a glass.

4.2.5 Prediction of viscosity using a mole-fraction based Arrhenius mixing rule

The viscosities of SOA as a function of RH can also be estimated using the measured viscosities of pure water and dry SOA and mixing rules. In the following, a mole-fraction based Arrhenius mixing rule is tested for predicting the viscosity of β -caryophyllene SOA as a function of RH. This mixing rule is expressed for this system using the following equation (Zhud, 2014):

$$\ln(\eta) = x_{SOA} \ln(\eta_{SOA,dry}) + x_{H_2O} \ln(\eta_{H_2O}) \quad (\text{Eq. 4.9})$$

where η is the viscosity of the SOA and water mixture, $\eta_{SOA,dry}$ is the viscosity of the dry SOA, η_{H_2O} is the viscosity of pure water, x_{SOA} is the mole fraction of SOA in the SOA-water mixture, and x_{H_2O} is the mole fraction of water in the SOA-water mixture. A value of 1×10^7 Pa s was used for the viscosity of the dry SOA (which is based on the experimental data), and a value of 10^{-3} Pa s was used for the viscosity of pure water (Crittenden et al., 2012). The mole fractions of SOA and water were calculated from the weight fractions of SOA and water using Eq. 4.10:

$$x_{SOA} = \frac{\frac{w_{SOA}}{M_{SOA}}}{\frac{w_{SOA}}{M_{SOA}} + \frac{w_{H_2O}}{M_{H_2O}}} \quad (\text{Eq. 4.10})$$

where w_{SOA} and w_{H_2O} are the weight fractions of the SOA and water, respectively, and M_{SOA} and M_{H_2O} are the molecular weights of SOA and water, respectively. For the average molecular weight of the SOA a value of 271.0 g mol^{-1} was used based on the mass spectra and Eq. 4.13 (see below). The weight fraction of the SOA and water were estimated from the water activity using Eq. 4.5 and 4.6, a SOA density of 990 kg m^{-3} (Tasoglou and Pandis, 2015), and CCN-derived

kappa values of 0.04-0.001 for SOA generated from the ozonolysis of β -caryophyllene in the presence of an OH scavenger (Asa-Awuku et al., 2009; Frosch et al., 2013).

4.3 Results and discussion

4.3.1 Viscosity as a function of RH

Values of the experimental flow time, $\tau_{exp, flow}$, as a function of RH were determined from each of the poke-flow measurements (Fig. 4.5a). The $\tau_{exp, flow}$ values increased from ~48 seconds at 48% RH to ~2.5 h at 0% RH. Using the $\tau_{exp, flow}$ values and the particle dimensions, upper and lower limits for the viscosities were determined from fluid flow simulations (Fig. 4.5b). At an RH of 0% the viscosity was between 6.2×10^5 - 9.6×10^7 Pa s and at a RH of 48% the viscosity was between 1.3×10^3 - 2.8×10^5 Pa s. As mentioned in Section 2.2.2, the large uncertainty in the viscosity measurements is primarily the result of the range of possible literature values for the simulation input parameters. Some other types of SOA previously investigated with the poke-flow technique were more sensitive to RH over the same RH range. For example, the viscosity of SOA generated by the photooxidation of toluene is $>10^8$ Pa s at 17% RH, but $\sim 10^3$ - 10^4 Pa s at ~50% RH (Fig. 4.5b) (Song et al., 2016a). The weaker dependence on RH in the current experiments compared to toluene SOA is most likely because β -caryophyllene SOA has a lower hygroscopicity ($\kappa = 0.04$ - 0.001) (Asa-Awuku et al., 2009; Frosch et al., 2013) than toluene SOA ($\kappa = 0.1$ - 0.25) (Ruiz et al., 2015). Water acts as a plasticizer for SOA (i.e., as water content increases viscosity decreases) (Koop et al., 2011) and the smaller hygroscopicity of β -caryophyllene SOA likely translates into a weaker dependence of viscosity on RH over the range of RH values investigated.

A few previous studies investigated particle rebound as a function of RH for SOA from sesquiterpenes (Li et al., 2015; Pajunoja et al., 2015). The rebound studies were used to infer whether the SOA was in a liquid (viscosity $\lesssim 10^2$ Pa s) or a non-liquid state (viscosity $\gtrsim 10^2$ Pa s). Li et al. (2015) inferred that the non-liquid to liquid transition occurred at an RH $> 90\%$ for SOA generated by the photooxidation of β -caryophyllene. Pajunoja et al. (2015) inferred that the transition occurred at a RH of 70-90% for SOA from longifolene photooxidation, with the exact value depending on O:C. These studies are consistent with the current results.

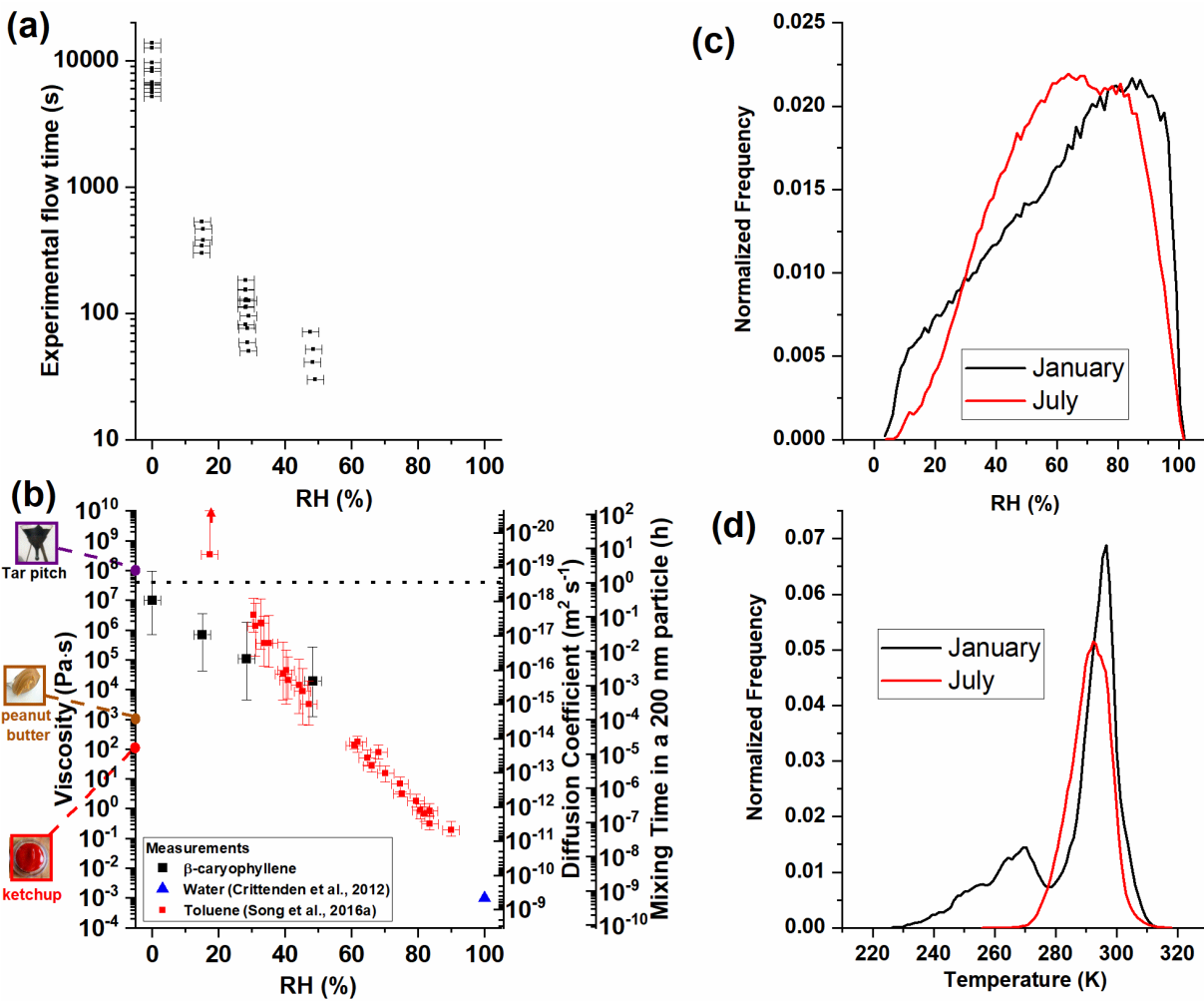


Figure 4.5: Panel A shows the experimental flow time, $\tau_{\text{exp, flow}}$, for poked particles as a function of RH. Panel B shows simulated viscosities, diffusion coefficients and mixing times of organic molecules in a 200 nm particle. The x-error bars correspond to uncertainties in the RH measurements and in panel B the y-error bars correspond to the upper and lower limits of the simulated viscosities at each RH and represent the uncertainties in the experimental flow times as well as the uncertainties in the parameters used to simulate the viscosities. The dotted line corresponds to a mixing time of 1 h. Also included in panel B are literature viscosity values for toluene SOA (Song et al., 2016a). Pictures of common substances have been added to panel B as points of reference per Koop et al. (2011). The tar pitch image is from the tar pitch experiment (image courtesy of Wikimedia Commons, GNU Free Documentation License, University of Queensland, John Mainstone). Panels C and D show the RH and temperature frequency distributions in the planetary boundary layer when the organic aerosol average concentration is $> 0.5 \mu\text{g m}^{-3}$ at the surface based on GEOS-Chem (Ullmann et al., 2019).

4.3.2 Diffusion coefficients and mixing times of organic molecules within β -caryophyllene SOA as a function of RH

Diffusion coefficients of organic molecules within SOA can be calculated from viscosity measurements using the Stokes-Einstein equation (Evoy et al., 2019; Price et al., 2016) or the fractional Stokes-Einstein equation (Evoy et al., 2019, 2020; Price et al., 2016). A recent study showed that diffusion coefficients predicted with the Stokes-Einstein equation were in reasonable agreement with measured diffusion coefficients in most cases when the radius of the diffusing molecules (R_{diff}) was greater than or equal to the radius of the matrix molecules (R_{matrix}) and when the viscosities were between 10^{-3} and 10^6 Pa s (Evoy et al., 2020). A more recent study showed that the fractional Stokes-Einstein equation was able to predict 98% of observed diffusion coefficients roughly within the uncertainty of the measurement for R_{diff}/R_{matrix} values ranging from 0.31 to 1.75 and viscosities ranging from 10^{-3} to 10^{10} Pa s. Based on these findings, the fractional Stokes-Einstein equation was used to predict diffusion of organic molecules within the SOA (Easteal, 1990):

$$D = D_0 * \left(\frac{\eta_0}{\eta}\right)^\xi \quad (\text{Eq. 4.11})$$

where ξ is the fractional exponent, η is the viscosity, η_0 is the viscosity of pure water (10^{-3} Pa s at a temperature of 293 K), and D_0 is the diffusion coefficient in pure water, calculated using the Stokes-Einstein equation (Eq. 1.1). A radius of 0.47 nm was assumed for the diffusing molecule, based on a molecular weight of 254 g mol^{-1} for some common first generation β -caryophyllene ozonolysis products (Li et al., 2011), a density of 990 kg m^{-3} (Tasoglou and Pandis, 2015), and an assumed spherical geometry of the diffusing molecule. The value of ξ was calculated using Eq. 4.12 (Evoy et al., 2020):

$$\xi = 1 - \left[A \exp\left(-B \frac{R_{diff}}{R_{matrix}}\right) \right] \quad (\text{Eq. 4.12})$$

where A corresponds to 0.73 and B corresponds to 1.79 (Evoy et al., 2020). A value of 1 was assumed for R_{diff}/R_{matrix} . Based on the fractional Stokes-Einstein equation, the diffusion coefficients ranged from $\sim 2 \times 10^{-16} \text{ m}^2 \text{ s}^{-1}$ at 48% RH to $\sim 9 \times 10^{-19} \text{ m}^2 \text{ s}^{-1}$ at 0% RH (Fig. 4.5b, secondary Y-axis).

Diffusion coefficients were converted into characteristic mixing times of organic molecules within 200 nm SOA particles using Eq. 1.2 (Seinfeld and Pandis, 2006).

As mentioned in Chapter 1, the mixing time calculated using Eq. 1.2 corresponds to the time it takes for the concentration of the diffusing molecules at the centre of the SOA particle to be approximately $1/e$ of the equilibrium concentration for non-reactive partitioning (Zaveri et al., 2014). The SOA particle was assumed to have a diameter of 200 nm as that is roughly the median diameter in the volume distribution of ambient SOA-containing particles (Martin et al., 2010; Pöschl et al., 2010; Riipinen et al., 2011). The calculated mixing times ranged from ~ 0.4 h at 0% RH to < 6 sec at 48% RH (Fig. 4.5b, secondary Y-axis).

As mentioned in Chapter 3, chemical transport models typically assume the mixing times within SOA are less than ~ 1 h (Hallquist et al., 2009). Based on these results, the mixing time within a 200 nm β -caryophyllene SOA is < 1 h when the RH is $\geq 15\%$ RH (Fig. 4.5b) and the temperature is 292-294 K. Based on previous calculations, the RH in the PBL is nearly always $\geq 15\%$ RH when the organic aerosol concentrations are $> 0.5 \mu\text{g m}^{-3}$ at the surface (Fig. 4.5c). The temperature in the PBL is most often 280-290 K when the organic aerosol concentrations are $> 0.5 \mu\text{g m}^{-3}$ at the surface (Fig. 4.5d). Hence, the mixing times within β -caryophyllene SOA are < 1 h for a large majority of RH and temperature conditions in the PBL when the organic aerosol concentrations are $> 0.5 \mu\text{g m}^{-3}$ at the surface. Conditions where the organic aerosol concentrations were $< 0.5 \mu\text{g m}^{-3}$ were excluded, as aerosols at low concentrations are expected to be of less importance to climate or visibility.

One caveat to the discussion above is that the mass concentration of the SOA generated in the environmental chamber was $\sim 150 \mu\text{g m}^{-3}$, which is higher than typical mass concentrations of biogenic SOA in the atmosphere (Raatikainen et al., 2010; Spracklen et al., 2011). Previous studies have shown that for some types of SOA the viscosity, and hence mixing times, increases with a decrease in mass concentration of SOA in the reactor (Champion et al., 2019; Grayson et al., 2016; Jain et al., 2018). Reducing the SOA mass concentration removes compounds with higher vapour pressures from the particles (Donahue et al., 2009). These higher vapour pressure compounds have lower glass transition temperatures (DeRieux et al., 2018; Shiraiwa et al., 2017b). Additional studies are needed to determine the effect of SOA mass concentration on the viscosity of β -caryophyllene SOA.

Related to the mixing times shown in Fig. 4.5b, Ye et al. (2018) investigated the mixing of semi-volatile vapours from α -pinene SOA and toluene SOA within β -caryophyllene SOA (formed by ozonolysis, as in the current experiments). In these experiments, β -caryophyllene

SOA took up only a small amount of semi-volatile vapours ($\leq 10\%$ change in β -caryophyllene SOA mass) over a period of 2 h at 50 % RH. The authors suggested two possible explanations for the limited uptake of the semi-volatile vapours: 1) diffusion limited uptake and 2) immiscibility (e.g. non-ideality) of semi-volatile vapours from α -pinene SOA and toluene SOA within β -caryophyllene SOA (Ye et al., 2018). The size of SOA particles studied by Ye et al. (2018) ranged from 200-700 nm in diameter. Using the method discussed above, the mixing times of organic molecules within 450 nm β -caryophyllene SOA particles were calculated as a function of RH (Fig. 4.6).

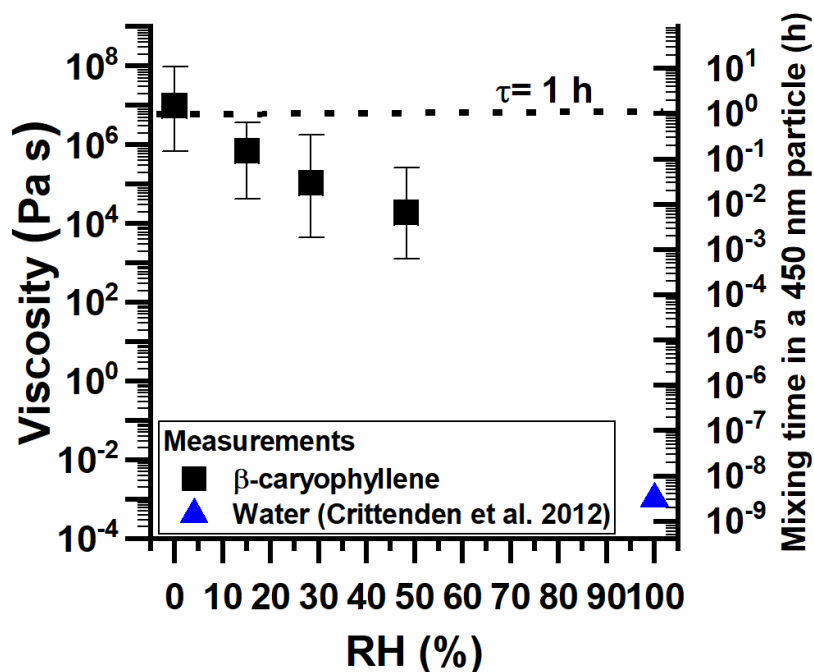


Figure 4.6: Viscosities of β -caryophyllene SOA and calculated mixing times within a 450 nm β -caryophyllene SOA particle. The y-error bars correspond to the upper and lower limits of the simulated viscosities at each RH and represent the uncertainties in the experimental flow times used to simulate the viscosity as well as the uncertainties in the parameters used to simulate the viscosities. The x-error bars correspond to uncertainties in the RH measurements. The horizontal line corresponds to a mixing time of 1 h.

Based on these calculations, the mixing times of organic molecules within a 450 nm β -caryophyllene SOA particle at 48% RH is 2.2 - 250 s. These calculations suggested that the limited uptake of semi-volatile vapours from α -pinene SOA and toluene SOA within β -caryophyllene SOA observed by Ye et al. (2018) was due to immiscibility rather than diffusion

limited uptake. However, Ye et al. (2018) used SOA generated with mass concentrations of 3.4 - 6.4 $\mu\text{g m}^{-3}$, compared to the mass loading of 50 - 60 $\mu\text{g m}^{-3}$ used in this study. Since viscosity can increase with a decrease in SOA mass concentration, the SOA studied by Ye et al. (2018) may have been more viscous than the SOA in the current study, leading to longer mixing times than calculated from this data.

4.3.3 Chemical composition of the SOA based on mass spectrometry

The full mass spectra are shown in Fig. B.3 and relative peak abundances from the mass spectra are shown in Fig. 4.7 as a function of carbon number. β -caryophyllene ($\text{C}_{15}\text{H}_{24}$) is expected to produce mainly C14-C15 compounds during ozonolysis, but smaller compounds resulting from more extensive backbone fragmentation and larger compounds resulting from oligomerization are also possible. Close examination of the mass spectra suggested that there was more in-source ion fragmentation during ESI and nano-ESI ionization compared to the nano-DESI ionization.

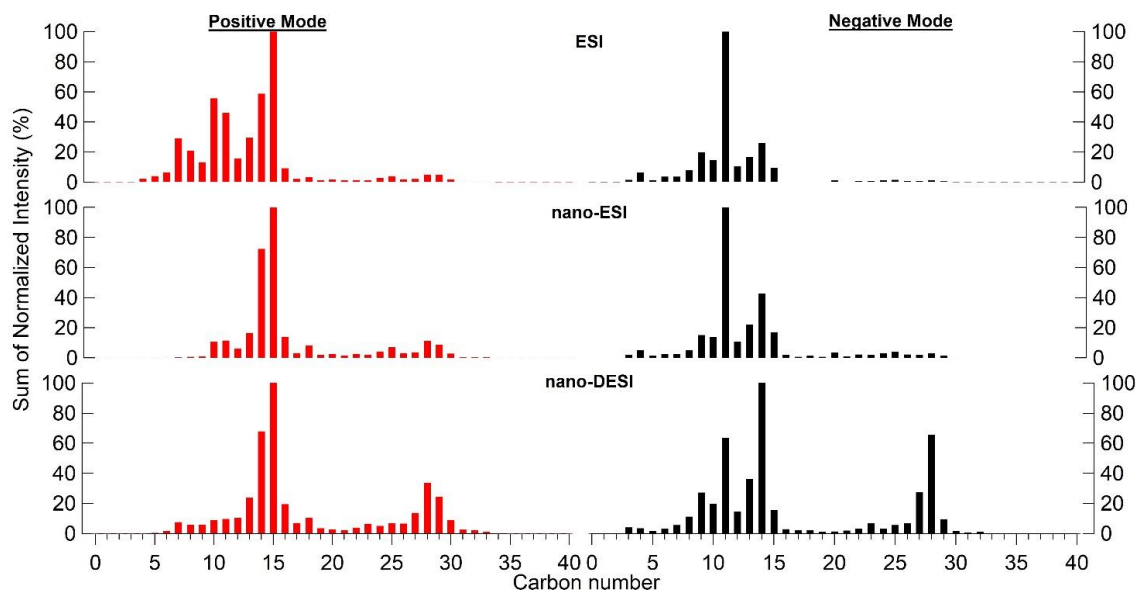


Figure 4.7: Total intensity of all molecular formula assignments based on carbon number for three ionization techniques (ESI, nano-ESI, and nano-DESI). In-source fragmentation resulted in increased abundance of smaller carbon compounds when using ESI and nano-ESI compared to nano-DESI.

The fragmentation is especially noticeable in the positive ion mode ESI data, manifesting itself in unexpectedly high peak abundances in C5-C10 compounds. A recent study of organic

compounds in ambient particles also found more in-source fragmentation for the ESI source (Kourtchev et al., 2020). In the negative ion mode spectra, the fragmentation shifted the peak abundance from the expected C14-C15 compounds in nano-DESI to smaller compounds in ESI and nano-ESI. The ionization mechanism for nano-DESI has been shown to be better suited for the detection of chemically-labile compounds compared to ESI and nano-ESI (Roach et al., 2010). Therefore, the remainder of the document will focus on the nano-DESI results to minimize the effect of in-source fragmentation on the data analysis.

Shown in Fig. 4.8 is the nano-DESI mass spectra, with the five most abundant peaks in the positive and negative mode identified. Approximately 1000 peaks were observed in positive mode compared to 700 peaks observed in negative mode. β -caryophyllene has two double bonds (Fig. 4.1) and attack by ozone on the more reactive endocyclic double bond will generally lead to ring-opening products retaining the C15 carbon number. Attack on the less reactive exocyclic double bond generally leads to C14 products. Indeed, the most abundant peaks in the positive ion mode mass spectra were C14 and C15 species. It is common to observe $C_{15}H_{24}O_n$ products in mass spectra of oxidized sesquiterpenes (Klodt et al., 2019; Romonosky et al., 2017). The major C15 products identified include $C_{15}H_{24}O_4$ and $C_{15}H_{24}O_5$, which have been reported as first generation ozonolysis products (Jaoui and Kamens, 2003a; Li et al., 2011). Some of the major C14 products identified include $C_{14}H_{22}O_4$, $C_{14}H_{22}O_5$, and $C_{14}H_{22}O_7$, which have been reported as second generation ozonolysis products (Jaoui and Kamens, 2003a; Li et al., 2011). The $C_{14}H_{22}O_9$ product was previously reported in Richters et al. (2016) as a highly oxidized reaction product of β -caryophyllene ozonolysis formed via an extended autoxidation pathway.

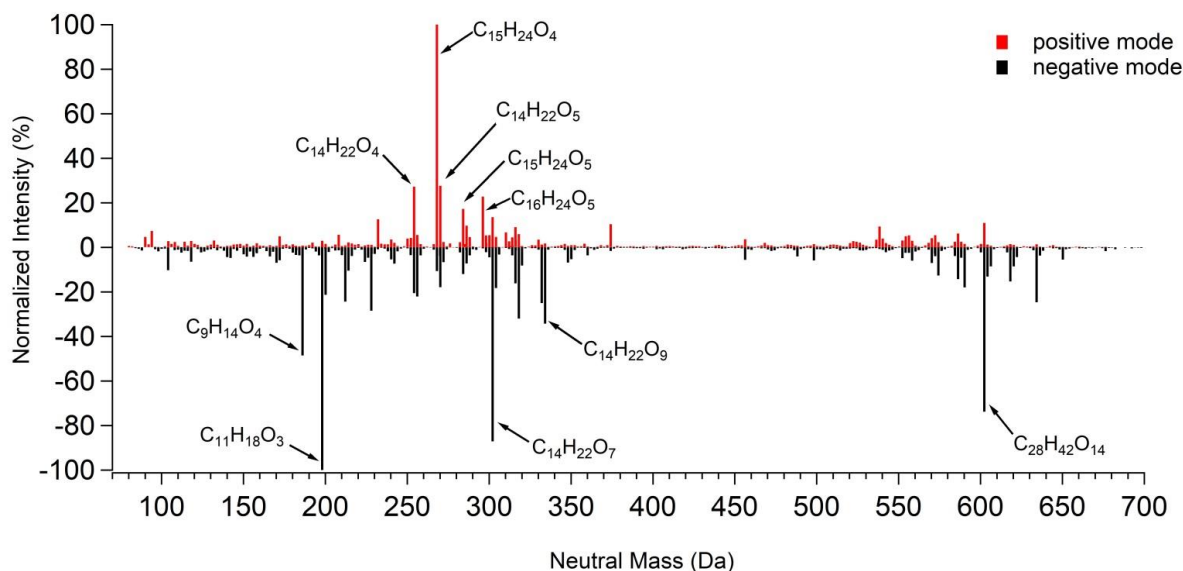


Figure 4.8: nano-DESI mass spectrum taken in positive mode (red spectrum) and negative mode (black spectrum). The signals were normalized to the highest intensity in each respective mode. The five most abundant peaks in each mode are labelled by the corresponding neutral (unionized) molecular formulas.

In addition to C14 and C15 species, other carbon numbers were also observed, which result from fragmentation of Criegee intermediates during ozonolysis, other radical driven secondary chemistry, and oligomerization processes occurring in the gas and particle phase. The C11 product $C_{11}H_{18}O_3$ has been reported as a second generation ozonolysis products of β -caryophyllene (Jaoui and Kamens, 2003a; Li et al., 2011). The C28 peak $C_{28}H_{42}O_{14}$ has more carbons than β -caryophyllene, indicating the formation of oligomers from β -caryophyllene oxidation products. Some other major peaks include $C_9H_{14}O_4$, and $C_{16}H_{24}O_5$, which have not been reported previously and are likely second or third generation products. These two compounds have O:C ratios of 0.44 and 0.31, respectively, which is consistent with O:C ratios of second generation products (Li et al., 2011).

4.3.4 Viscosity predictions from the measured chemical composition

For viscosity predictions, the nano-DESI mass spectrometry results were used, since the least amount of fragmentation occurred for this method of ionization, based on Fig. 4.7. It was assumed that the mass fraction of each compound was proportional to its relative peak abundance in the combined mass spectra dataset (Eq. 4.3) (DeRieux et al., 2018). The

predictions based on this assumption and the nano-DESI results drastically overpredicted the viscosity (Fig. 4.9a). For example, for dry conditions, the predicted viscosities were up to six orders of magnitude larger than the measured viscosities.

ESI based methods are known to be more sensitive to larger, oligomeric compounds (Kenseth et al., 2020; Nguyen et al., 2013), and this may be the reason, at least in part, for the discrepancy between the measured viscosity and predicted viscosity. To investigate if this may be important to this study, as a second step in the analysis, an approach based on the work of Nguyen et al. (2013) was used to predict the mass fraction of each compound in the SOA:

$$w_i = \frac{I_i}{H/C_i * M_i} \quad (\text{Eq. 4.13})$$

where M_i is the molecular weight of the compound, H/C_i is the hydrogen-to-carbon ratio of the compound, and $H/C_i \times M_i$ is the adjusted mass. This adjusted mass scaling was used to approximately account for the impact of molecular weight and degree of unsaturation (represented by the H/C ratio) on the ionization efficiency of the individual compounds. This is the same relation developed by Nguyen et al. (2013) based on the addition of calibration standards to a realistic SOA matrix, except Nguyen et al. (2013) included a term to account for the limit of detection (LOD) of the compounds, which was found to inversely correlate with molecular weight and found to be small for compounds when the adjusted mass was > 200 Da. In the absence of better information, the LOD term was neglected as more than 90 % of the compounds detected via mass spectrometry have an adjusted mass > 200 Da.

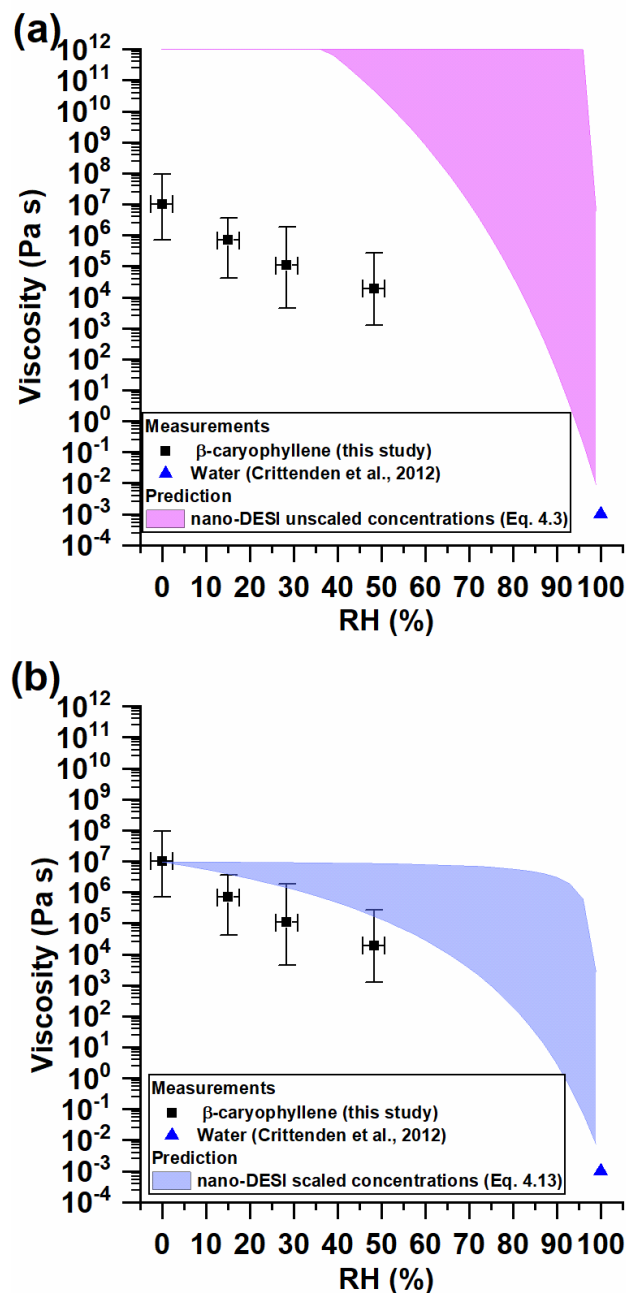


Figure 4.9: Comparison of measured and predicted viscosities as a function of RH. The x-error bars correspond to uncertainties in the RH measurements, and the y-error bars correspond to the upper and lower limits of the simulated viscosities at each RH and represent the uncertainties in the experimental flow times used to simulate the viscosity as well as the uncertainties in the parameters used to simulate the viscosities. Panel A shows the viscosity predictions using the averaged positive and negative ion mode mass spectrometry data where it was assumed that the weight fraction of the individual SOA species was proportional to the mass spectrum signal intensities (Eq. 4.3). Panel B shows the viscosity predictions using the averaged mass spectrometry data assuming a relation between weight fraction and intensity given in Eq. 4.13.

The viscosities predicted using Eq. 4.13 better overlapped with the measured viscosities within the uncertainties in both viscosity measurements and the RH measurements (Fig. 4.9b). It is especially remarkable that the predicted viscosity matches with the measured value very well at 0% RH, indicating that the T_g parameterization and prediction method (Eq. 4.1 and 4.2) works well. This suggests that the poor agreement between the measured viscosities and the initial predictions (assuming linearity between w_i and I_i), may be due to the enhanced sensitivity of ESI methods to larger molecular weight compounds. Interestingly, in previous studies using toluene SOA and diesel fuel SOA, a reasonable agreement between measured viscosities and predictions was observed when assuming a linear relation (i.e. Eq. 4.3) (DeRieux et al., 2018; Song et al., 2019). To investigate this further, these comparisons were redone using Eq. 4.3 and Eq. 4.13. The results show that using the relation in Eq. 4.13 results in similar or improved predictions of the viscosity compared to Eq. 4.3 for both the toluene SOA and diesel fuel SOA (Fig. B.4-B.5), consistent with the trend observed for β -caryophyllene SOA (although the difference in the predicted results is not nearly as dramatic as for β -caryophyllene SOA).

The ultimate data set for viscosity predictions would be a full roster of the actual (rather than estimated) mass fractions of all SOA compounds. Because of the overwhelmingly large number of SOA compounds and lack of appropriate calibration standards, no existing experimental method can provide such a data set. However, the analysis suggests that an approximate estimation of mass fractions based on Eq. 4.13 can work reasonably well for the purposes of predicting material viscosity. Specifically, it has been shown that nano-DESI can be used with Eq. 4.1-4.2 and 4.4-4.8 and the relation between w_i and I_i shown in Eq. 4.13 to provide an improved prediction for viscosity for toluene SOA, diesel fuel SOA, and β -caryophyllene SOA compared to using the assumption in Eq. 4.3. However, this method is currently limited in its precision as the precise values of several parameters such as hygroscopicity are not known.

4.3.5 Viscosity predictions from the mole-fraction based Arrhenius mixing rule

The viscosities of SOA as a function of RH were also estimated using a mole-fraction based Arrhenius mixing rule (Eq. 4.9) and the measured viscosities of pure water and dry SOA. For the viscosity of the dry SOA, a value of 1×10^7 Pa s was used (which is consistent with experimental data) and a viscosity of pure water of 10^{-3} Pa s (Crittenden et al., 2012).

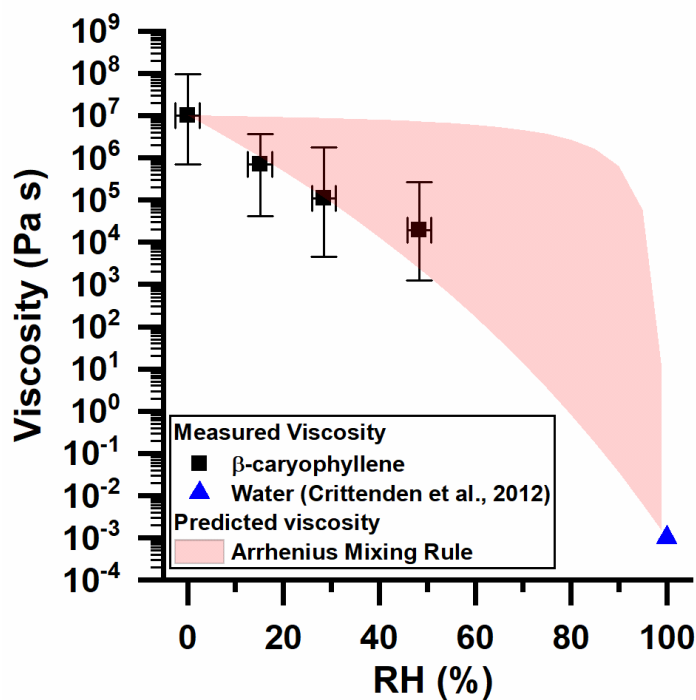


Figure 4.10: Measured viscosities and predicted viscosities using a mole-fraction based Arrhenius mixing rule. For the measurements, the x-error bars correspond to uncertainties in the RH, and the y-error bars correspond to the upper and lower limits of the simulated viscosities at each RH and represent the uncertainties in the experimental flow times used to simulate the viscosity as well as the uncertainties in the parameters used to simulate the viscosities. The uncertainties in the predictions are due to uncertainties in the hygroscopicity of the SOA. For the hygroscopicity, a range of CCN-derived kappa values of 0.04-0.001 was used (Asa-Awuku et al., 2009; Frosch et al., 2013).

The predictions based on this approach overlapped with the measured viscosities (Fig. 4.10). This is consistent with the recent studies by Gervasi et al. (2020), who showed a mole-fraction based mixing rule is the best choice among simple mixing rules for predicting viscosity in binary aqueous systems. These predicted viscosities had large uncertainties for RH values ranging from approximately 30 to 95 %, mainly due to the large uncertainty in the κ values used to predict the mole fraction of water in the SOA. The predictions based on the chemical composition and the method from DeRieux et al. (2018) (Fig. 4.9) also had large uncertainties at similar RH values for the same reason. This highlights that accurate and precise measurements of κ values for SOA are needed to improve predictions of viscosity of SOA as a function of RH.

4.4 Summary and conclusions

Viscosity was measured as a function of RH at room temperature for SOA generated via the ozonolysis of β -caryophyllene. The viscosity increased from $1.3 \times 10^3 - 2.8 \times 10^5$ Pa s at 48% RH to $6.2 \times 10^5 - 9.6 \times 10^7$ Pa s at 0% RH, where the ranges correspond to both measurement and data analysis uncertainties. Diffusion coefficients were calculated from the viscosities using the fractional Stokes-Einstein equation and ranged from $\sim 2 \times 10^{-16} \text{ m}^2 \text{ s}^{-1}$ at 48% RH to $\sim 9 \times 10^{-19} \text{ m}^2 \text{ s}^{-1}$ at 0% RH. Mixing times of organic molecules within 200 nm SOA particles were calculated from the diffusion coefficients and ranged from < 6 s at 48% RH to 0.4 h at 0% RH. Based on these values, mixing times within 200 nm β -caryophyllene SOA are fast (< 1 h) for RH and temperatures typically found in the PBL.

The chemical composition of the SOA was determined with nano-DESI mass spectrometry. The most abundant peaks in the mass spectra were C15 and C14 peaks, corresponding to the first and second generation ozonolysis products. Another abundant peak in the mass spectra was a C28 peak, likely the result of dimerization of the β -caryophyllene oxidation products. Other ionization sources, ESI and nano-ESI, resulted in more in-source fragmentation compared to nano-DESI.

The viscosity data and the chemical composition from mass spectrometry were used to test the accuracy of the method from DeRieux et al. (2018) for predicting the viscosity of β -caryophyllene SOA. Using raw peak abundances in the mass spectra as estimates of mass fractions led to a drastic overprediction of the viscosity by up to six orders of magnitude (depending on the RH). However, when the peak abundances were adjusted to account for the sensitivity of the electrospray ionization to larger molecular weight components using an empirical relationship suggested by Nguyen et al. (2013), the measured viscosity overlapped with predictions. Furthermore, the same method also produced better or similar predictions for previous observations of viscosity of toluene SOA and diesel fuel SOA. These results highlight the importance of the method used for relating peak abundances to relative concentrations in direct infusion mass spectrometry.

The accuracy of a mole-fraction based Arrhenius mixing rule was tested for predicting viscosity as a function of RH from the viscosity of water and the dry SOA. For this case, the predictions also overlapped with the measured data. However, predictions based on chemical

composition or a mole-fraction based mixing rule are limited in their precision due to uncertainties in parameters such as hygroscopicity.

Chapter 5: Global distribution of the phase state and mixing times within secondary organic aerosol particles in the troposphere based on room-temperature viscosity measurements

5.1 Introduction

As discussed in Chapter 1, SOA properties such as phase state, and the mixing time of water and organics are important for understanding the formation and growth of SOA as well as its impact on the climate. Global distributions of these properties are needed to be able to accurately model SOA using chemical transport models.

The phase state and mixing times of water and organic molecules within SOA or proxies of SOA have been investigated in many studies (Abramson et al., 2013; Bastelberger et al., 2017; Evoy et al., 2019, 2020; Gervasi et al., 2020; Grayson et al., 2016; Kiland et al., 2019; Li and Shiraiwa, 2019; Liu et al., 2016; Reid et al., 2018; Renbaum-Wolff et al., 2013; Song et al., 2016a; Virtanen et al., 2010; Zhang et al., 2019b; Zobrist et al., 2011). This work has shown that the glassy state can dominate, and mixing times of water and organics are slow in SOA and SOA proxies at low temperatures and low RHs (Gervasi et al., 2020; Li and Shiraiwa, 2019; Zhang et al., 2019b; Zobrist et al., 2011). Mixing times of organics within some types of SOA and SOA proxies can even exceed 1 h at room temperature if the RH is low ($\lesssim 25\%$) (Abramson et al., 2013; Renbaum-Wolff et al., 2013; Song et al., 2016a). However, studies assessing the global distributions of SOA phase states and mixing times within SOA are rare.

Chapter 3 investigated the global distribution of mixing times of organic molecules within SOA for the planetary boundary layer (PBL). To predict mixing times, a parameterization of viscosity as a function of temperature and RH was developed based on room temperature and low temperature viscosity measurements. It was found that mixing times of organic molecules are most often < 1 h in the PBL.

Shiraiwa et al. (2017b) investigated the global distribution of the phase state and mixing times of water and organics within SOA for both the PBL and the free troposphere (FT) using a parameterization that related the glass transition temperature (T_g) to molar mass and the oxygen-to-carbon ratio (O:C) of the SOA components. They found that in the middle and upper FT, SOA are mostly in a glassy state and mixing times of water and organics most often exceed 1 h.

In this chapter, the global distribution of phase states and mixing times of water and organic molecules within SOA are investigated for both the PBL and FT, with a focus on the FT since Shiraiwa et al. (2017b) provides the only study in this region. The approach for calculating phase state and mixing times is different from Shiraiwa et al. (2017b) and Chapter 3. A parameterization was developed for the viscosity of biogenic and anthropogenic SOA as a function of RH and temperature based on literature room-temperature viscosities measured using the poke-flow technique (Smith et al., 2020; Song et al., 2016a). This information, together with RH and temperature fields in the troposphere was then used to estimate the global distribution of the phase state and mixing times in the PBL and FT. This method of parameterizing the viscosity allows for predictions of phase state and mixing times using datasets similar to the viscosity dataset shown in Chapter 4. Fewer parameters are required for these predictions compared to Shiraiwa et al. (2017b). For example, this method does not require the hygroscopicity or the Gordon-Taylor constants of the SOA, which have associated uncertainties leading to uncertainties in the predicted phase state and mixing times within SOA (Yli-Juuti et al., 2017). On the other hand, this method has other limitations, making these results complementary to Shiraiwa et al. (2017b). In the end, the results obtained from this approach are consistent with Shiraiwa et al. (2017b) and further illustrate the importance of the glass state and slow mixing times of water and organic molecules in the upper part of the FT.

5.2 Materials and methods

An overview of the method used to predict global distributions of SOA phase state and mixing times within SOA is shown in Fig. 5.1. First parameterizations were developed for the viscosity of biogenic and anthropogenic SOA as a function of RH and temperature based on laboratory viscosity measurements (Sections 5.2.1 and 5.2.2). Phase state and mixing times as a function of RH and temperature were then predicted from the viscosities (Section 5.2.3). Finally, global distributions of phase state and mixing times were determined using this information and average annual RH and temperature fields in the troposphere extracted from the ECHAM/Modular Earth Submodel System Atmospheric Chemistry (EMAC) model (Section 5.2.5) (Jöckel et al., 2006).

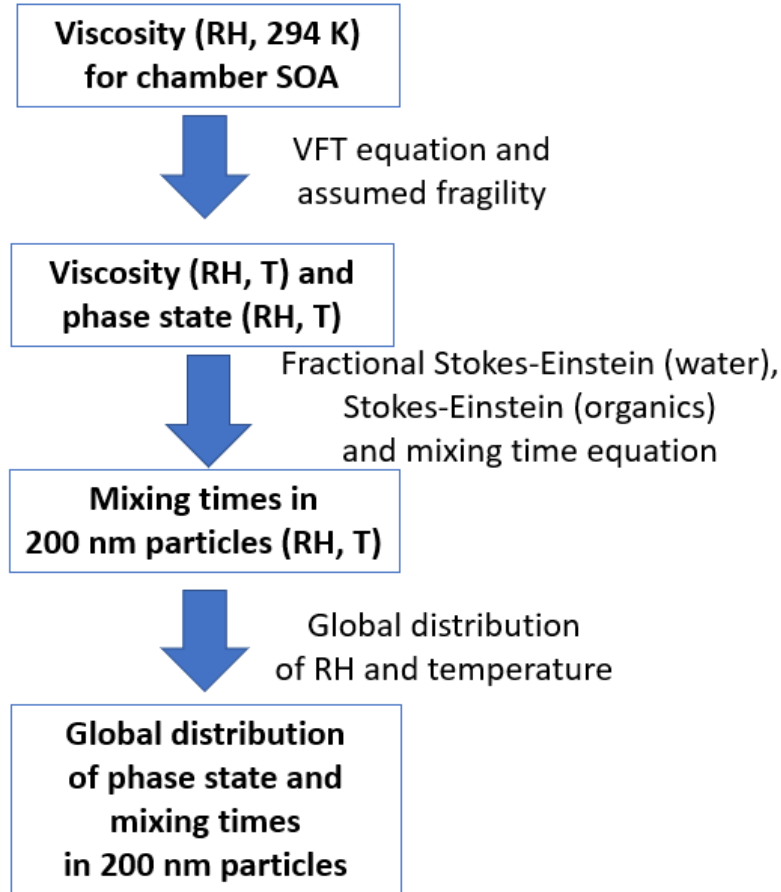


Figure 5.1: Overview of method used to calculate the global distribution of SOA phase state and the mixing times of water and organics within SOA particles.

5.2.1 Parameterization for the viscosity of biogenic SOA as a function of RH and temperature

To develop a parameterization for the viscosity of biogenic SOA as a function of RH and temperature, the following data was used: 1) measured room-temperature viscosity data of SOA generated by the photooxidation of a mixture of VOCs representing emissions from Scots pine trees (Smith et al., 2020) and 2) the room temperature viscosity data of water (Crittenden et al., 2012). This data is shown in Fig. 5.2. Pine trees are widely distributed throughout the boreal forest (Lundqvist et al., 2019), and Scots pine (*Pinus Sylvestris*) make up a significant portion of boreal forests in several European countries (Boratyński, 1991). As a result, Scots pine tree SOA should be a good proxy for SOA over boreal forests, which is one the largest ecosystems on

Earth. The applicability of these results to other types of biogenic SOA still needs to be determined.

To generate a parameterization for viscosity as a function of RH and temperature, the data in Fig. 5.2 was first fit piecewise to the following equations:

$$\log(\eta(RH, 294K)) = \begin{cases} ae^{\left(\frac{RH}{100}\right)^b} + c, & RH < 39.2 \% \quad (\text{Eq. 5.1}) \\ \left(1 - \frac{RH}{100}\right)d + \frac{RH}{100}e, & RH \geq 39.2 \% \quad (\text{Eq. 5.2}) \end{cases}$$

where $\eta(RH, 294K)$ is the RH-dependent viscosity at 294 K (i.e. room temperature) and a - e are fitting parameters. The fitting was done using the least squares method without any weighting from the error bars. The values for coefficients $[a, b, c, d, e]$ are $[-0.36 \pm 0.21, -0.21 \pm 0.05, 8.92 \pm 0.27, 12.93 \pm 0.34, -2.97 \pm 0.22]$, based on the fitting. The best fit curves are shown in Fig. 5.2 (solid line). Equations 5.1 and 5.2 were used since they both monotonically decrease as the RH increases and since they both fit the data well for their respective RH ranges. Equation 5.2 is equivalent to the mole fraction-based viscosity mixing rule used in Chapter 4 to predict the viscosity of β -caryophyllene (Eq. 4.9) (see Section C.1).

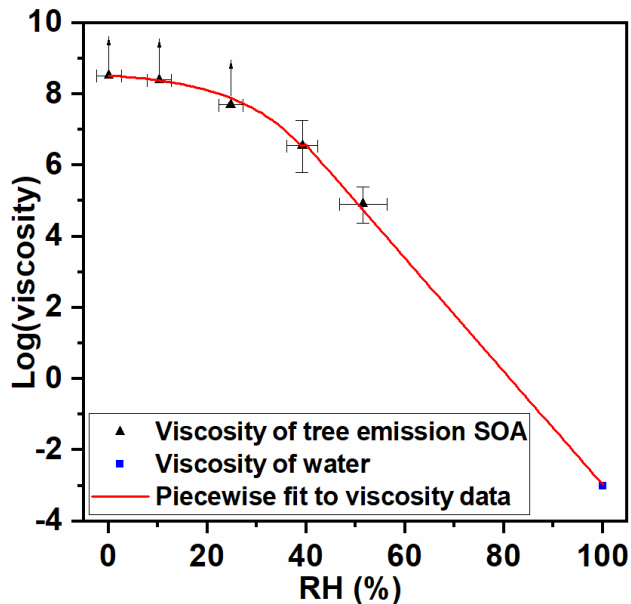


Figure 5.2: Log(viscosity) data from Smith et al. (2020) as a function of relative humidity for SOA produced via photooxidation of healthy tree emissions and the viscosity of pure water as well as a fit to the data using Eq. 5.1 and 5.2. The x-error bars represent uncertainties in the RH measurements and the y-error bars correspond to the 83% confidence interval for the upper and lower limit of viscosity. The points with upwards arrows correspond to data where only lower limits of viscosity were obtained.

To extrapolate the room-temperature viscosity data, $\eta(RH, 294K)$, to lower temperatures the VFT equation, previously introduced in Chapter 4, was used:

$$\eta = \eta_{\infty} e^{\frac{T_0 D_f}{T - T_0}} \quad (\text{Eq. 5.3})$$

where η_{∞} is the viscosity at infinite temperature, T_0 is the Vogel temperature and D_f is the fragility parameter. This is the same equation used by Shiraiwa et al. (2017b) to calculate viscosities as a function of temperature from T_g . Here, $T_0(RH)$ was calculated from the room-temperature viscosity parameterization discussed above by rearranging the VFT equation and evaluating at $T = 294$ K:

$$T_0(RH) = \frac{\ln\left(\frac{\eta(RH, 294 K)}{\eta_{\infty}}\right) 294 K}{D_f + \ln\left(\frac{\eta(RH, 294 K)}{\eta_{\infty}}\right)} \quad (\text{Eq. 5.4})$$

A value of 10^{-5} Pa s was used for η_{∞} (Angell, 1991, 2002). To be consistent with Shiraiwa et al. (2017b), a value of $D_f=10$ was assumed. As discussed previously, the fragility parameter for organic compounds is typically in the range of ~ 5 -30 (Angell, 1997). Furthermore, for molar masses > 200 g mol $^{-1}$, D_f is typically in the range of 5-20 and approaches a limit of ~ 10 at molar masses > 400 g mol $^{-1}$ (DeRieux et al., 2018). Once $T_0(RH)$ was calculated, $\eta(RH, T)$ was calculated using Eq. 5.3. It is assumed that the fragility is independent of RH as was done in Chapter 4. At lower temperatures, the viscosity values calculated using this approach increase by up to 10 orders of magnitude depending on the RH compared to the room temperature values.

5.2.2 Parameterization for the viscosity of anthropogenic SOA as a function of RH and temperature

To develop a parameterization for the viscosity of anthropogenic SOA as a function of RH and temperature the following data was used: 1) measured room-temperature viscosity data of SOA generated via the photooxidation of toluene (Song et al., 2016a) and 2) the room temperature viscosity data of water (Crittenden et al., 2012). This data is shown in Fig. 5.3. Aromatic hydrocarbons (including toluene) are an important source of SOA in urban environments (Gao et al., 2019; de Gouw et al., 2008), and toluene SOA is often used as a proxy for anthropogenic SOA (Pandis et al., 1992; Robinson et al., 2013), however anthropogenic SOA is likely more complex and can also be the result of non-aromatic VOCs such as alkanes (Gao et al., 2019; de Gouw et al., 2008; Song et al., 2019). To generate a parameterization for viscosity

of anthropogenic SOA as a function of RH and temperature, the data in Fig. 5.3 was first fit to an equation equivalent to a mole fraction-based viscosity mixing rule (Eq. 5.5):

$$\log(\eta(RH, 294K)) = \left(1 - \frac{RH}{100}\right)f + \frac{RH}{100}g \quad (\text{Eq. 5.5})$$

The fitting was done using the least squares method without any weighting from the error bars. The value of coefficients $[f, g]$ were $[9.89 \pm 0.20, -2.52 \pm 0.15]$, based on the fitting and the results of the fitting are included in Fig. 5.3 (solid line). Equation 5.5 was used to fit the data since it monotonically decreases as the RH increases and since it fit the data well. To extrapolate the room-temperature viscosity data, $\eta(RH, 294K)$, to lower temperatures, the same approach discussed above for biogenic SOA was used (Eq. 5.3 and 5.4).

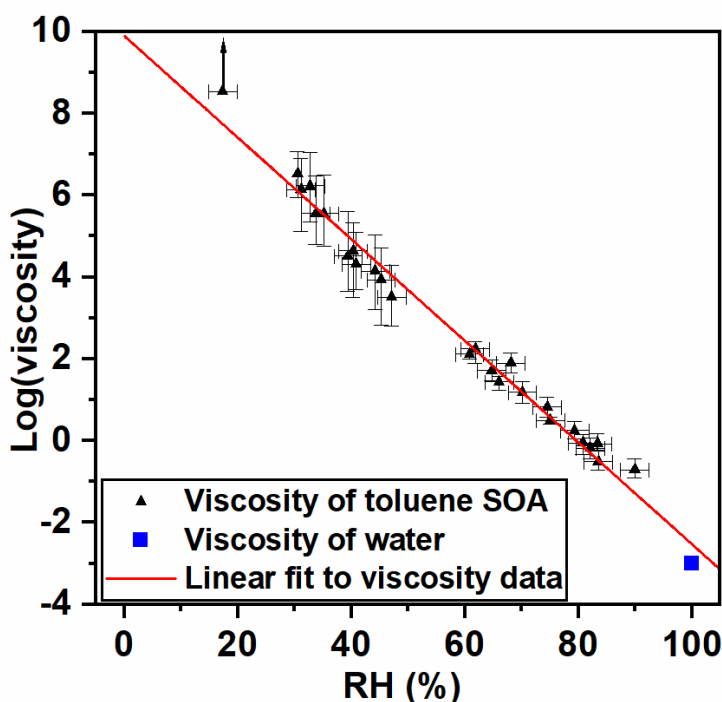


Figure 5.3: Log(viscosity) data from Song et al. (2016a) as a function of relative humidity for SOA produced via the photooxidation of toluene and the viscosity of pure water as well as a fit to the data using Eq. 5.5. The x-error bars represent uncertainties in the RH measurements and the y-error bars correspond to the upper and lower limits of the viscosities. The point with an upwards arrow corresponds to data where only a lower limit of viscosity was obtained.

5.2.3 Predicting phase state and mixing times

The phase state of the SOA can be determined from the viscosity. To determine if the SOA is in a glassy state, the glass transition temperature of the SOA as a function of RH was

first calculated by evaluating the VFT equation (Eq. 5.3) at the glass transition temperature ($T=T_g$ and $\eta=10^{12}$ Pa s) (Angell, 1991, 2002; DeRieux et al., 2018):

$$T_g(RH) = \frac{T_o(RH)*(D_f+39.17)}{39.17} \quad (\text{Eq. 5.6})$$

where $T_g(RH)$ is the RH-dependent glass transition temperature of the SOA. This equation is equivalent to Eq. 4.8. It is assumed that the SOA and water remain miscible and consist of a single phase without the water freezing out. It has been shown that in organic-water mixtures, the viscosity upon cooling is high enough to prevent ice from forming up to water activities of ~ 0.85 (correspond to an RH of 85%, with the exact RH depending on the organic compound) (Zobrist et al., 2008). Pure water homogeneously freezes in the atmosphere at ~ 236 K, but the presence of organic molecules depresses the freezing point. For example, it has been shown for several organic-water mixtures that the freezing temperature of water in super cooled particles is ~ 200 K at a water activity of ~ 0.85 (Zobrist et al., 2008). As a result, even if the water activity is high enough that water in the SOA could homogeneously freeze, the temperature may not be low enough. For the purpose of these calculations, it is assumed that the water remains unfrozen. Next the ratio of $T_g(RH)/T$ was evaluated, and a $T_g(RH)/T$ value ≥ 1 was assumed to correspond to the glass state.

To determine characteristic mixing times of organic molecules within SOA, diffusion coefficients of organic molecules within SOA as a function of temperature and RH, $D_{org}(RH, T)$, were calculated from $\eta(RH, T)$ using the Stokes-Einstein equation (Eq. 1.1).

A recent study showed that diffusion coefficients of organic molecules predicted with the Stokes-Einstein equation were in reasonable agreement with measured diffusion coefficients in most cases when the radius of the diffusing molecules (R_{diff}) was greater than or equal to the radius of the matrix molecules (R_{matrix}) and when the viscosity was less than or equal to 10^6 Pa s (Evoy et al., 2019). A more recent study showed that the fractional Stokes-Einstein equation was able to predict 98% of observed diffusion coefficients roughly within the uncertainty of the measurement for R_{diff}/R_{matrix} values ranging from 0.31 to 1.75 and viscosities ranging from 10^{-3} to 10^{10} Pa s. Nevertheless, here the Stokes-Einstein equation was used instead of the fractional Stokes-Einstein equation to predict diffusion coefficients of organic molecules to be consistent with Shiraiwa et al. (2017b). For these calculations, a R_{diff} value of 0.4 nm was used, which is consistent with molecular weights, densities, and an assumed spherical geometry of SOA

molecules (Bahreini et al., 2005; Cross et al., 2007; Hinks et al., 2018; Li et al., 2011; Malloy et al., 2009; Ng et al., 2007; Renbaum-Wolff et al., 2013; Saathoff et al., 2009; Smith et al., 2020; Tasoglou and Pandis, 2015). In contrast, Shiraiwa et al. (2017b) used a value of 0.1 nm for the radius of the diffusing molecules. This results in a difference of only a factor of 4 in the mixing times of organic molecules according to Eq. 1.1, which is small compared to the variability in the mixing times considered here (> 5 orders of magnitude variability). Nevertheless, when comparing these results with Shiraiwa et al. (2017b), all of the organic mixing times from Shiraiwa et al. (2017b) have been increased by a factor of 4 to be consistent with the radius of the diffusing molecule used in this study.

After determining $D_{org}(RH, T)$, characteristic mixing times of organic molecules as a function of RH and temperature, $\tau_{mix,org}(RH, T)$, were calculated using Eq. 1.2 (Seinfeld and Pandis, 2006). This mixing time corresponds to the time it takes for concentration of the diffusing species at the centre of the particle to be approximately 1/e of the equilibrium concentration (Zaveri et al., 2014). The diameter of the SOA particles was assumed to be 200 nm as that is a common size of SOA particles in the atmosphere (Martin et al., 2010; Pöschl et al., 2010; Riipinen et al., 2011).

To determine characteristic mixing times of water within SOA, diffusion coefficients of water as a function of RH and temperature were determined using the fractional Stokes-Einstein equation (Easteal, 1990):

$$D(RH, T) = D_0(T) * \left(\frac{\eta_0(T)}{\eta(RH, T)}\right)^\xi \quad (\text{Eq. 5.7})$$

where ξ is the fractional exponent, $\eta(RH, T)$ is the viscosity as a function of RH and temperature, $\eta_0(T)$ is the viscosity of pure water as a function of temperature (10^{-3} at a temperature of 293 K), and $D_0(T)$ is the diffusion coefficient in pure water as a function of temperature. The temperature-dependent viscosity data for pure water was taken from Hallett (1963) and Crittenden et al. (2012). Details can be found in Section C.2. $D_0(T)$ was evaluated using the Stokes-Einstein equation (Eq. 1.1) and assuming a radius for water of 0.1 nm (Price et al., 2016)). The value of ξ was calculated using Eq. 5.8 (Evoy et al., 2020):

$$\xi = 1 - \left[A \exp\left(-B \frac{R_{diff}}{R_{matrix}}\right) \right] \quad (\text{Eq. 5.8})$$

where A corresponds to 0.73 and B corresponds to 1.79 (Evoy et al., 2020). To evaluate Eq. 5.8, values of $R_{diff} = 0.1$ nm and $R_{matrix} = 0.4$ nm were assumed to be consistent with the size of organic molecules discussed above.

For this case, the common Stokes-Einstein equation was not used, since it drastically underpredicts diffusion coefficients of water and small oxidants in organic-water mixtures (Evoy et al., 2020). On the other hand, the fractional Stokes-Einstein equation (Eq. 5.7) combined with Eq. 5.8 is able to predict 98 % of the published diffusion coefficients of small molecules, including water, within the uncertainties of the measurements for organic-water mixtures (Evoy et al., 2020). Once diffusion coefficients of water as a function of RH and temperature were determined, characteristic mixing times of water within the SOA were calculated using Eq. 1.2. The fractional Stokes-Einstein equation was used instead of the method used by Shiraiwa et al. (2017b), because it does not require any assumption of the hygroscopicity or density of the SOA.

5.2.4 Predicting phase state and mixing times from Shiraiwa et al. (2017b)

Shiraiwa et al. (2017b) used a chemical transport model to predict the mass of biogenic and anthropogenic SOA in three separate volatility bins. Each volatility bin was then assigned molar masses and oxygen-to-carbon ratios (O:C) based on the molecular corridor approach. The glass transition temperature for each bin was then calculated from the molar mass and O:C using a parameterization developed by Shiraiwa et al. (2017b). The glass transition temperature as a function of RH of the total SOA (biogenic and anthropogenic SOA combined) was then calculated from the glass transition temperature of each volatility bin using the Gordon-Taylor approach. Viscosities and mixing times were then calculated as a function of temperature and RH from the RH-dependent glass transition temperature of the total SOA. Due to this approach, their predictions correspond to the total SOA (biogenic and anthropogenic SOA), rather than biogenic and anthropogenic SOA separately. Shiraiwa et al. (2017b) mostly focused on results at three atmospheric pressures: surface (1013 hPa), 850 hPa, and 500 hPa. Here, for comparison purposes, the predictions from Shiraiwa et al. (2017b) are replotted as a function of latitude and altitude. As mentioned above, their mixing times for organic molecules within SOA were increased by a factor of 4 to account for the systematic difference in the choice of radius for the diffusing molecules used in this Chapter.

5.2.5 RH and temperature in the troposphere

The RH and temperature in the troposphere were needed to assess the phase of the SOA and the mixing times within the particles. Average annual RH and temperature fields were calculated using the model EMAC for the years 2005-2009 (Fig. 5.4) (Jöckei et al., 2006; Shiraiwa et al., 2017b). The same RH and temperature fields were used by Shiraiwa et al. (2017b). RH and temperature were determined as function of pressure, latitude, and longitude. From the pressure, the altitude (h) was calculated using Eq. 5.9 (Filippone, 2006):

$$h = \frac{1 - \left(\frac{P(h)}{P_0}\right)^{\frac{R\lambda}{gM_{air}}}}{\frac{\lambda}{T^*}} \quad (\text{Eq. 5.9})$$

where P_0 is the pressure at sea level (101325 Pa), $P(h)$ is the pressure at the altitude h , R is the gas constant ($8.3145 \text{ J mol}^{-1} \text{ K}^{-1}$), λ is the temperature lapse rate (0.0065 K m^{-1}), g is the standard gravity (9.806 m s^{-2}), M_{air} is the molecular mass of air (28.97 g mol^{-1}), and T^* is the temperature at the surface (288.15 K). Temperature and RH values were averaged across longitude to give values as a function of latitude and altitude.

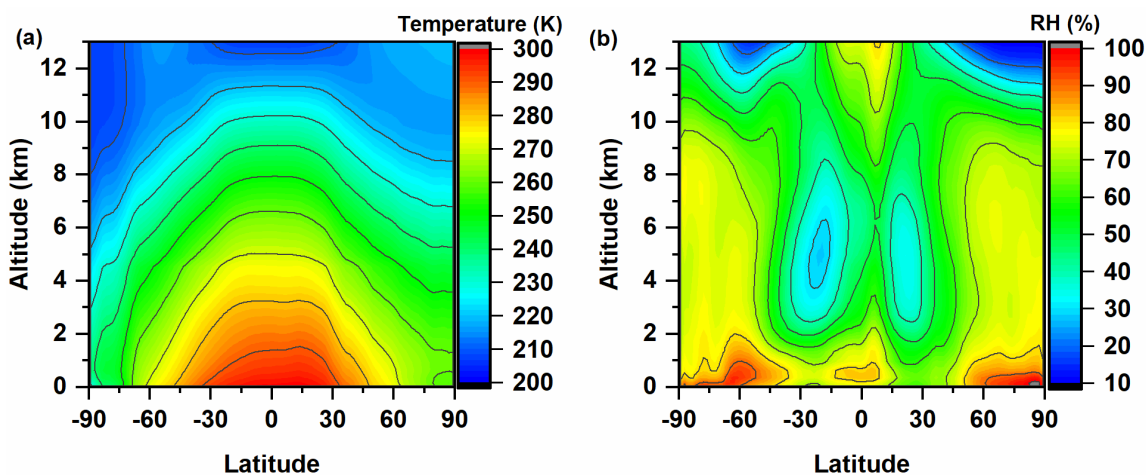


Figure 5.4: Altitude profiles for a) temperature and b) relative humidity (RH) as a function of latitude calculated using the EMAC model for the years 2005-2009.

5.3 Results and discussion

5.3.1 Parameterization of the viscosity, T_g/T , and mixing times of SOA particles as a function of temperature and RH.

Shown in Fig. 5.5a-h are the parameterizations of viscosity, T_g/T , and mixing times as a function of RH and temperature developed using the procedures described above. To highlight a few points: 1) as expected, the viscosity depends strongly on RH and temperature, with the viscosity increasing as the RH and temperature decrease (Fig. 5.5a-b). An increase in viscosity with a decrease in RH is expected since water is a plasticizer and a decrease in RH leads to a decrease in the water content of the SOA. An increase in viscosity with a decrease in temperature is expected since at lower temperatures the molecules have less energy available to overcome intermolecular forces. 2) At RH = 0, the biogenic SOA and anthropogenic SOA are in a glass state at temperatures ≤ 280 K and ≤ 285 K, respectively (Fig. 5.5 c-d). This illustrates that SOA can be in a glass state at temperatures approaching room-temperature, if RH is low. However, it should be kept in mind that a transition to a glass state is highly dependent on RH. For example, at RH = 60%, the biogenic SOA and anthropogenic SOA do not reach the glass state until the temperature is ≤ 250 K and ≤ 235 K, respectively. 3) At the same RH and temperature, the mixing times of organics are much longer than the mixing times of water within the same particle. For example, at 0% RH and 280 K, the mixing times of organics are a factor of 10^7 larger than the mixing times of water within the biogenic SOA (Fig. 5.5e & 5.4g). This is because small molecules, such as water, can more easily diffuse through SOA particles than larger organic molecules.

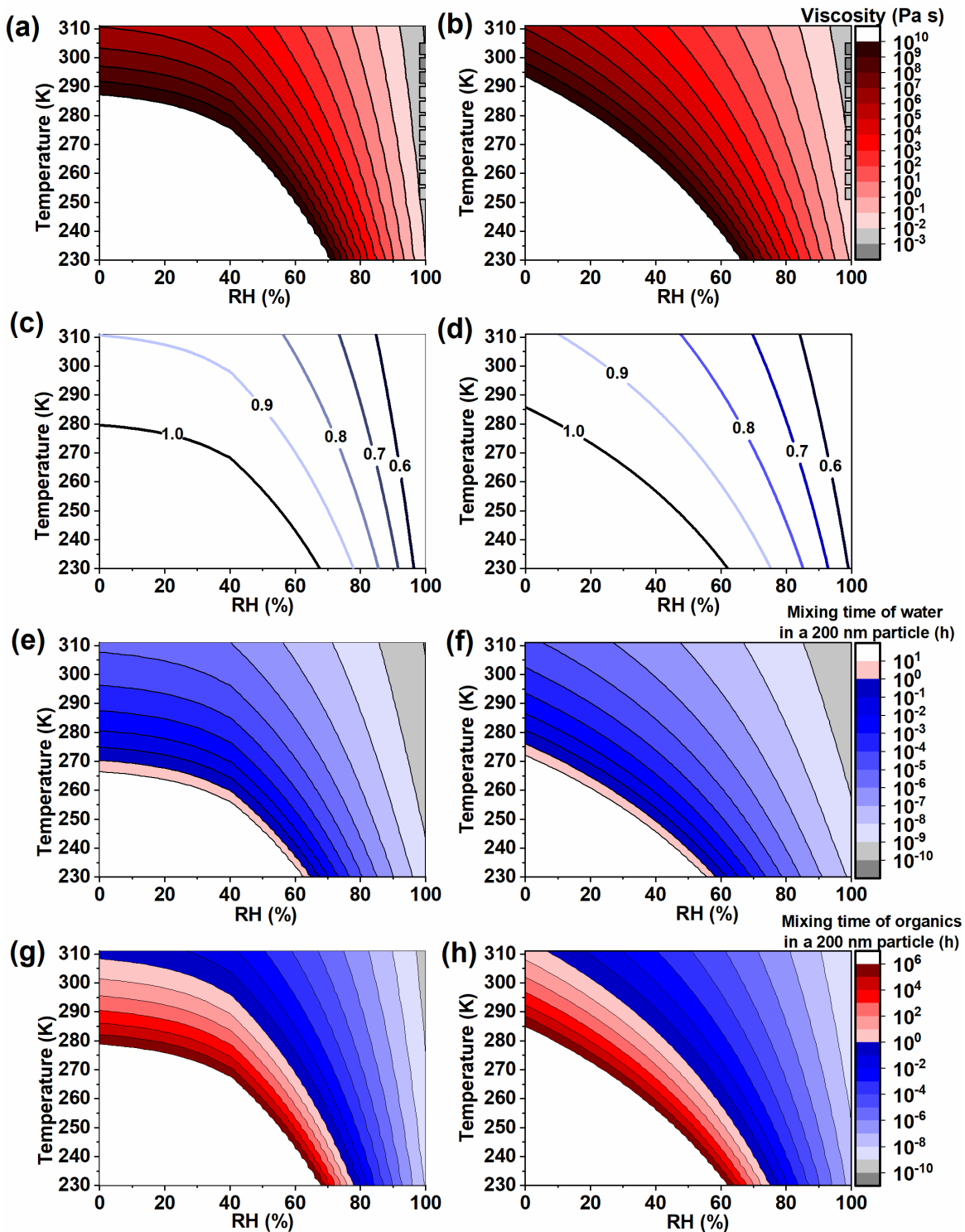


Figure 5.5: Parameterizations for viscosity (a, b), T_g/T (c, d), mixing time of water (e, f) and mixing time of organic molecules (g, h) as a function of temperature and RH for biogenic SOA (left-hand side) and anthropogenic SOA (right-hand side). The squares in panels (a, b) correspond to the viscosity of water as a function of temperature. Mixing times of water and organic molecules within SOA were calculated for 200 nm particles.

5.3.2 Global distributions of the glass state.

Shown in Fig. 5.6 are predicted annual average T_g/T values as a function of altitude and latitude for biogenic SOA (Fig. 5.6a) and anthropogenic SOA (Fig. 5.6b). As mentioned above, SOA is considered a glass when $T_g/T \geq 1$. Shown in Fig. 5.7 are annual average T_g/T values as a function of altitude for the tropical regions (-23.26° to 23.26°), midlatitude regions (-23.26° to -66.3° and 23.26° to 66.3°), and polar regions ($< -66.3^\circ$ and $> 66.3^\circ$). The patterns of T_g/T as a function of altitude and latitude are similar in the northern and southern hemisphere (Fig. 5.6), since the patterns of RH and temperature are similar in both hemispheres (Fig. 5.4). In addition, the shape of the $T_g/T = 1$ isopleth for biogenic SOA is similar to anthropogenic SOA, except the anthropogenic $T_g/T = 1$ isopleth occurs at 1-2 km higher in altitude. Based on Fig. 5.6, the lowest altitude at which the glass state is observed is 4 km for biogenic SOA and 5.25 km for anthropogenic SOA, occurring at a latitude of -30° , due in part to the low RH values at this latitude (Fig. 5.4). The glassy state is not common in the PBL, based on these predictions.

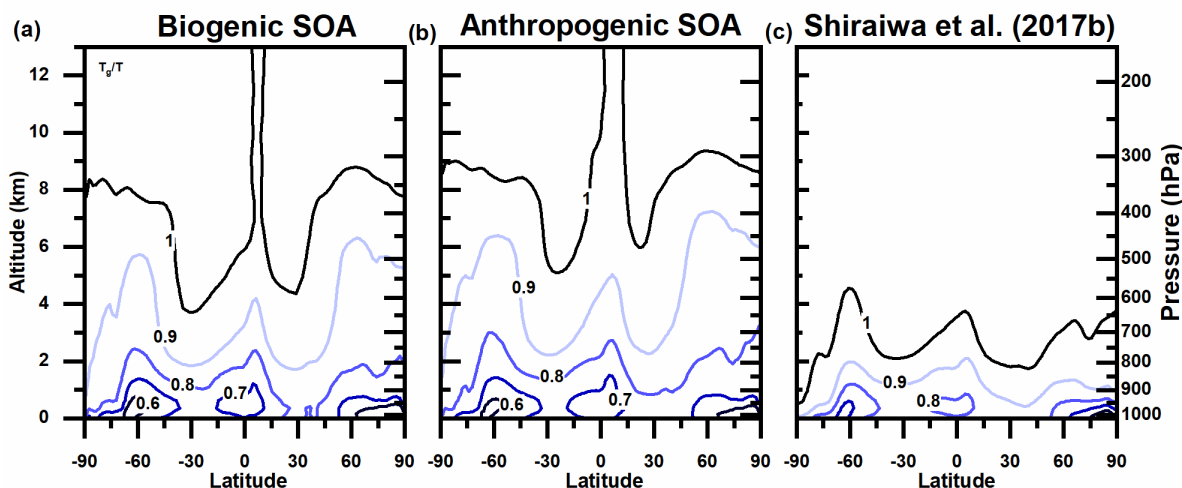


Figure 5.6: Annual average phase state of particles of a) biogenic SOA, b) anthropogenic SOA and c) SOA from Shiraiwa et al. (2017b) as a function of altitude and latitude. The particles are solid when $T_g/T > 1$.

For biogenic SOA in the polar, midlatitudes, and tropical regions, the annual average T_g/T exceeds 1, indicating the formation of a glass, at altitudes of 8 km, 7.25 km, and 5.25 km, respectively (Fig. 5.7). For anthropogenic SOA at these latitudes, the average T_g/T exceeds 1 at altitudes of 9 km, 8.25 km, and 7.25 km, respectively (Fig. 5.7). At the same altitude, the average T_g/T values in the polar regions are lower than the average T_g/T values for the midlatitude and

tropical regions (Fig. 5.7) due to the higher RH values predicted in the polar regions by the model (Fig. 5.4b).

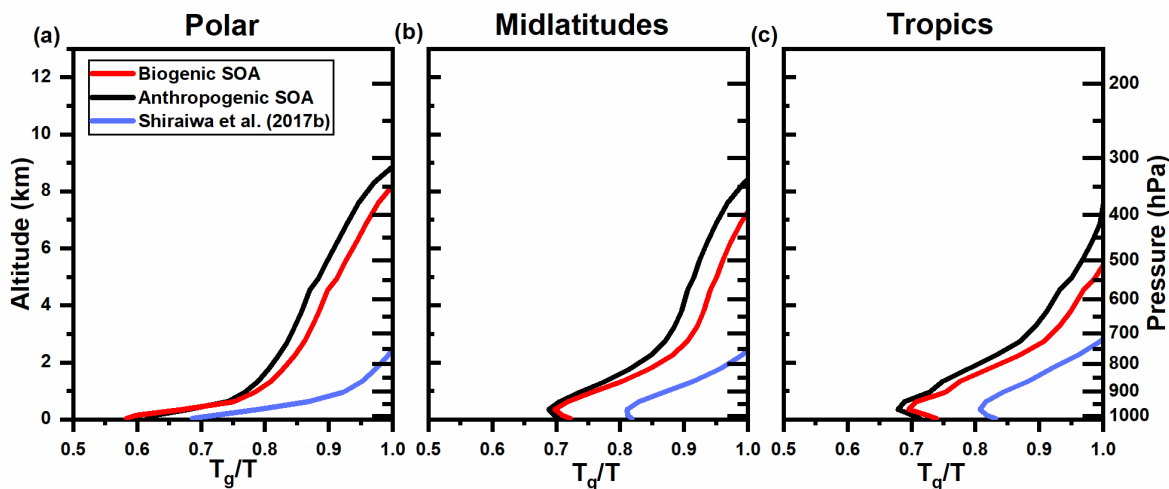


Figure 5.7: Annual average altitude profiles of T_g/T for a) polar (latitude $>66.3^\circ$ and $<-66.3^\circ$), b) midlatitude ($66.3^\circ > \text{latitude} > 23.26^\circ$ and $-66.3^\circ < \text{latitude} < -23.26^\circ$) and c) tropical ($23.26^\circ > \text{latitude} > -23.26^\circ$) regions for biogenic SOA (red), anthropogenic SOA (black) and SOA from Shiraiwa et al. (2017b) (blue).

The results from Shiraiwa et al. (2017b) are shown in Fig. 5.6c and 5.7 for comparison. As discussed above, their results correspond to the combined biogenic and anthropogenic SOA. However, biogenic sources dominate outside urban environments and in the FT since anthropogenic sources contribute only approximately 10% to the total SOA budget (Hallquist et al., 2009). The predictions from Shiraiwa et al. (2017b) have a similar shape to the results for biogenic and anthropogenic SOA (Fig. 5.6c), except the $T_g/T = 1$ is shifted to lower altitudes. The $T_g/T = 1$ isopleth from Shiraiwa et al. (2017b) is approximately 1-4 km lower in altitude than the biogenic SOA predictions, depending on latitude. At latitudes of -30° , the glass state is predicted at altitudes of 2 km by Shiraiwa et al. (2017b). For the polar, midlatitude, and tropical regions the average $T_g/T \geq 1$ at altitudes of 2.5 km, 2.5 km, and 3 km, respectively based on Shiraiwa et al. (2017b). The glassy state is also uncommon in the PBL based on the Shiraiwa et al. (2017b) predictions.

5.3.3 Global distributions of water mixing times

Shown in Fig. 5.8-5.9 are the predicted global distributions of annual average mixing times of water in 200 nm particles. The shapes of the 1 h isopleth for biogenic SOA is similar to

anthropogenic SOA 1 h isopleth except the anthropogenic 1 h isopleth occurs at 2-3 km higher in altitude. Based on Fig. 5.8, the lowest altitude where the mixing times of water ≥ 1 h is 5 km for biogenic SOA and 7 km for anthropogenic SOA, occurring at latitudes of -30° and -20° , respectively.

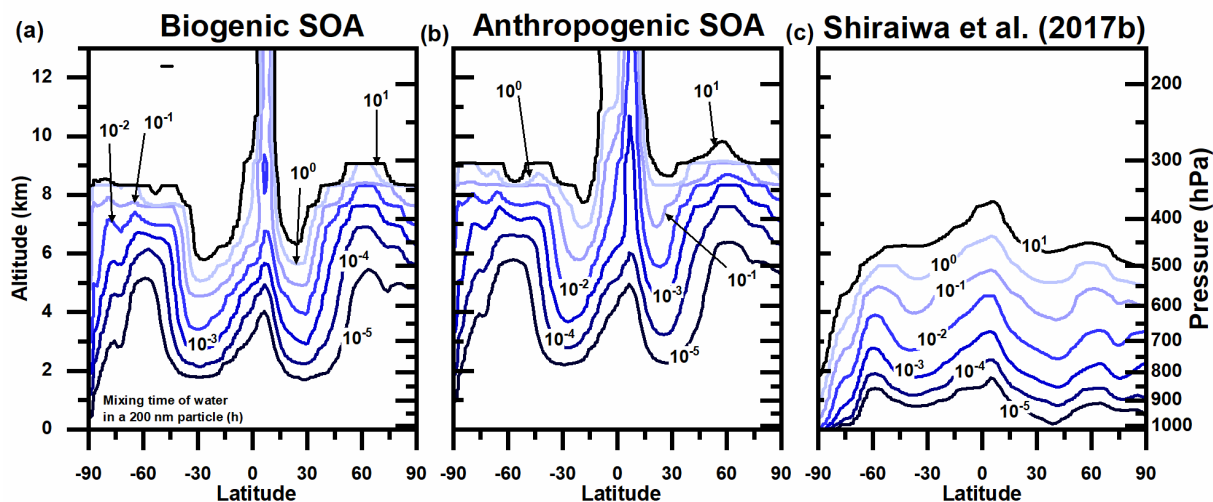


Figure 5.8: Annual average mixing time of water in a 200 nm particles for a) biogenic SOA, b) anthropogenic SOA and c) SOA for Shiraiwa et al. (2017b) as a function of altitude and latitude. The contour lines correspond to mixing times in hours.

The average mixing times of water as a function of altitude were calculated using the average of the log of the mixing time at each altitude. For biogenic SOA in the polar, midlatitude, and tropical regions, the average mixing time of water ≥ 1 h at altitudes of 8.5 km, 8 km, and 6.5 km, respectively (Fig. 5.9). For anthropogenic SOA at these latitudes, the average mixing time of water ≥ 1 h at altitudes of 9 km, 9 km, and 9.5 km, respectively (Fig. 5.9).

The results for Shiraiwa et al. (2017b) have a similar shape to the biogenic and anthropogenic SOA results (Fig. 5.8c), except that the 1 h isopleth is at lower altitudes. At a latitude of -30° (Fig. 5.8c), the mixing time of water is predicted to be > 1 h at altitudes of 5.25 km by Shiraiwa et al. (2017b). The average mixing time of water in polar, midlatitude, and tropical region is > 1 h at altitudes of 4.5 km, 5.5 km, and 6 km, respectively (Fig. 5.9).

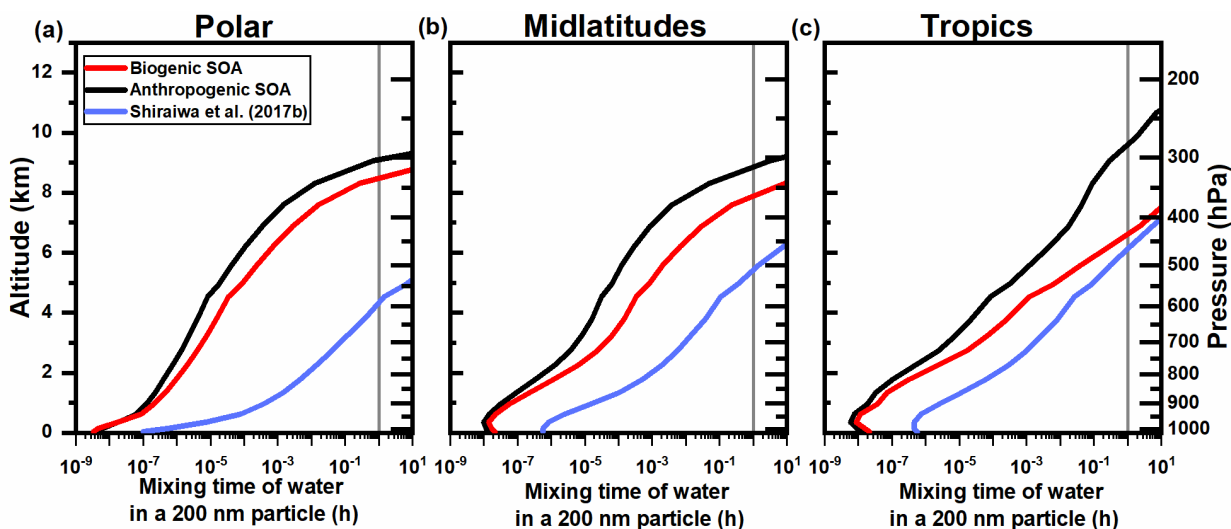


Figure 5.9: Annual average altitude profiles of the mixing time of water in a 200 nm particle for a) polar ($\text{latitude} > 66.3^\circ$ and $< -66.3^\circ$), b) midlatitude ($66.3^\circ > \text{latitude} > 23.26^\circ$ and $-66.3^\circ < \text{latitude} < -23.26^\circ$) and c) tropical ($23.26^\circ > \text{latitude} > -23.26^\circ$) regions for biogenic SOA (red), anthropogenic SOA (black) and SOA from Shiraiwa et al. (2017b) (blue). The vertical lines are included to highlight a mixing time of 1 h. Average mixing time values were calculated using the average of the log mixing time data as a function of latitude.

5.3.4 Global distributions of organic mixing times

Shown in Fig. 5.10-5.11 are the predicted global distributions of annual average mixing times of organic molecules in 200 nm particles. The lowest altitude at which the mixing times of organics exceeds 1 h is 2 km for biogenic SOA (Fig. 5.10a) and 2.25 km for anthropogenic SOA (Fig. 5.10b), corresponding to -30° latitude. The mixing times of organics is < 1 h in the planetary boundary layer (PBL) based on both the biogenic and anthropogenic SOA predictions.

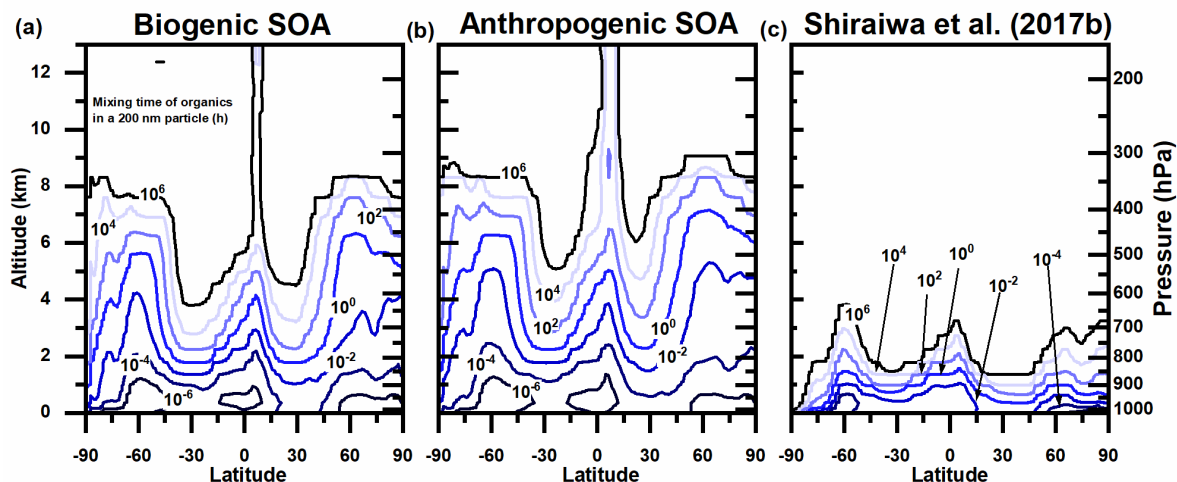


Figure 5.10: Annual average mixing time of organic molecules within SOA for a) biogenic SOA, b) anthropogenic SOA and c) SOA from Shiraiwa et al. (2017b) as a function of altitude and latitude. The contour lines correspond to mixing times in hours.

The average mixing times of organic molecules as a function of altitude were calculated using the average of the log of the mixing time at each altitude. Biogenic SOA in the polar, midlatitude, and tropical regions reaches an average mixing time of organics ≥ 1 h at altitudes of 4.5 km, 2.5 km, and 2.5 km, respectively (Fig. 5.11). Anthropogenic SOA at these latitudes reaches an average organic mixing time ≥ 1 h at altitudes of 6 km, 4 km, and 3 km, respectively (Fig. 5.11).

Similarly to T_g/T and the water mixing times, the results for the mixing time of organics by Shiraiwa et al. (2017b) have a similar shape to the biogenic and anthropogenic results (Fig. 5.10c), except the 1 h isopleth occurs at a lower altitude. At a latitude of -30° (Fig. 5.10c), the mixing time of organics exceeds 1 h at ~ 0.75 km. The average mixing times of organics in the polar, midlatitude and tropical regions are ≥ 1 h at altitudes 0.5 km, 1 km, and 1 km, respectively (Fig. 5.11). The mixing times of organics is < 1 h in the PBL for most of times based on the Shiraiwa et al. (2017b) predictions.

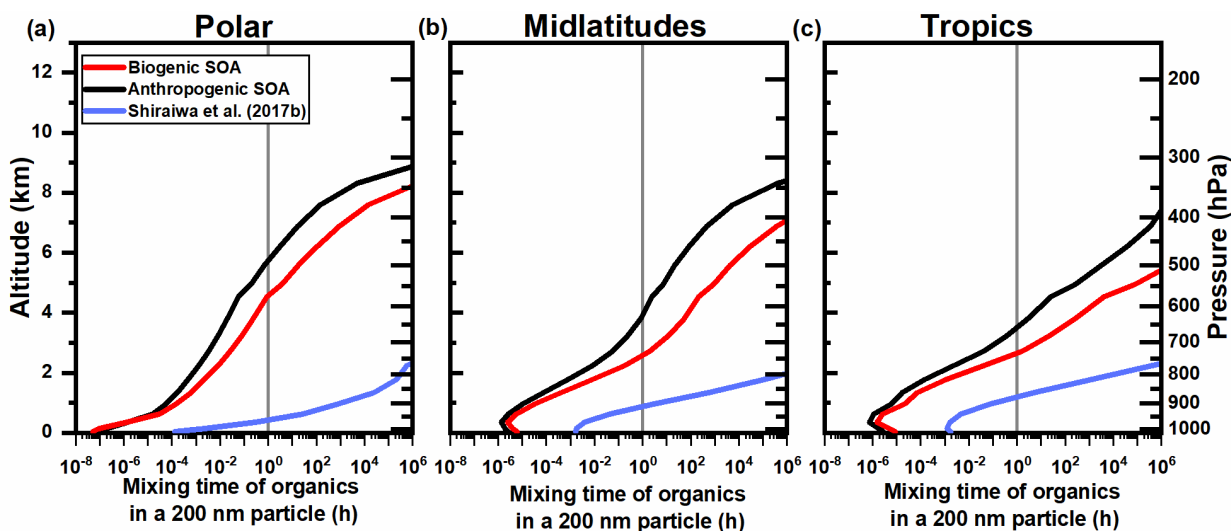


Figure 5.11: Annual average altitude profiles of the mixing time of organics in a 200 nm particle for a) polar (latitude $>66.3^\circ$ and $<-66.3^\circ$), b) midlatitude ($66.3^\circ > \text{latitude} > 23.26^\circ$ and $-66.3^\circ < \text{latitude} < -23.26^\circ$) and c) tropical ($23.26^\circ > \text{latitude} > -23.26^\circ$) regions for biogenic SOA (red), anthropogenic SOA (black), and SOA from Shiraiwa et al. (2017b) (blue). The vertical lines are included to highlight a mixing time of 1 h. Average mixing time values were calculated using the average of the log mixing time data as a function of latitude.

5.3.5 Possible reasons for the difference between the current results and Shiraiwa et al. (2017b)

The T_g/T values, mixing times of water, and mixing times of organics predicted by Shiraiwa et al. (2017b) are larger than predicted here for the same altitude and latitude. These differences can be due to several reasons. For example, the method used to predict viscosities by Shiraiwa et al. (2017b) is very different than used here (see Section 5.2.4, for details). Several parameters were needed for the predictions by Shiraiwa et al. (2017b) including the hygroscopicity and Gordon-Taylor constants for the SOA. These parameters each have their own uncertainties, which could lead to an under- or over-prediction of the viscosity of the SOA. In addition, the parameterization used by Shiraiwa et al. (2017b) to convert molar mass and O:C to a glass transition temperature had an uncertainty of ± 15 K for individual components, which can also lead to an under- or over-prediction of the viscosity of the SOA, although the uncertainty may be as small as ± 3 K for SOA mixtures.

In this chapter, viscosity measurements of SOA generated in an environmental chamber were used. In this case, the SOA was formed during a short time period (less than 2 h), and hence corresponds to fresh SOA. In contrast the simulations by Shiraiwa et al. (2017b), which

incorporated a chemical transport model and atmospheric chemistry, included chemical aging of SOA that can occur over longer time periods in the atmosphere. This atmospheric aging can lead to reduced volatilities and higher viscosities, T_g/T values, and mixing times (Athanasiadis et al., 2016; Champion et al., 2019; Hosny et al., 2016; Li et al., 2020; Saukko et al., 2012b; Schum et al., 2018; Zhang et al., 2019b). In addition, the SOA used to generate the biogenic parameterization discussed here was produced with a mass concentration of $\sim 150 \mu\text{g m}^{-3}$ (Smith et al., 2020), which is higher than found in the FT. Previous studies have shown that higher mass concentrations can lead to lower viscosities, and hence lower T_g/T values and mixing times (Champion et al., 2019; Grayson et al., 2016; Jain et al., 2018). In contrast, Shiraiwa et al. (2017b), used a chemical transport model to predict mass concentrations, which is able to reproduce spatial distributions and mass concentrations of SOA measured in the troposphere (Tsimpidi et al., 2016). The SOA used to generate the anthropogenic parameterization was produced with mass concentrations of either $60\text{-}100 \mu\text{g m}^{-3}$ or $600\text{-}1000 \mu\text{g m}^{-3}$, with no dependence of the viscosity on production mass concentration (Song et al., 2016a). As a result, it is unknown whether the viscosity would increase at lower mass concentrations. In conclusion, the differences between the current studies and the studies by Shiraiwa et al. (2017b) may be explained by the higher mass concentrations and lack of chemical aging of the SOA used to develop the parameterization in this Chapter. However, differences in methodologies used to predict viscosity may also play a role.

5.4 Summary and conclusions

Parameterizations for viscosity as a function of temperature and RH were developed for biogenic and anthropogenic SOA based on room temperature viscosity data. Based on these parameterizations, as well as tropospheric RH and temperature fields, the phase state and mixing times of water and organic molecules in SOA particles were predicted. Some of the key results are summarized and compared with Shiraiwa et al. (2017b) in Table 5.1. Based on the results, the glass state can be important, and the mixing time of water can exceed 1 h in the middle and upper FT. The mixing time of organic molecules can exceed 1 h throughout most of the FT. The glass state is not important in the PBL and mixing of water and organic molecules is < 1 h for most of the PBL. This latter conclusion is consistent with previous predictions, field measurements, and laboratory studies of SOA at temperatures and RH values common for the

PBL (Bateman et al., 2016, 2017; Ditto et al., 2019; Liu et al., 2016; Maclean et al., 2017; Pajunoja et al., 2016; Ye et al., 2016).

Table 5.1: Altitudes at which SOA reaches a glassy state, and altitude at which the mixing time of water and organics in SOA exceed 1 h

SOA Property	Source of SOA	Region of the Earth			
		-30° latitude	Tropical	Midlatitudes	Polar
$T_g/T > 1$	Biogenic SOA (Chapter 5)	4 km	5.25 km	7.25 km	8 km
	Shiraiwa et al. (2017b) (Mostly Biogenic SOA)	2 km	3 km	2.5 km	2.5 km
	Anthropogenic SOA (Chapter 5)	5.25 km	7.25 km	8.25 km	9 km
Mixing time of water > 1 h in 200 nm SOA	Biogenic SOA (Chapter 5)	5 km	6.5 km	8 km	8.5 km
	Shiraiwa et al. (2017b) (Mostly Biogenic SOA)	5.25 km	6 km	5.5 km	4.5 km
	Anthropogenic SOA (Chapter 5)	8 km	9.5 km	9 km	9 km
Mixing time of organics > 1 h in 200 nm SOA	Biogenic SOA (Chapter 5)	2 km	2.5 km	2.5 km	4.5 km
	Shiraiwa et al. (2017b) (Mostly Biogenic SOA)	0.75 km	1 km	1 km	0.5 km
	Anthropogenic SOA (Chapter 5)	2.25 km	3.5 km	4 km	5.75 km

The results from Shiraiwa et al. (2017b) are qualitatively consistent with these findings. Their results suggest that the glass state can be important and mixing times of organics can exceed 1 h throughout most of the FT, while the importance of slow mixing of water may be

constrained to the middle and upper FT. They also predict that the glass state is not important and mixing of water and organics is < 1 h in the PBL, except perhaps in the south polar region.

Based on these combined results, SOA particles in the upper FT will most often be in a glass state with long mixing times of water. The timescale of a typical updraft in the atmosphere is 1 s to 1 h (Berkemeier et al., 2014). During an updraft the temperature will decrease, and the RH will increase. Due to the long mixing times of water in the SOA in this region of the atmosphere, SOA may not be able to reach equilibrium with the surrounding RH during updrafts. As a result, heterogenous ice nucleation by the glass state will be more likely since a glassy core will more likely be able to persist during the updraft (Berkemeier et al., 2014).

Based on the combined results, the mixing times of organic molecules can be long throughout most of the FT. Long mixing times of organics in the FT have implications for the long-range transport of pollutants such as polycyclic aromatic hydrocarbons (PAHs). Previous studies have shown that aerosol particles can undergo long-range transport at altitudes of 2-6 km, depending on the region (Carlson, 1981; Weinzierl et al., 2017; Zhao et al., 2013). At these altitudes, the mixing times of organics within SOA can be long. As a result, pollutant molecules can be trapped within the SOA particles, inhibiting their degradation via oxidation (Zelenyuk et al., 2012; Zhou et al., 2013).

The mixing time of organics in SOA is predicted to be < 1 h for most, if not all, the PBL, where the majority of SOA is formed. This means that the assumption of equilibrium partitioning for SOA formation used in chemical transport models is reasonable for the PBL, consistent with previous conclusions (Friedman et al., 2014; Liu et al., 2016; Maclean et al., 2017; Mu et al., 2018; Shiraiwa et al., 2017b; Shrivastava et al., 2017; Ye et al., 2016). Equilibrium partitioning for SOA may not be valid in cases where SOA is formed in the FT (Heald et al., 2006).

Chapter 6: Conclusions and future work

6.1 Conclusions

6.1.1 Predicting mixing times of organic molecules in SOA in the troposphere

Chapters 3 and 5 presented predictions of mixing times of organic molecules in SOA and SOA proxies in the troposphere to test the assumption of rapid mixing within SOA. Chapter 3 focused on mixing times in α -pinene SOA and sucrose particles in the PBL while Chapter 5 focused on mixing times in SOA from tree emissions and toluene SOA in the whole troposphere. Chapter 5 also shows a comparison of mixing times with another study. These results added to the limited studies investigating global distributions of mixing times of organic molecules in SOA in the atmosphere.

In Chapter 3, parameterizations of viscosity were developed for α -pinene SOA and sucrose particles based on room-temperature and low temperature viscosity values. The parameterizations were then used with RH and temperature fields in the PBL and the Stokes-Einstein equation to predict the mixing times of organic molecules within the SOA. The results showed that the mixing times of organic molecules are generally < 1 h in the PBL. For α -pinene SOA, the mixing times of organic molecules are < 1 h for $> 98\%$ of the RH and temperature conditions for both January and July. For sucrose particles, a proxy for anthropogenic SOA, the mixing times are < 1 h for $> 70\%$ of the RH and temperature conditions for January and July. Overall, it is expected that mixing times of organic molecules in SOA will generally be < 1 h in the PBL and the assumption of rapid mixing is valid in this region of the atmosphere.

In Chapter 5, parameterizations of viscosity were developed for tree emission SOA and toluene SOA based on room-temperature viscosity values. These parameterizations were combined with RH and temperature fields in the troposphere and the Stokes-Einstein equation to predict the mixing times of organics in the troposphere. Both types of SOA were found to have mixing times of organic molecules < 1 h in the PBL, similar to the results in Chapter 3. However, both the tree emission SOA and toluene SOA had predicted mixing times > 1 h in the middle and upper FT, indicating that the assumption of rapid mixing may not be valid for the entire troposphere. These results agreed with another modeling study by Shiraiwa et al. (2017b) which also predicted that the mixing times of organic molecules would be > 1 h in the majority of the FT. As a result, the long mixing time of organic molecules is expected to be important for predicting SOA growth, lifetime, and the long-range transport of pollutants in the FT.

6.1.2 Room-temperature mixing times of organic molecules in SOA based on measured viscosities as a function of RH

Chapter 4 presented room-temperature viscosity measurements as a function of RH for SOA generated from the ozonolysis of β -caryophyllene, a sesquiterpene. The viscosity of the SOA increased by 2-3 orders of magnitude as the RH decreased from 48% to 0%. The viscosities were converted into diffusion coefficients using the fractional Stokes-Einstein equation which were then used to calculate mixing times of organics within the SOA. The mixing times varied from < 6 s at 48% up to 0.4 h at 0% RH. It is expected that mixing times of organics will be < 1 h for RH and temperature conditions typically found in the PBL. The viscosity of the SOA was also predicted based on chemical composition using the parameterization from DeRieux et al. (2018). Using the adjusted mass approach from Nguyen et al. (2013) to account for the sensitivity of the electrospray ionization to larger molecular weight components, the upper limit of measured viscosity overlapped with the lower limit of the predictions. As well, the predictions using a mole-fraction based mixing rule overlapped with the measured data however both the predictions based on chemical composition and predictions using a mole-fraction based mixing rule had large uncertainties associated with the hygroscopicity of the SOA. Further measurements of the hygroscopicity of β -caryophyllene SOA are required to gain a better understanding of this parameter and reduce the uncertainty.

6.1.3 Phase state and mixing time of water in SOA in the troposphere

Chapter 5 presented predictions of SOA phase state and the mixing time of water for biogenic and anthropogenic SOA in the troposphere. For both biogenic and anthropogenic SOA, SOA particles are expected to be in a glass state in the upper FT at most latitudes, with mixing times of water > 1 h. As a result, heterogenous ice nucleation by the glass state will be more likely as a glassy core is more likely to persist during an updraft. These results are consistent with the modelling study by Shiraiwa et al. (2017b). They found that SOA particles are likely to be in a glass state in much of the FT, with mixing times of water > 1 h in the middle and upper FT. As a result, heterogenous ice nucleation by glassy SOA needs to be considered in models to accurately predict the impact of SOA.

6.2 Future work

Predictions of phase state and the mixing times of water and organic molecules based on viscosity measurements were presented here. Many of these studies focused on SOA generated from a single VOC (α -pinene, β -caryophyllene and toluene) with only Chapter 5 using SOA generated from a mixture of VOCs (tree emission SOA). Since atmospheric SOA is comprised of products from the oxidation of multiple different VOCs, studies measuring or inferring phase state and mixing times in laboratory SOA generated from a variety of VOCs more representative of atmospheric SOA are critical for predicting these properties in the atmosphere.

Studies measuring the diffusion coefficients of water in SOA are also needed. Current studies have measured the diffusion of water in SOA proxies with very few measurements in SOA. Measurements in glassy mixtures at the same temperature have shown that the diffusion coefficient of water can vary between different substances and isn't necessarily correlated with the glass transition temperature. As a result, additional studies are needed to measure the diffusion coefficients of water in glassy SOA as a function of temperature and RH to gain a better understanding of water diffusion in the atmosphere.

The SOA used for Chapters 3, 4 and 5 were all generated at higher mass concentrations than would typically be found in the atmosphere. Previous results have shown that viscosity increases with decreasing mass concentration (Champion et al., 2019; Grayson et al., 2016; Jain et al., 2018), with implications for phase state and mixing times. Studies focusing on SOA generated at low, atmospherically relevant, mass concentrations are needed to properly understand the properties of atmospheric SOA. As well, measurements in more oxidized SOA are needed to better replicate atmospheric SOA.

Temperatures in the atmosphere cover a wide range, with temperatures in the FT as low as 217 K (Seinfeld and Pandis, 2006). Viscosity increases strongly with decreasing temperature, resulting in longer mixing times. It has been assumed that the temperature-dependent viscosity can be predicted using the VFT equation or equivalent equations, allowing for extrapolation of mixing times to lower temperatures. However, studies assessing the temperature dependence of mixing times, either via temperature dependent viscosity or diffusion measurements are needed to validate this assumption. This will allow for more accurate predictions of the physical parameters of SOA over a wider range of temperatures.

In Chapter 4, viscosity of SOA was predicted using a parameterization for the glass transition temperature of the organic molecules within the SOA. To further refine these predictions, more extensive datasets of the glass transition temperature of individual SOA molecules are required to improve the parameterizations. In addition, measurements of glass transition temperatures of SOA are needed to validate the predictions.

Finally, when predicting physical parameters of SOA like viscosity and mixing times, values for other parameters including hygroscopicity are needed. As shown in Chapter 4, hygroscopicity can have a significant impact on predictions of viscosity. However, there is a large uncertainty associated with hygroscopicity. As a result, studies assessing properties such as hygroscopicity are critical in combination with viscosity and mixing time measurements to ensure accurate predictions.

References

- Aalto, P.: Hyytiälä SMEAR II meteorology, gases and soil- Air temperature 8.4 m- 2012, atm-data@helsinki.fi, Etsin Res. data finder [online] Available from: <http://urn.fi/urn:nbn:fi:csc-kata20160308104539432017> (Accessed 28 June 2016a), 2012.
- Aalto, P.: Hyytiälä SMEAR II meteorology, gases and soil- Relative humidity 16 m-2012, atm-data@helsinki.fi, Etsin Res. data finder [online] Available from: <http://urn.fi/urn:nbn:fi:csc-kata20160308112058571248> (Accessed 28 June 2016b), 2012.
- Abramson, E., Imre, D., Beranek, J., Wilson, J. and Zelenyuk, A.: Experimental determination of chemical diffusion within secondary organic aerosol particles, *Phys. Chem. Chem. Phys.*, 15(8), 2983–2991, doi:10.1039/C2CP44013J, 2013.
- Aiken, A. C., DeCarlo, P. F., Kroll, J. H., Worsnop, D. R., Huffman, J. A., Docherty, K. S., Ulbrich, I. M., Mohr, C., Kimmel, J. R., Sueper, D., Sun, Y., Zhang, Q., Trimborn, A., Northway, M., Ziemann, P. J., Canagaratna, M. R., Onasch, T. B., Alfarra, M. R., Prevot, A. S. H., Dommen, J., Duplissy, J., Metzger, A., Baltensperger, U. and Jimenez, J. L.: O/C and OM/OC Ratios of Primary, Secondary, and Ambient Organic Aerosols with High-Resolution Time-of-Flight Aerosol Mass Spectrometry, *Environ. Sci. Technol.*, 42(12), 4478–4485, doi:10.1021/es703009q, 2008.
- Alfarra, M. R., Paulsen, D., Gysel, M., Garforth, A. A., Dommen, J., Prévôt, A. S. H., Worsnop, D. R., Baltensperger, U. and Coe, H.: A mass spectrometric study of secondary organic aerosols formed from the photooxidation of anthropogenic and biogenic precursors in a reaction chamber, *Atmos. Chem. Phys.*, 6(12), 5279–5293, doi:10.5194/acp-6-5279-2006, 2006.
- Angell, C. A.: Relaxation in liquids, polymers and plastic crystals - strong/fragile patterns and problems, *J. Non. Cryst. Solids*, 133, 13–31, 1991.
- Angell, C. A.: Formation of glasses from liquids and biopolymers, *Science* (80-.), 267(5206), 1924–1935, doi:10.1126/science.267.5206.1924, 1995.
- Angell, C. A.: Entropy and fragility in supercooling liquids, *J. Res. Natl. Inst. Stand. Technol.*, 102(2), 171–181, doi:10.6028/jres.102.013, 1997.
- Angell, C. A.: Liquid fragility and the glass transition in water and aqueous solutions, *Chem. Rev.*, 102(8), 2627–2650, doi:10.1021/cr000689q, 2002.
- Asa-Awuku, A., Engelhart, G. J., Lee, B. H., Pandis, S. N. and Nenes, A.: Relating CCN activity, volatility, and droplet growth kinetics of β -caryophyllene secondary organic aerosol, *Atmos. Chem. Phys.*, 9(3), 795–812, doi:10.5194/acp-9-795-2009, 2009.
- Athanasiadis, A., Fitzgerald, C., Davidson, N. M., Giorio, C., Botchway, S. W., Ward, A. D., Kalberer, M., Pope, F. D. and Kuimova, M. K.: Dynamic viscosity mapping of the oxidation of squalene aerosol particles, *Phys. Chem. Chem. Phys.*, 18(44), 30385–30393, doi:10.1039/c6cp05674a, 2016.
- Bahreini, R., Keywood, M. D., Ng, N. L., Varutbangkul, V., Gao, S., Flagan, R. C., Seinfeld, J. H., Worsnop, D. R. and Jimenez, J. L.: Measurements of secondary organic aerosol from oxidation of cycloalkenes, terpenes, and m-xylene using an aerodyne aerosol mass spectrometer, *Environ. Sci. Technol.*, 39(15), 5674–5688, doi:10.1021/es048061a, 2005.
- Bastelberger, S., Krieger, U. K., Luo, B. and Peter, T.: Diffusivity measurements of volatile organics in levitated viscous aerosol particles, *Atmos. Chem. Phys.*, 17(13), 8453–8471, doi:10.5194/acp-17-8453-2017, 2017.
- Bateman, A. P., Bertram, A. K. and Martin, S. T.: Hygroscopic Influence on the Semisolid-to-

- Liquid Transition of Secondary Organic Materials, *J. Phys. Chem. A*, 119(19), 4386–4395, doi:10.1021/jp508521c, 2015.
- Bateman, A. P., Gong, Z., Liu, P., Sato, B., Cirino, G., Zhang, Y., Artaxo, P., Bertram, A. K., Manzi, A. O., Rizzo, L. V., Souza, R. A. F., Zaveri, R. A. and Martin, S. T.: Sub-micrometre particulate matter is primarily in liquid form over Amazon rainforest, *Nat. Geosci.*, 9(1), 34–39, doi:10.1038/ngeo2599, 2016.
- Bateman, A. P., Gong, Z., Harder, T. H., De Sá, S. S., Wang, B., Castillo, P., China, S., Liu, Y., O'Brien, R. E., Palm, B. B., Shiu, H. W., Cirino, G. G., Thalman, R., Adachi, K., Elizabeth Alexander, M., Artaxo, P., Bertram, A. K., Buseck, P. R., Gilles, M. K., Jimenez, J. L., Laskin, A., Manzi, A. O., Sedlacek, A., Souza, R. A. F., Wang, J., Zaveri, R. and Martin, S. T.: Anthropogenic influences on the physical state of submicron particulate matter over a tropical forest, *Atmos. Chem. Phys.*, 17(3), 1759–1773, doi:10.5194/acp-17-1759-2017, 2017.
- Baudry, J., Charlaix, E., Tonck, A. and Mazuyer, D.: Experimental evidence for a large slip effect at a nonwetting fluid-solid interface, *Langmuir*, 17(17), 5232–5236, doi:10.1021/la0009994, 2001.
- Bauer, S. E., Tsigaridis, K. and Miller, R.: Significant atmospheric aerosol pollution caused by world food cultivation, *Geophys. Res. Lett.*, 43(10), 5394–5400, doi:10.1002/2016GL068354, 2016.
- Baustian, K. J., Wise, M. E., Jensen, E. J., Schill, G. P., Freedman, M. A. and Tolbert, M. A.: State transformations and ice nucleation in amorphous (semi-)solid organic aerosol, *Atmos. Chem. Phys.*, 13(11), 5615–5628, doi:10.5194/acp-13-5615-2013, 2013.
- Baxley, J. S. and Wells, J. R.: The hydroxyl radical reaction rate constant and Atmospheric Transformation Products of 2-Butanol and 2-Pentanol, *Int. J. Chem. Kinet.*, 36(10), 534–544, doi:10.1002/kin.20027, 1998.
- Berkemeier, T., Shiraiwa, M., Pöschl, U. and Koop, T.: Competition between water uptake and ice nucleation by glassy organic aerosol particles, *Atmos. Chem. Phys.*, 14(22), 12513–12531, doi:10.5194/acp-14-12513-2014, 2014.
- Bones, D. L., Reid, J. P., Lienhard, D. M. and Krieger, U. K.: Comparing the mechanism of water condensation and evaporation in glassy aerosol, *Proc. Natl. Acad. Sci. U. S. A.*, 109(29), 11613–11618, doi:10.1073/pnas.1200691109, 2012.
- Boratyński, A.: *Genetics of Scots Pine*, edited by M. Giertych and C. Mátyás, Elsevier, Budapest., 1991.
- Bouvier-Brown, N. C., Goldstein, A. H., Gilman, J. B., Kuster, W. C. and de Gouw, J. A.: In-situ ambient quantification of monoterpenes, sesquiterpenes and related oxygenated compounds during BEARPEX 2007: Implications for gas- and particle-phase chemistry, *Atmos. Chem. Phys.*, 9(15), 5505–5518, doi:10.5194/acp-9-5505-2009, 2009.
- Buchholz, A., Lambe, A. T., Ylisirniö, A., Li, Z., Tikkanen, O. P., Faiola, C., Kari, E., Hao, L., Luoma, O., Huang, W., Mohr, C., Worsnop, D. R., Nizkorodov, S. A., Yli-Juuti, T., Schobesberger, S. and Virtanen, A.: Insights into the O: C-dependent mechanisms controlling the evaporation of α -pinene secondary organic aerosol particles, *Atmos. Chem. Phys.*, 19(6), 4061–4073, doi:10.5194/acp-19-4061-2019, 2019.
- Cappa, C. D. and Wilson, K. R.: Evolution of organic aerosol mass spectra upon heating: implications for OA phase and partitioning behavior, *Atmos. Chem. Phys.*, 11(5), 1895–1911, doi:10.5194/acp-11-1895-2011, 2011.
- Carlson, T. N.: Speculations on the movement of polluted air to the Arctic, *Atmos. Environ.*,

- 15(8), 1473–1477, doi:10.1016/0004-6981(81)90354-1, 1981.
- Centeno, G., Sánchez-Reyna, G., Ancheyta, J., Muñoz, J. A. D. and Cardona, N.: Testing various mixing rules for calculation of viscosity of petroleum blends, *Fuel*, 90(12), 3561–3570, doi:10.1016/j.fuel.2011.02.028, 2011.
- Champion, W. M., Rothfuss, N. E., Petters, M. D. and Grieshop, A. P.: Volatility and Viscosity Are Correlated in Terpene Secondary Organic Aerosol Formed in a Flow Reactor, *Environ. Sci. Technol. Lett.*, 6(9), 513–519, doi:10.1021/acs.estlett.9b00412, 2019.
- Chen, X. and Hopke, P. K.: Secondary organic aerosol from α -pinene ozonolysis in dynamic chamber system, *Indoor Air*, 19(4), 335–345, doi:10.1111/j.1600-0668.2009.00596.x, 2009.
- Cheng, J. T. and Giordano, N.: Fluid flow through nanometer-scale channels, *Phys. Rev. E - Stat. Physics, Plasmas, Fluids, Relat. Interdiscip. Top.*, 65(3), 1–5, doi:10.1103/PhysRevE.65.031206, 2002.
- Chenyakin, Y., Ullmann, D. A., Evoy, E., Renbaum-Wolff, L., Kamal, S. and Bertram, A. K.: Diffusion coefficients of organic molecules in sucrose-water solutions and comparison with Stokes-Einstein predictions, *Atmos. Chem. Phys.*, 17(3), 2423–2435, doi:10.5194/acp-2016-740, 2017.
- Choi, C. H. and Kim, C. J.: Large slip of aqueous liquid flow over a nanoengineered superhydrophobic surface, *Phys. Rev. Lett.*, 96(6), 1–4, doi:10.1103/PhysRevLett.96.066001, 2006.
- Churaev, N. V., Sobolev, V. D. and Somov, A. N.: Slippage of liquids over lyophobic solid surfaces, *J. Colloid Interface Sci.*, 97(2), 574–581, doi:10.1016/0021-9797(84)90330-8, 1984.
- Corti, H. R., Frank, G. A. and Marconi, M. C.: An Alternate Solution of Fluorescence Recovery Kinetics after Spot-Bleaching for Measuring Diffusion Coefficients. 2. Diffusion of Fluorescein in Aqueous Sucrose Solutions, *J. Solution Chem.*, 37(11), 1593–1608, doi:10.1007/s10953-008-9329-4, 2008.
- Craig, V. S. J., Neto, C. and Williams, D. R. M.: Shear-Dependent boundary slip in an aqueous newtonian liquid, *Phys. Rev. Lett.*, 87(5), 54504-1-54504-4, doi:10.1103/PhysRevLett.87.054504, 2001.
- Crittenden, J. C., Trussel, R. R., Hand, D. W., Howe, K. J. and Tchobanoglous, G.: *MWH's Water Treatment*, John Wiley and Sons., 2012.
- Cross, E. S., Slowik, J. G., Davidovits, P., Allan, J. D., Worsnop, D. R., Jayne, J. T., Lewis, D. K., Canagaratna, M. and Onasch, T. B.: Laboratory and ambient particle density determinations using light scattering in conjunction with aerosol mass spectrometry, *Aerosol Sci. Technol.*, 41(4), 343–359, doi:10.1080/02786820701199736, 2007.
- DeRieux, W.-S. W., Li, Y., Lin, P., Laskin, J., Laskin, A., Bertram, A. K., Nizkorodov, S. A. and Shiraiwa, M.: Predicting the glass transition temperature and viscosity of secondary organic material using molecular composition, *Atmos. Chem. Phys.*, 18(9), 6331–6351, doi:10.5194/acp-18-6331-2018, 2018.
- Dette, H. P., Qi, M., Schröder, D. C., Godt, A. and Koop, T.: Glass-forming properties of 3-methylbutane-1,2,3-tricarboxylic acid and its mixtures with water and pinonic acid, *J. Phys. Chem. A*, 118(34), 7024–7033, doi:10.1021/jp505910w, 2014.
- Ditto, J. C., Joo, T., Khare, P., Sheu, R., Takeuchi, M., Chen, Y., Xu, W., Bui, A. A. T., Sun, Y., Ng, N. L. and Gentner, D. R.: Effects of Molecular-Level Compositional Variability in Organic Aerosol on Phase State and Thermodynamic Mixing Behavior, *Environ. Sci. Technol.*, doi:10.1021/acs.est.9b02664, 2019.

- Donahue, N. M., Robinson, A. L. and Pandis, S. N.: Atmospheric organic particulate matter: From smoke to secondary organic aerosol, *Atmos. Environ.*, 43(1), 94–106, doi:10.1016/j.atmosenv.2008.09.055, 2009.
- Easteal, A. J.: Tracer diffusion in aqueous sucrose and urea solutions, *Can. J. Chem.*, 68(9), 1611–1615, doi:10.1139/v90-248, 1990.
- Ervens, B., Turpin, B. J. and Weber, R. J.: Secondary organic aerosol formation in cloud droplets and aqueous particles (aqSOA): a review of laboratory, field and model studies, *Atmos. Chem. Phys.*, 11(21), 11069–11102, doi:10.5194/acp-11-11069-2011, 2011.
- Evoy, E., Maclean, A. M., Rovelli, G., Li, Y., Tsimpidi, A. P., Karydis, V. A., Kamal, S., Lelieveld, J., Shiraiwa, M., Reid, J. P. and Bertram, A. K.: Predictions of diffusion rates of large organic molecules in secondary organic aerosols using the Stokes-Einstein and fractional Stokes-Einstein relations, *Atmos. Chem. Phys.*, 19(15), 10073–10085, doi:10.5194/acp-19-10073-2019, 2019.
- Evoy, E., Kamal, S., Patey, G. N., Martin, S. T. and Bertram, A. K.: Unified Description of Diffusion Coefficients from Small to Large Molecules in Organic-Water Mixtures, *J. Phys. Chem. A*, 124(11), 2301–2308, doi:10.1021/acs.jpca.9b11271, 2020.
- Faiola, C. L., Pullinen, I., Buchholz, A., Khalaj, F., Ylisirniö, A., Kari, E., Miettinen, P., Holopainen, J. K., Kivimäenpää, M., Schobesberger, S., Yli-Juuti, T. and Virtanen, A.: Secondary Organic Aerosol Formation from Healthy and Aphid-Stressed Scots Pine Emissions, *ACS Earth Sp. Chem.*, 3(9), 1756–1772, doi:10.1021/acsearthspacechem.9b00118, 2019.
- Filippone, A.: *Flight Performance of Fixed and Rotary Wing Aircraft*, Elsevier Ltd, Oxford., 2006.
- Först, P., Werner, F. and Delgado, A.: On the pressure dependence of the viscosity of aqueous sugar solutions, *Rheol. Acta*, 41(4), 369–374, doi:10.1007/s00397-002-0238-y, 2002.
- Forstner, H. J. L., Flagan, R. C. and Seinfeld, J. H.: Secondary organic aerosol from the photooxidation of aromatic hydrocarbons: Molecular composition, *Environ. Sci. Technol.*, 31(5), 1345–1358, doi:10.1021/es9605376, 1997.
- Friedman, C. L., Pierce, J. R. and Selin, N. E.: Assessing the influence of secondary organic versus primary carbonaceous aerosols on long-range atmospheric polycyclic aromatic hydrocarbon transport, *Environ. Sci. Technol.*, 48(6), 3293–3302, doi:10.1021/es405219r, 2014.
- Frosch, M., Bilde, M., Nenes, A., Praplan, A. P., Jurányi, Z., Dommen, J., Gysel, M., Weingartner, E. and Baltensperger, U.: CCN activity and volatility of β -caryophyllene secondary organic aerosol, *Atmos. Chem. Phys.*, 13(4), 2283–2297, doi:10.5194/acp-13-2283-2013, 2013.
- Gallagher, J. P., McKendry, I. G., Macdonald, A. M. and Leitch, W. R.: Seasonal and Diurnal Variations in Aerosol Concentration on Whistler Mountain: Boundary Layer Influence and Synoptic-Scale Controls, *J. Appl. Meteorol. Climatol.*, 50(11), 2210–2222, doi:10.1175/JAMC-D-11-028.1, 2011.
- Gao, Y., Wang, H., Zhang, X., Jing, S., Peng, Y., Qiao, L., Zhou, M., Huang, D. D., Wang, Q., Li, X., Li, L., Feng, J., Ma, Y. and Li, Y.: Estimating Secondary Organic Aerosol Production from Toluene Photochemistry in a Megacity of China, *Environ. Sci. Technol.*, 53(15), 8664–8671, doi:10.1021/acs.est.9b00651, 2019.
- Gervasi, N. R., Topping, D. O. and Zuend, A.: A predictive group-contribution model for the viscosity of aqueous organic aerosol, *Atmos. Chem. Phys.*, 20(5), 2987–3008,

- doi:10.5194/acp-20-2987-2020, 2020.
- Glasius, M., Lahaniati, M., Calogirou, A., Di Bella, D., Jensen, N. R., Hjorth, J., Kotzias, D. and Larsen, B. R.: Carboxylic Acids in Secondary Aerosols from Oxidation of Cyclic Monoterpenes by Ozone, *Environ. Sci. Technol.*, 34(6), 1001–1010, doi:10.1021/es990445r, 2000.
- de Gouw, J. A., Brock, C. A., Atlas, E. L., Bates, T. S., Fehsenfeld, F. C., Goldan, P. D., Holloway, J. S., Kuster, W. C., Lerner, B. M., Matthew, B. M., Middlebrook, A. M., Onasch, T. B., Peltier, R. E., Quinn, P. K., Senff, C. J., Stohl, A., Sullivan, A. P., Trainer, M., Warneke, C., Weber, R. J. and Williams, E. J.: Sources of particulate matter in the northeastern United States in summer: 1. Direct emissions and secondary formation of organic matter in urban plumes, *J. Geophys. Res.*, 113(8), 1–19, doi:10.1029/2007JD009243, 2008.
- Grayson, J. W., Song, M., Sellier, M. and Bertram, A. K.: Validation of the poke-flow technique combined with simulations of fluid flow for determining viscosities in samples with small volumes and high viscosities, *Atmos. Meas. Tech.*, 8(6), 2463–2472, doi:10.5194/amt-8-2463-2015, 2015.
- Grayson, J. W., Zhang, Y., Mutzel, A., Renbaum-Wolff, L., Böge, O., Kamal, S., Herrmann, H., Martin, S. T. and Bertram, A. K.: Effect of varying experimental conditions on the viscosity of α -pinene derived secondary organic material, *Atmos. Chem. Phys.*, 16(10), 6027–6040, doi:10.5194/acp-16-6027-2016, 2016.
- Grayson, J. W., Evoy, E., Song, M., Chu, Y., Maclean, A., Nguyen, A., Upshur, M. A., Ebrahimi, M., Chan, C. K., Geiger, F. M., Thomson, R. J. and Bertram, A. K.: The effect of hydroxyl functional groups and molar mass on the viscosity of non-crystalline organic and organic-water particles, *Atmos. Chem. Phys.*, 17(13), 8509–8524, doi:10.5194/acp-17-8509-2017, 2017.
- Greenspan, L.: Humidity fixed points of binary saturated aqueous solutions, *J. Res. Natl. Bur. Stand. Sect. A Phys. Chem.*, 81A(1), 89, doi:10.6028/jres.081A.011, 1977.
- Guenther, A. B., Jiang, X., Heald, C. L., Sakulyanontvittaya, T., Duhl, T., Emmons, L. K. and Wang, X.: The Model of Emissions of Gases and Aerosols from Nature version 2.1 (MEGAN2.1): an extended and updated framework for modeling biogenic emissions, *Geosci. Model Dev.*, 5(6), 1471–1492, doi:10.5194/gmd-5-1471-2012, 2012.
- Hallett, J.: The temperature dependence of the viscosity of supercooled water, *Proc. Phys. Soc.*, 82(6), 1046–1050, doi:10.1088/0370-1328/82/6/326, 1963.
- Hallquist, M., Wenger, J. C., Baltensperger, U., Rudich, Y., Simpson, D., Claeys, M., Dommen, J., Donahue, N. M., George, C., Goldstein, A. H., Hamilton, J. F., Herrmann, H., Hoffmann, T., Iinuma, Y., Jang, M., Jenkin, M. E., Jimenez, J. L., Kiendler-Scharr, A., Maenhaut, W., McFiggans, G., Mentel, T. F., Monod, A., Prévôt, A. S. H., Seinfeld, J. H., Surratt, J. D., Szmigielski, R. and Wildt, J.: The formation, properties and impact of secondary organic aerosol: current and emerging issues, *Atmos. Chem. Phys.*, 9(14), 5155–5236, doi:10.5194/acp-9-5155-2009, 2009.
- Han, Z., Tang, X. and Zheng, B.: A PDMS viscometer for microliter Newtonian fluid, *J. Micromechanics Microengineering*, 17(9), 1828–1834, doi:10.1088/0960-1317/17/9/011, 2007.
- Heald, C. L., Jacob, D. J., Turquety, S., Hudman, R. C., Weber, R. J., Sullivan, A. P., Peltier, R. E., Atlas, E. L., de Gouw, J. A., Warneke, C., Holloway, J. S., Neuman, J. A., Flocke, F. M. and Seinfeld, J. H.: Concentrations and sources of organic carbon aerosols in the free

- troposphere over North America, *J. Geophys. Res. Atmos.*, 111(D23), 1–12, doi:10.1029/2006jd007705, 2006.
- Heald, C. L., Coe, H., Jimenez, J. L., Weber, R. J., Bahreini, R., Middlebrook, A. M., Russell, L. M., Jolleys, M., Fu, T. M., Allan, J. D., Bower, K. N., Capes, G., Crosier, J., Morgan, W. T., Robinson, N. H., Williams, P. I., Cubison, M. J., Decarlo, P. F. and Dunlea, E. J.: Exploring the vertical profile of atmospheric organic aerosol: comparing 17 aircraft field campaigns with a global model, *Atmos. Chem. Phys.*, 11(24), 12673–12696, doi:10.5194/acp-11-12673-2011, 2011.
- Helmig, D., Ortega, J., Duhl, T., Tanner, D., Guenther, A., Harley, P., Wiedinmyer, C. and Milford, J.: Sesquiterpene Emissions from Pine Trees - Identifications, Emission Rates and Flux Estimates for the Contiguous United States, *Environ. Sci. Technol.*, 1545–1553, doi:10.1021/es0618907, 2007.
- Hinks, M. L., Montoya-Aguilera, J., Ellison, L., Lin, P., Laskin, A., Laskin, J., Shiraiwa, M., Dabdub, D. and Nizkorodov, S. A.: Effect of relative humidity on the composition of secondary organic aerosol from the oxidation of toluene, *Atmos. Chem. Phys.*, 18(3), 1643–1652, doi:10.5194/acp-18-1643-2018, 2018.
- Hosny, N. A., Fitzgerald, C., Vyšniauskas, A., Athanasiadis, A., Berkemeier, T., Uygur, N., Pöschl, U., Shiraiwa, M., Kalberer, M., Pope, F. D. and Kuimova, M. K.: Direct imaging of changes in aerosol particle viscosity upon hydration and chemical aging, *Chem. Sci.*, 7(2), 1357–1367, doi:10.1039/C5SC02959G, 2016.
- Huff Hartz, K. E., Rosenørn, T., Ferchak, S. R., Raymond, T. M., Bilde, M., Donahue, N. M. and Pandis, S. N.: Cloud condensation nuclei activation of monoterpene and sesquiterpene secondary organic aerosol, *J. Geophys. Res. D Atmos.*, 110(14), 1–8, doi:10.1029/2004JD005754, 2005.
- Ignatius, K., Kristensen, T. B., Järvinen, E., Nichman, L., Fuchs, C., Gordon, H., Herenz, P., Hoyle, C. R., Duplissy, J., Garimella, S., Dias, A., Frege, C., Höppel, N., Tröstl, J., Wagner, R., Yan, C., Amorim, A., Baltensperger, U., Curtius, J., Donahue, N. M., Gallagher, M. W., Kirkby, J., Kulmala, M., Möhler, O., Saathoff, H., Schnaiter, M., Tomé, A., Virtanen, A., Worsnop, D. and Stratmann, F.: Heterogeneous ice nucleation of viscous secondary organic aerosol produced from ozonolysis of α -pinene, *Atmos. Chem. Phys.*, 16(10), 6495–6509, doi:10.5194/acp-16-6495-2016, 2016.
- Jain, S., Fischer, K. B. and Petrucci, G. A.: The influence of absolute mass loading of secondary organic aerosols on their phase state, *Atmosphere (Basel)*, 9(4), doi:10.3390/atmos9040131, 2018.
- Jang, M. S. and Kamens, R. M.: Characterization of Secondary Aerosol from the Photooxidation of Toluene in the Presence of NO_x and 1-Propene, *Environ. Sci. Technol.*, 35(18), 3626–3639, doi:10.1021/es010676+, 2001.
- Jaoui, M. and Kamens, R. M.: Gas and particulate products distribution from the photooxidation of α -humulene in the presence of NO_x, natural atmospheric air and sunlight, *J. Atmos. Chem.*, 46(1), 29–54, doi:10.1023/A:1024843525968, 2003a.
- Jaoui, M. and Kamens, R. M.: Gaseous and Particulate Oxidation Products Analysis of a Mixture of α -pinene + β -pinene/O₃/Air in the Absence of Light and α -pinene + β -pinene/NO_x/Air in the Presence of Natural Sunlight, *J. Atmos. Chem.*, 44(3), 259–297, doi:10.1023/A:1022977427523, 2003b.
- Järvinen, E., Ignatius, K., Nichman, L., Kristensen, T. B., Fuchs, C., Hoyle, C. R., Höppel, N., Corbin, J. C., Craven, J., Duplissy, J., Ehrhart, S., El Haddad, I., Frege, C., Gordon, H.,

- Jokinen, T., Kallinger, P., Kirkby, J., Kiselev, A., Naumann, K. H., Petäjä, T., Pinterich, T., Prevot, A. S. H., Saathoff, H., Schiebel, T., Sengupta, K., Simon, M., Slowik, J. G., Tröstl, J., Virtanen, A., Vochezer, P., Vogt, S., Wagner, A. C., Wagner, R., Williamson, C., Winkler, P. M., Yan, C., Baltensperger, U., Donahue, N. M., Flagan, R. C., Gallagher, M., Hansel, A., Kulmala, M., Stratmann, F., Worsnop, D. R., Möhler, O., Leisner, T. and Schnaiter, M.: Observation of viscosity transition in α -pinene secondary organic aerosol, *Atmos. Chem. Phys.*, 16(7), 4423–4438, doi:10.5194/acp-16-4423-2016, 2016.
- Jimenez, J. L., Canagaratna, M. R., Donahue, N. M., Prevot, A. S. H., Zhang, Q., Kroll, J. H., DeCarlo, P. F., Allan, J. D., Coe, H., Ng, N. L., Aiken, A. C., Docherty, K. S., Ulbrich, I. M., Grieshop, A. P., Robinson, A. L., Duplissy, J., Smith, J. D., Wilson, K. R., Lanz, V. A., Hueglin, C., Sun, Y. L., Tian, J., Laaksonen, A., Raatikainen, T., Rautiainen, J., Vaattovaara, P., Ehn, M., Kulmala, M., Tomlinson, J. M., Collins, D. R., Cubison, M. J., Dunlea, E. J., Huffman, J. A., Onasch, T. B., Alfarra, M. R., Williams, P. I., Bower, K., Kondo, Y., Schneider, J., Drewnick, F., Borrmann, S., Weimer, S., Demerjian, K., Salcedo, D., Cottrell, L., Griffin, R., Takami, A., Miyoshi, T., Hatakeyama, S., Shimojo, A., Sun, J. Y., Zhang, Y. M., Dzepina, K., Kimmel, J. R., Sueper, D., Jayne, J. T., Herndon, S. C., Trimborn, A. M., Williams, L. R., Wood, E. C., Middlebrook, A. M., Kolb, C. E., Baltensperger, U. and Worsnop, D. R.: Evolution of Organic Aerosols in the Atmosphere, *Science* (80-.), 326(5959), 1525–1529, doi:10.1126/science.1180353, 2009.
- Jin, S., Huang, P., Park, J., Yoo, J. Y. and Breuer, K. S.: Near-surface velocimetry using evanescent wave illumination, *Exp. Fluids*, 37(6), 825–833, doi:10.1007/s00348-004-0870-7, 2004.
- Jöckel, P., Tost, H., Pozzer, A., Brühl, C., Buchholz, J., Ganzeveld, L., Hoor, P., Kerkweg, A., Lawrence, M. G., Sander, R., Steil, B., Stiller, G., Tanarhte, M., Taraborrelli, D., Van Aardenne, J. and Lelieveld, J.: The atmospheric chemistry general circulation model ECHAM5/MESy1: Consistent simulation of ozone from the surface to the mesosphere, *Atmos. Chem. Phys.*, 6(12), 5067–5104, doi:10.5194/acp-6-5067-2006, 2006.
- Joly, L., Ybert, C. and Bocquet, L.: Probing the nanohydrodynamics at liquid-solid interfaces using thermal motion, *Phys. Rev. Lett.*, 96(4), doi:10.1103/PhysRevLett.96.046101, 2006.
- Joseph, P. and Tabeling, P.: Direct measurement of the apparent slip length, *Phys. Rev. E - Stat. Nonlinear, Soft Matter Phys.*, 71(3), 1–4, doi:10.1103/PhysRevE.71.035303, 2005.
- Kanakidou, M., Seinfeld, J. H., Pandis, S. N., Barnes, I., Dentener, F. J., Facchini, M. C., Van Dingenen, R., Ervens, B., Nenes, A., Nielsen, C. J., Swietlicki, E., Putaud, J. P., Balkanski, Y., Fuzzi, S., Horth, J., Moortgat, G. K., Winterhalter, R., Myhre, C. E. L., Tsigaridis, K., Vignati, E., Stephanou, E. G. and Wilson, J.: Organic aerosol and global climate modelling: a review, *Atmos. Chem. Phys.*, 5, 1053–1123, doi:10.5194/acp-5-1053-2005, 2005.
- Kasparoglu, S., Li, Y., Shiraiwa, M. and Petters, M.: Toward closure between predicted and observed particle viscosity over a wide range temperature and relative humidity, *Atmos. Chem. Phys. Discuss.*, (August), 1–22, 2020.
- Kenseth, C. M., Hafeman, N. J., Huang, Y., Dalleska, N. F., Stoltz, B. M. and Seinfeld, J. H.: Synthesis of Carboxylic Acid and Dimer Ester Surrogates to Constrain the Abundance and Distribution of Molecular Products in α -Pinene and β -Pinene Secondary Organic Aerosol, *Environ. Sci. Technol.*, doi:10.1021/acs.est.0c01566, 2020.
- Keyword, M. D., Kroll, J. H., Varutbangkul, V., Bahreini, R., Flagan, R. C. and Seinfeld, J. H.: Secondary organic aerosol formation from cyclohexene ozonolysis: Effect of OH scavenger and the role of radical chemistry, *Environ. Sci. Technol.*, 38(12), 3343–3350,

- doi:10.1021/es049725j, 2004.
- Khan, M. A. H., Jenkin, M. E., Foulds, A., Derwent, R. G., Percival, C. J. and Shallcross, D. E.: A modeling study of secondary organic aerosol formation from sesquiterpenes using the STOCHEM global chemistry and transport model, *J. Geophys. Res.*, 122(8), 4426–4439, doi:10.1002/2016JD026415, 2017.
- Kidd, C., Perraud, V., Wingen, L. M. and Finlayson-Pitts, B. J.: Integrating phase and composition of secondary organic aerosol from the ozonolysis of α -pinene, *Proc. Natl. Acad. Sci. U. S. A.*, 111(21), 7552–7557, doi:10.1073/pnas.1322558111, 2014.
- Kiland, K. J., Maclean, A. M., Kamal, S. and Bertram, A. K.: Diffusion of Organic Molecules as a Function of Temperature in a Sucrose Matrix (a Proxy for Secondary Organic Aerosol), *J. Phys. Chem. Lett.*, 10(19), 5902–5908, doi:10.1021/acs.jpcclett.9b02182, 2019.
- King, S. M., Rosenoern, T., Shilling, J. E., Chen, Q. and Martin, S. T.: Cloud condensation nucleus activity of secondary organic aerosol particles mixed with sulfate, *Geophys. Res. Lett.*, 34(24), 1–5, doi:10.1029/2007GL030390, 2007.
- King, S. M., Rosenoern, T., Shilling, J. E., Chen, Q. and Martin, S. T.: Increased cloud activation potential of secondary organic aerosol for atmospheric mass loadings, *Atmos. Chem. Phys.*, 9(9), 2959–2971, doi:10.5194/acp-9-2959-2009, 2009.
- Kleindienst, T. E., Smith, D. F., Li, W., Edney, E. O., Driscoll, D. J., Speer, R. E. and Weathers, W. S.: Secondary organic aerosol formation from the oxidation of aromatic hydrocarbons in the presence of dry submicron ammonium sulfate aerosol, *Atmos. Environ.*, 33(22), 3669–3681, doi:10.1016/S1352-2310(99)00121-1, 1999.
- Klodt, A. L., Romonosky, D. E., Lin, P., Laskin, J., Laskin, A. and Nizkorodov, S. A.: Aqueous Photochemistry of Secondary Organic Aerosol of α -Pinene and α -Humulene in the Presence of Hydrogen Peroxide or Inorganic Salts, *ACS Earth Sp. Chem.*, 3(12), 2736–2746, doi:10.1021/acsearthspacechem.9b00222, 2019.
- Knopf, D. A., Alpert, P. A. and Wang, B.: The Role of Organic Aerosol in Atmospheric Ice Nucleation: A Review, *ACS Earth Sp. Chem.*, 2(3), 168–202, doi:10.1021/acsearthspacechem.7b00120, 2018.
- Kohl, I., Bachmann, L., Hallbrucker, A., Mayer, E. and Loerting, T.: Liquid-like relaxation in hyperquenched water at ≤ 140 K, *Phys. Chem. Chem. Phys.*, 7(17), 3210–3220, doi:10.1039/b507651j, 2005.
- Koop, T., Bookhold, J., Shiraiwa, M. and Pöschl, U.: Glass transition and phase state of organic compounds: dependency on molecular properties and implications for secondary organic aerosols in the atmosphere, *Phys. Chem. Chem. Phys.*, 13(43), 19238–19255, doi:10.1039/c1cp22617g, 2011.
- Kourtchev, I., Szeto, P., O'Connor, I., Popoola, O. A. M., Maenhaut, W., Wenger, J. and Kalberer, M.: Comparison of Heated Electrospray Ionization and Nanoelectrospray Ionization Sources Coupled to Ultra-High-Resolution Mass Spectrometry for Analysis of Highly Complex Atmospheric Aerosol Samples, *Anal. Chem.*, 92(12), 8396–8403, doi:10.1021/acs.analchem.0c00971, 2020.
- Kroll, J. H., Donahue, N. M., Cee, V. J., Demerjian, K. L. and Anderson, J. G.: Gas-phase ozonolysis of alkenes: Formation of OH from anti carbonyl oxides, *J. Am. Chem. Soc.*, 124(29), 8518–8519, doi:10.1021/ja0266060, 2002.
- Larsen, B. R., Di Bella, D., Glasius, M., Winterhalter, R., Jensen, N. R. and Hjorth, J.: Gas-Phase OH Oxidation of Monoterpenes: Gaseous and Particulate Products, *J. Atmos. Chem.*, 38(3), 231–276, doi:10.1023/A:1006487530903, 2001.

- Li, D. Y., Jing, D. L., Pan, Y. L., Ahmad, K. and Zhao, X. Z.: Slip Length Measurement of Water Flow on Graphite Surface Using Atomic Force Microscope, *Adv. Mater. Res.*, 941–944, 1581–1584, doi:10.4028/www.scientific.net/amr.941-944.1581, 2014.
- Li, Y. and Shiraiwa, M.: Timescales of secondary organic aerosols to reach equilibrium at various temperatures and relative humidities, *Atmos. Chem. Phys.*, 19(9), 5959–5971, doi:10.5194/acp-19-5959-2019, 2019.
- Li, Y., Day, D. A., Stark, H., Jimenez, J. and Shiraiwa, M.: Predictions of the glass transition temperature and viscosity of organic aerosols by volatility distributions, *Atmos. Chem. Phys.*, 20(13), 8103–8122, doi:10.5194/acp-2019-1132, 2020.
- Li, Y. J., Chen, Q., Guzman, M. I., Chan, C. K. and Martin, S. T.: Second-generation products contribute substantially to the particle-phase organic material produced by β -caryophyllene ozonolysis, *Atmos. Chem. Phys.*, 11(1), 121–132, doi:10.5194/acp-11-121-2011, 2011.
- Li, Y. J., Liu, P. F., Gong, Z. H., Wang, Y., Bateman, A. P., Bergoend, C., Bertram, A. K. and Martin, S. T.: Chemical Reactivity and Liquid/Nonliquid States of Secondary Organic Material, *Environ. Sci. Technol.*, 49(22), 13264–13274, doi:10.1021/acs.est.5b03392, 2015.
- Lienhard, D. M., Huisman, A. J., Krieger, U. K., Rudich, Y., Marcolli, C., Luo, B. P., Bones, D. L., Reid, J. P., Lambe, A. T., Canagaratna, M. R., Davidovits, P., Onasch, T. B., Worsnop, D. R., Steimer, S. S., Koop, T. and Peter, T.: Viscous organic aerosol particles in the upper troposphere: diffusivity-controlled water uptake and ice nucleation?, *Atmos. Chem. Phys.*, 15(23), 13599–13613, doi:10.5194/acp-15-13599-2015, 2015.
- Liu, P., Li, Y. J., Wang, Y., Gilles, M. K., Zaveri, R. A., Bertram, A. K. and Martin, S. T.: Lability of secondary organic particulate matter., *Proc. Natl. Acad. Sci. U. S. A.*, 113(45), 12643–12648, doi:10.1073/pnas.1603138113, 2016.
- Longinotti, M. P. and Corti, H. R.: Viscosity of concentrated sucrose and trehalose aqueous solutions including the supercooled regime, *J. Phys. Chem. Ref. Data*, 37(3), 1503–1515, doi:10.1063/1.2932114, 2008.
- Lundqvist, L., Ahlström, M. A., Petter Axelsson, E., Mörling, T. and Valinger, E.: Multi-layered Scots pine forests in boreal Sweden result from mass regeneration and size stratification, *For. Ecol. Manage.*, 441(March), 176–181, doi:10.1016/j.foreco.2019.03.044, 2019.
- Maclean, A. M., Butenhoff, C. L., Grayson, J. W., Barsanti, K., Jimenez, J. L. and Bertram, A. K.: Mixing times of organic molecules within secondary organic aerosol particles: A global planetary boundary layer perspective, *Atmos. Chem. Phys.*, 17(21), 13037–13048, doi:10.5194/acp-17-13037-2017, 2017.
- Malloy, Q. G. J., Nakao, S., Qi, L., Austin, R., Stothers, C., Hagino, H. and Cocker, D. R.: Real-Time aerosol density determination utilizing a modified scanning mobility particle sizer aerosol particle mass analyzer system, *Aerosol Sci. Technol.*, 43(7), 673–678, doi:10.1080/02786820902832960, 2009.
- Marsh, A., Petters, S. S., Rothfuss, N. E., Rovelli, G., Song, Y. C., Reid, J. P. and Petters, M. D.: Amorphous phase state diagrams and viscosity of ternary aqueous organic/organic and inorganic/organic mixtures, *Phys. Chem. Chem. Phys.*, 20(22), 15086–15097, doi:10.1039/c8cp00760h, 2018.
- Martin, S. T.: Phase transitions of aqueous atmospheric particles, *Chem. Rev.*, 100(9), 3403–3453, doi:10.1021/cr990034t, 2000.
- Martin, S. T., Andreae, M. O., Althausen, D., Artaxo, P., Baars, H., Borrmann, S., Chen, Q., Farmer, D. K., Guenther, A., Gunthe, S. S., Jimenez, J. L., Karl, T., Longo, K., Manzi, A., Müller, T., Pauliquevis, T., Petters, M. D., Prenni, A. J., Pöschl, U., Rizzo, L. V., Schneider,

- J., Smith, J. N., Swietlicki, E., Tota, J., Wang, J., Wiedensohler, A. and Zorn, S. R.: An overview of the Amazonian Aerosol Characterization Experiment 2008 (AMAZE-08), *Atmos. Chem. Phys.*, 10(23), 11415–11438, doi:10.5194/acp-10-11415-2010, 2010.
- Migliori, M., Gabriele, D., Di Sanzo, R., De Cindio, B. and Correr, S.: Viscosity of multicomponent solutions of simple and complex sugars in water, *J. Chem. Eng. Data*, 52(4), 1347–1353, doi:10.1021/je700062x, 2007.
- Mikhailov, E., Vlasenko, S., Martin, S. T., Koop, T. and Pöschl, U.: Amorphous and crystalline aerosol particles interacting with water vapor: conceptual framework and experimental evidence for restructuring, phase transitions and kinetic limitations, *Atmos. Chem. Phys.*, 9(24), 9491–9522, 2009.
- Mu, Q., Shiraiwa, M., Octaviani, M., Ma, N., Ding, A., Su, H., Lammel, G., Pöschl, U. and Cheng, Y.: Temperature effect on phase state and reactivity controls atmospheric multiphase chemistry and transport of PAHs, *Sci. Adv.*, 4(3), doi:10.1126/sciadv.aap7314, 2018.
- Muchlinski, A., Chen, X., Lovell, J. T., Köllner, T. G., Pelot, K. A., Zerbe, P., Ruggiero, M., Callaway, L. M., Laliberte, S., Chen, F. and Tholl, D.: Biosynthesis and Emission of Stress-Induced Volatile Terpenes in Roots and Leaves of Switchgrass (*Panicum virgatum* L.), *Front. Plant Sci.*, 10(September), 1–16, doi:10.3389/fpls.2019.01144, 2019.
- Murray, B. J., Wilson, T. W., Dobbie, S., Cui, Z., Al-Jumur, S. M. R. K., Möhler, O., Schnaiter, M., Wagner, R., Benz, S., Niemand, M., Saathoff, H., Ebert, V., Wagner, S. and Kärcher, B.: Heterogeneous nucleation of ice particles on glassy aerosols under cirrus conditions, *Nat. Geosci.*, 3(4), 233–237, doi:10.1038/ngeo817, 2010.
- Murray, B. J., Haddrell, A. E., Peppe, S., Davies, J. F., Reid, J. P., O’Sullivan, D., Price, H. C., Kumar, R., Saunders, R. W., Plane, J. M. C., Umo, N. S. and Wilson, T. W.: Glass formation and unusual hygroscopic growth of iodic acid solution droplets with relevance for iodine mediated particle formation in the marine boundary layer, *Atmos. Chem. Phys.*, 12(18), 8575–8587, doi:10.5194/acp-12-8575-2012, 2012.
- National Institute of Standards and Technology: Water, [online] Available from: <http://webbook.nist.gov/cgi/cbook.cgi?ID=C7732185&Mask=4&Type=ANTOINE&Plot=on#ANTOINE> (Accessed 1 August 2016), 2016.
- Neto, C., Evans, D. R., Bonaccorso, E., Butt, H. J. and Craig, V. S. J.: Boundary slip in Newtonian liquids: A review of experimental studies, *Reports Prog. Phys.*, 68(12), 2859–2897, doi:10.1088/0034-4885/68/12/R05, 2005.
- Ng, N. L., Kroll, J. H., Chan, A. W. H., Chhabra, P. S., Flagan, R. C., Ng, N. L., Kroll, J. H., Chan, A. W. H., Chhabra, P. S. and Flagan, R. C.: Secondary organic aerosol formation from m-xylene, toluene, and benzene, 2007.
- Ng, N. L., Canagaratna, M. R., Zhang, Q., Jimenez, J. L., Tian, J., Ulbrich, I. M., Kroll, J. H., Docherty, K. S., Chhabra, P. S., Bahreini, R., Murphy, S. M., Seinfeld, J. H., Hildebrandt, L., Donahue, N. M., Decarlo, P. F., Lanz, V. A., Prévôt, A. S. H., Dinar, E., Rudich, Y. and Worsnop, D. R.: Organic aerosol components observed in Northern Hemispheric datasets from Aerosol Mass Spectrometry, *Atmos. Chem. Phys.*, 10(10), 4625–4641, doi:10.5194/acp-10-4625-2010, 2010.
- Nguyen, Q. T., Glasius, M., Sørensen, L. L., Jensen, B., Skov, H., Birmili, W., Wiedensohler, A., Kristensson, A., Nøjgaard, J. K. and Massling, A.: Seasonal variation of atmospheric particle number concentrations, new particle formation and atmospheric oxidation capacity at the high Arctic site Villum Research Station, Station Nord, *Atmos. Chem. Phys.*, 16(17),

- 11319–11336, doi:10.5194/acp-16-11319-2016, 2016.
- Nguyen, T. B., Nizkorodov, S. A., Laskin, A. and Laskin, J.: An approach toward quantification of organic compounds in complex environmental samples using high-resolution electrospray ionization mass spectrometry, *Anal. Methods*, 5(1), 72–80, doi:10.1039/c2ay25682g, 2013.
- Nizkorodov, S. A., Laskin, J. and Laskin, A.: Molecular chemistry of organic aerosols through the application of high resolution mass spectrometry, *Phys. Chem. Chem. Phys.*, 13(9), 3612–3629, doi:10.1039/c0cp02032j, 2011.
- Pajunoja, A., Malila, J., Hao, L., Joutsensaari, J., Lehtinen, K. E. J. and Virtanen, A.: Estimating the Viscosity Range of SOA Particles Based on Their Coalescence Time, *Aerosol Sci. Technol.*, 48(August 2016), i–iv, doi:10.1080/02786826.2013.870325, 2014.
- Pajunoja, A., Lambe, A. T., Hakala, J., Rastak, N., Cummings, M. J., Brogan, J. F., Hao, L., Paramonov, M., Hong, J., Prisle, N. L., Malila, J., Romakkaniemi, S., Lehtinen, K. E. J., Laaksonen, A., Kulmala, M., Massoli, P., Onasch, T. B., Donahue, N. M., Riipinen, I., Davidovits, P., Worsnop, D. R., Petäjä, T. and Virtanen, A.: Adsorptive uptake of water by semisolid secondary organic aerosols, *Geophys. Res. Lett.*, 42(8), 3063–3068, doi:10.1002/2015gl063142, 2015.
- Pajunoja, A., Hu, W., Leong, Y. J., Taylor, N. F., Miettinen, P., Palm, B. B., Mikkonen, S., Collins, D. R., Jimenez, J. L. and Virtanen, A.: Phase state of ambient aerosol linked with water uptake and chemical aging in the southeastern US, *Atmos. Chem. Phys.*, 16(17), 11163–11176, doi:10.5194/acp-16-11163-2016, 2016.
- Pandis, S. N., Harley, R. A., Cass, G. R. and Seinfeld, J. H.: Secondary organic aerosol formation and transport, *Atmos. Environ. Part A, Gen. Top.*, 26(13), 2269–2282, doi:10.1016/0960-1686(92)90358-R, 1992.
- Pankow, J. F.: An absorption model of the gas/aerosol partitioning involved in the formation of secondary organic aerosol, *Atmos. Environ.*, 28, 189–193, doi:10.1016/j.atmosenv.2007.10.060, 1994.
- Parsons, M. T., Sydoryk, I., Lim, A., McIntyre, T. J., Tulip, J., Jäger, W. and McDonald, K.: Real-time monitoring of benzene, toluene, and p-xylene in a photoreaction chamber with a tunable mid-infrared laser and ultraviolet differential optical absorption spectroscopy, *Appl. Opt.*, 50(4), doi:10.1364/AO.50.000A90, 2011.
- Perraud, V., Bruns, E. A., Ezell, M. J., Johnson, S. N., Yu, Y., Alexander, M. L., Zelenyuk, A., Imre, D., Chang, W. L., Dabdub, D., Pankow, J. F. and Finlayson-Pitts, B. J.: Nonequilibrium atmospheric secondary organic aerosol formation and growth, *Proc. Natl. Acad. Sci. U. S. A.*, 109(8), 2836–2841, doi:10.1073/pnas.1119909109, 2012.
- Perry, R. and Green, D.: *Perry's Chemical Engineers' Handbook*, McGraw-Hill, Toronto., 2008.
- Petters, M. D. and Kreidenweis, S. M.: A single parameter representation of hygroscopic growth and cloud condensation nucleus activity, *Atmos. Chem. Phys.*, 7(8), 1961–1971, doi:10.5194/acp-8-6273-2008, 2007.
- Pöschl, U., Martin, S. T., Sinha, B., Chen, Q., Gunthe, S. S., Huffman, J. A., Borrmann, S., Farmer, D. K., Garland, R. M., Helas, G., Jimenez, J. L., King, S. M., Manzi, A., Mikhailov, E., Pauliquevis, T., Petters, M. D., Prenni, A. J., Roldin, P., Rose, D., Schneider, J., Su, H., Zorn, S. R., Artaxo, P. and Andreae, M. O.: Rainforest aerosols as biogenic nuclei of clouds and precipitation in the Amazon., *Science*, 329(5998), 1513–6, doi:10.1126/science.1191056, 2010.
- Power, R. M. and Reid, J. P.: Probing the micro-rheological properties of aerosol particles using

- optical tweezers, *Reports Prog. Phys.*, 77(7), doi:10.1088/0034-4885/77/7/074601, 2014.
- Power, R. M., Simpson, S. H., Reid, J. P. and Hudson, A. J.: The transition from liquid to solid-like behaviour in ultrahigh viscosity aerosol particles, *Chem. Sci.*, 4(6), 2597–2604, doi:10.1039/c3sc50682g, 2013.
- Pratap, V., Chen, Y., Yao, G. and Nakao, S.: Temperature effects on multiphase reactions of organic molecular markers: A modeling study, *Atmos. Environ.*, 179(February), 40–48, doi:10.1016/j.atmosenv.2018.02.009, 2018.
- Prather, K. A., Hatch, C. D. and Grassian, V. H.: Analysis of Atmospheric Aerosols, *Annu. Rev. Anal. Chem.*, 1(1), 485–514, doi:10.1146/annurev.anchem.1.031207.113030, 2008.
- Price, H. C., Murray, B. J., Mattsson, J., O’Sullivan, D., Wilson, T. W., Baustian, K. J. and Benning, L. G.: Quantifying water diffusion in high-viscosity and glassy aqueous solutions using a Raman isotope tracer method, *Atmos. Chem. Phys.*, 14(8), 3817–3830, doi:10.5194/acp-14-3817-2014, 2014.
- Price, H. C., Mattsson, J., Zhang, Y., Bertram, A. K., Davies, J. F., Grayson, J. W., Martin, S. T., O’Sullivan, D., Reid, J. P., Rickards, A. M. J. and Murray, B. J.: Water diffusion in atmospherically relevant α -pinene secondary organic material, *Chem. Sci.*, 6(8), 4876–4883, doi:10.1039/c5sc00685f, 2015.
- Price, H. C., Mattsson, J. and Murray, B. J.: Sucrose diffusion in aqueous solution, *Phys. Chem. Chem. Phys.*, 18(28), 19207–19216, doi:10.1039/C6CP03238A, 2016.
- Pye, H. O. T. and Seinfeld, J. H.: A global perspective on aerosol from low-volatility organic compounds, *Atmos. Chem. Phys.*, 10(9), 4377–4401, doi:10.5194/acp-10-4377-2010, 2010.
- Pye, H. O. T., Chan, A. W. H., Barkley, M. P. and Seinfeld, J. H.: Global modeling of organic aerosol: The importance of reactive nitrogen (NO_x and NO₃), *Atmos. Chem. Phys.*, 10(22), 11261–11276, doi:10.5194/acp-10-11261-2010, 2010.
- Quintas, M., Brandão, T. R. S., Silva, C. L. M. and Cunha, R. L.: Rheology of supersaturated sucrose solutions, *J. Food Eng.*, 77(4), 844–852, doi:10.1016/j.jfoodeng.2005.08.011, 2006.
- Raatikainen, T., Vaattovaara, P., Tiitta, P., Miettinen, P., Rautiainen, J., Ehn, M., Kulmala, M., Laaksonen, A. and Worsnop, D. R.: Physicochemical properties and origin of organic groups detected in boreal forest using an aerosol mass spectrometer, *Atmos. Chem. Phys.*, 10(4), 2063–2077, doi:10.5194/acp-10-2063-2010, 2010.
- Recondo, M. P., Elizalde, B. E. and Buera, M. P.: Modeling temperature dependence of honey viscosity and of related supersaturated model carbohydrate systems, *J. Food Eng.*, 77(1), 126–134, doi:10.1016/j.jfoodeng.2005.06.054, 2006.
- Reid, J. P., Bertram, A. K., Topping, D. O., Laskin, A., Martin, S. T., Petters, M. D., Pope, F. D. and Rovelli, G.: The viscosity of atmospherically relevant organic particles, *Nat. Commun.*, 9(1), 1–14, doi:10.1038/s41467-018-03027-z, 2018.
- Reist, P. C.: *Aerosol Science and Technology*, 2nd ed., McGraw-Hill Professional, New York, NY, USA., 1992.
- Renbaum-Wolff, L., Grayson, J. W., Bateman, A. P., Kuwata, M., Sellier, M., Murray, B. J., Shilling, J. E., Martin, S. T. and Bertram, A. K.: Viscosity of α -pinene secondary organic material and implications for particle growth and reactivity, *Proc. Natl. Acad. Sci. U. S. A.*, 110(20), 8014–8019, doi:10.1073/pnas.1219548110, 2013.
- Richters, S., Herrmann, H. and Berndt, T.: Different pathways of the formation of highly oxidized multifunctional organic compounds (HOMs) from the gas-phase ozonolysis of β -caryophyllene, *Atmos. Chem. Phys.*, 16(15), 9831–9845, doi:10.5194/acp-16-9831-2016, 2016.

- Riipinen, I., Pierce, J. R., Yli-Juuti, T., Nieminen, T., Hakkinen, S., Ehn, M., Junninen, H., Lehtipalo, K., Petaja, T., Slowik, J., Chang, R., Shantz, N. C., Abbatt, J., Leaitch, W. R., Kerminen, V. M., Worsnop, D. R., Pandis, S. N., Donahue, N. M. and Kulmala, M.: Organic condensation: a vital link connecting aerosol formation to cloud condensation nuclei (CCN) concentrations, *Atmos. Chem. Phys.*, 11(8), 3865–3878, doi:10.5194/acp-11-3865-2011, 2011.
- Riva, M., Chen, Y., Zhang, Y., Lei, Z., Olson, N. E., Boyer, H. C., Narayan, S., Yee, L. D., Green, H. S., Cui, T., Zhang, Z., Baumann, K., Fort, M., Edgerton, E., Budisulistiorini, S. H., Rose, C. A., Ribeiro, I. O., Oliveira, R. L. E., Dos Santos, E. O., Machado, C. M. D., Szopa, S., Zhao, Y., Alves, E. G., De Sá, S. S., Hu, W., Knipping, E. M., Shaw, S. L., Duvoisin Junior, S., De Souza, R. A. F., Palm, B. B., Jimenez, J. L., Glasius, M., Goldstein, A. H., Pye, H. O. T., Gold, A., Turpin, B. J., Vizuete, W., Martin, S. T., Thornton, J. A., Dutcher, C. S., Ault, A. P. and Surratt, J. D.: Increasing Isoprene Epoxydiol-to-Inorganic Sulfate Aerosol Ratio Results in Extensive Conversion of Inorganic Sulfate to Organosulfur Forms: Implications for Aerosol Physicochemical Properties, *Environ. Sci. Technol.*, 53(15), 8682–8694, doi:10.1021/acs.est.9b01019, 2019.
- Roach, P. J., Laskin, J. and Laskin, A.: Nanospray desorption electrospray ionization: An ambient method for liquid-extraction surface sampling in mass spectrometry, *Analyst*, 135(9), 2233–2236, doi:10.1039/c0an00312c, 2010.
- Robinson, E. S., Saleh, R. and Donahue, N. M.: Organic aerosol mixing observed by single-particle mass spectrometry, *J. Phys. Chem. A*, 117(51), 13935–13945, doi:10.1021/jp405789t, 2013.
- Romonosky, D. E., Li, Y., Shiraiwa, M., Laskin, A., Laskin, J. and Nizkorodov, S. A.: Aqueous Photochemistry of Secondary Organic Aerosol of α -Pinene and α -Humulene Oxidized with Ozone, Hydroxyl Radical, and Nitrate Radical, *J. Phys. Chem. A*, 121(6), 1298–1309, doi:10.1021/acs.jpca.6b10900, 2017.
- Roos, Y.: Melting and glass transitions weight carbohydrates of low molecular, *Carbohydr. Res.*, 238, 39–48, doi:10.1016/0008-6215(93)87004-C, 1993.
- Rosencranz, R. and Bogen, S. A.: Clinical laboratory measurement of serum, plasma, and blood viscosity., *Am. J. Clin. Pathol.*, 125 Suppl(Suppl 1), doi:10.1309/FFF7U8RRPK26VAPY, 2006.
- Rothfuss, N. E. and Petters, M. D.: Characterization of the Temperature and Humidity-Dependent Phase Diagram of Amorphous Nanoscale Organic Aerosols, *Phys. Chem. Chem. Phys.*, 19, 6532–6545, doi:10.1039/C6CP08593H, 2017a.
- Rothfuss, N. E. and Petters, M. D.: Influence of Functional Groups on the Viscosity of Organic Aerosol, *Environ. Sci. Technol.*, 51(1), 271–279, doi:10.1021/acs.est.6b04478, 2017b.
- Rovelli, G., Song, Y.-C., MacLean, A. M., Topping, D. O., Bertram, A. K. and Reid, J. P.: Comparison of Approaches for Measuring and Predicting the Viscosity of Ternary Component Aerosol Particles, *Anal. Chem.*, 91(8), 5074–5082, doi:10.1021/acs.analchem.8b05353, 2019.
- Ruiz, L. H., Paciga, A. L., Cerully, K. M., Nenes, A., Donahue, N. M. and Pandis, S. N.: Formation and aging of secondary organic aerosol from toluene: changes in chemical composition, volatility, and hygroscopicity, *Atmos. Chem. Phys.*, 15(14), 8301–8313, doi:10.5194/acp-15-8301-2015, 2015.
- Russell, L. M., Bahadur, R. and Ziemann, P. J.: Identifying organic aerosol sources by comparing functional group composition in chamber and atmospheric particles, *Proc. Natl.*

- Acad. Sci. U. S. A., 108(9), 3516–3521, doi:10.1073/pnas.1006461108, 2011.
- Saathoff, H., Naumann, K.-H., Moehler, O., Jonsson, A. M., Hallquist, M., Kiendler-Scharr, A., Mentel, T. F., Tillmann, R. and Schurath, U.: Temperature dependence of yields of secondary organic aerosols from the ozonolysis of alpha-pinene and limonene, *Atmos. Chem. Phys.*, 9(5), 1551–1577, doi:10.5194/acp-9-1551-2009, 2009.
- Sakulyanontvittaya, T., Guenther, A., Helmig, D., Milford, J. and Wiedinmyer, C.: Secondary Organic Aerosol from Sesquiterpene and Monoterpene Emissions in the United States, *Environ. Sci. Technol.*, 42(23), 8784–8790, doi:10.1021/es800817r, 2008.
- Saukko, E., Kuuluvainen, H. and Virtanen, A.: A method to resolve the phase state of aerosol particles, *Atmos. Meas. Tech.*, 5(1), 259–265, doi:10.5194/amt-5-259-2012, 2012a.
- Saukko, E., Lambe, A. T., Massoli, P., Koop, T., Wright, J. P., Croasdale, D. R., Pedernera, D. A., Onasch, T. B., Laaksonen, A., Davidovits, P., Worsnop, D. R. and Virtanen, A.: Humidity-dependent phase state of SOA particles from biogenic and anthropogenic precursors, *Atmos. Chem. Phys.*, 12(16), 7517–7529, doi:10.5194/acp-12-7517-2012, 2012b.
- Schmedding, R., Rasool, Q. Z., Zhang, Y., Pye, H. O. T., Zhang, H., Chen, Y., Surratt, J. D., Lopez-Hilfiker, F. D., Thornton, J. A., Goldstein, A. H. and Vizuete, W.: Predicting secondary organic aerosol phase state and viscosity and its effect on multiphase chemistry in a regional-scale air quality model, *Atmos. Chem. Phys.*, 20(13), 8201–8225, doi:10.5194/acp-20-8201-2020, 2020.
- Schnell, E.: Slippage of water over nonwetable surfaces, *J. Appl. Phys.*, 27(10), 1149–1152, doi:10.1063/1.1722220, 1956.
- Schum, S. K., Zhang, B., Dzepina, K., Fialho, P., Mazzoleni, C. and Mazzoleni, L. R.: Molecular and physical characteristics of aerosol at a remote free troposphere site: Implications for atmospheric aging, *Atmos. Chem. Phys.*, 18(19), 14017–14036, doi:10.5194/acp-18-14017-2018, 2018.
- Schwartz, J., Dockery, D. W. and Neas, L. M.: Is Daily Mortality Associated Specifically with Fine Particles?, *J. Air Waste Manag. Assoc.*, 46(10), 927–939, doi:10.1080/10473289.1996.10467528, 1996.
- Seinfeld, J. H. and Pandis, S. N.: *Atmospheric Chemistry and Physics*, 2nd Ed., John Wiley and Sons, Hoboken, NJ., 2006.
- Shilling, J. E., Chen, Q., King, S. M., Rosenoern, T., Kroll, J. H., Worsnop, D. R., McKinney, K. A. and Martin, S. T.: Particle mass yield in secondary organic aerosol formed by the dark ozonolysis of α -pinene, *Atmos. Chem. Phys.*, 8(7), 2073–2088, doi:10.5194/acp-8-2073-2008, 2008.
- Shiraiwa, M. and Seinfeld, J. H.: Equilibration timescale of atmospheric secondary organic aerosol partitioning, *Geophys. Res. Lett.*, 39, doi:10.1029/2012gl054008, 2012.
- Shiraiwa, M., Ammann, M., Koop, T. and Pöschl, U.: Gas uptake and chemical aging of semisolid organic aerosol particles, *Proc. Natl. Acad. Sci. U. S. A.*, 108(27), 11003–11008, doi:10.1073/pnas.1103045108, 2011.
- Shiraiwa, M., Ueda, K., Pozzer, A., Lammel, G., Kampf, C. J., Fushimi, A., Enami, S., Arangio, A. M., Fröhlich-Nowoisky, J., Fujitani, Y., Furuyama, A., Lakey, P. S. J., Lelieveld, J., Lucas, K., Morino, Y., Pöschl, U., Takahama, S., Takami, A., Tong, H., Weber, B., Yoshino, A. and Sato, K.: *Aerosol Health Effects from Molecular to Global Scales*, *Environ. Sci. Technol.*, 51(23), 13545–13567, doi:10.1021/acs.est.7b04417, 2017a.
- Shiraiwa, M., Li, Y., Tsimpidi, A. P., Karydis, V. A., Berkemeier, T., Pandis, S. N., Lelieveld, J.,

- Koop, T. and Pöschl, U.: Global distribution of particle phase state in atmospheric secondary organic aerosols, *Nat. Commun.*, doi:10.1038/ncomms15002, 2017b.
- Shrivastava, M., Lou, S., Zelenyuk, A., Easter, R. C., Corley, R. A., Thrall, B. D., Rasch, P. J., Fast, J. D., Simonich, S. L. M., Shen, H. and Tao, S.: Global long-range transport and lung cancer risk from polycyclic aromatic hydrocarbons shielded by coatings of organic aerosol, *Proc. Natl. Acad. Sci. U. S. A.*, 114(6), 1246–1251, doi:10.1073/pnas.1618475114, 2017.
- Simperler, A., Kornherr, A., Chopra, R., Bonnet, P. A., Jones, W., Motherwell, W. D. S. and Zifferer, G.: Glass transition temperature of glucose, sucrose, and trehalose: An experimental and in silico study, *J. Phys. Chem. B*, 110(39), 19678–19684, doi:10.1021/jp063134t, 2006.
- Slade, J. H., Ault, A. P., Bui, A. T., Ditto, J. C., Lei, Z., Bondy, A. L., Olson, N. E., Cook, R. D., Desrochers, S. J., Harvey, R. M., Erickson, M. H., Wallace, H. W., Alvarez, S. L., Flynn, J. H., Boor, B. E., Petrucci, G. A., Gentner, D. R., Griffin, R. J. and Shepson, P. B.: Bouncer Particles at Night: Biogenic Secondary Organic Aerosol Chemistry and Sulfate Drive Diel Variations in the Aerosol Phase in a Mixed Forest, *Environ. Sci. Technol.*, 53(9), 4977–4987, doi:10.1021/acs.est.8b07319, 2019.
- Smith, N. R., Crescenzo, G., Huang, Y., Hettiyadura, A., Siemens, K., Li, Y., Faiola, C. L., Laskin, A., Bertram, A. K., Shiraiwa, M. and Nizkorodov, S. A.: Highly Viscous Secondary Organic Aerosol from Healthy and Stressed Pine Trees, to be Submitted, 2020.
- Song, M., Liu, P. F., Hanna, S. J., Li, Y. J., Martin, S. T. and Bertram, A. K.: Relative humidity-dependent viscosities of isoprene-derived secondary organic material and atmospheric implications for isoprene-dominant forests, *Atmos. Chem. Phys.*, 15(9), 5145–5159, doi:10.5194/acp-15-5145-2015, 2015.
- Song, M., Maclean, A. M., Huang, Y., Smith, N. R., Blair, S. L., Laskin, J., Laskin, A., DeRieux, W.-S. W., Li, Y., Shiraiwa, M., Nizkorodov, S. A. and Bertram, A. K.: Liquid-liquid phase separation and viscosity within secondary organic aerosol generated from diesel fuel vapors, *Atmos. Chem. Phys.*, 19, 12515–12529, doi:10.5194/acp-2019-367, 2019.
- Song, M. J., Liu, P. F. F., Hanna, S. J., Zaveri, R. A., Potter, K., You, Y., Martin, S. T. and Bertram, A. K.: Relative humidity-dependent viscosity of secondary organic material from toluene photo-oxidation and possible implications for organic particulate matter over megacities, *Atmos. Chem. Phys.*, 16(14), 8817–8830, doi:10.5194/acp-16-8817-2016, 2016a.
- Song, Y. C., Haddrell, A. E., Bzdek, B. R., Reid, J. P., Bannan, T., Topping, D. O., Percival, C. and Cai, C.: Measurements and Predictions of Binary Component Aerosol Particle Viscosity, *J. Phys. Chem. A*, 120(41), 8123–8137, doi:10.1021/acs.jpca.6b07835, 2016b.
- Spracklen, D. V., Carslaw, K. S., Merikanto, J., Mann, G. W., Reddington, C. L., Pickering, S., Ogren, J. A., Andrews, E., Baltensperger, U., Weingartner, E., Boy, M., Kulmala, M., Laakso, L., Lihavainen, H., Kivekäs, N., Komppula, M., Mihalopoulos, N., Kouvarakis, G., Jennings, S. G., O'Dowd, C., Birmili, W., Wiedensohler, A., Weller, R., Gras, J., Laj, P., Sellegri, K., Bonn, B., Krejci, R., Laaksonen, A., Hamed, A., Minikin, A., Harrison, R. M., Talbot, R. and Sun, J.: Explaining global surface aerosol number concentrations in terms of primary emissions and particle formation, *Atmos. Chem. Phys.*, 10(10), 4775–4793, doi:10.5194/acp-10-4775-2010, 2010.
- Spracklen, D. V., Jimenez, J. L., Carslaw, K. S., Worsnop, D. R., Evans, M. J., Mann, G. W., Zhang, Q., Canagaratna, M. R., Allan, J., Coe, H., McFiggans, G., Rap, A. and Forster, P.: Aerosol mass spectrometer constraint on the global secondary organic aerosol budget,

- Atmos. Chem. Phys., 11(23), 12109–12136, doi:10.5194/acp-11-12109-2011, 2011.
- Srivastava, N. and Burns, M. A.: Analysis of non-Newtonian liquids using a microfluidic capillary viscometer, *Anal. Chem.*, 78(5), 1690–1696, doi:10.1021/ac0518046, 2006.
- Stocker, T. F., Qin, D., Plattner, G.-K., Tignor, M. M. B., Allen, S. K., Boschung, J., Nauels, A., Xia, Y., Bex, V. and Midgley, P. M., Eds.: IPCC 2013: Climate Change 2013: The Physical Science Basis. Contribution of Working Group I to the Fifth Assessment Report of the Intergovernmental Panel on Climate Change, Cambridge Univ Press, Cambridge, UK., 2013.
- Surratt, J. D., Chan, A. W. H., Eddingsaas, N. C., Chan, M. N., Loza, C. L., Kwan, A. J., Hersey, S. P., Flagan, R. C., Wennberg, P. O. and Seinfeld, J. H.: Reactive intermediates revealed in secondary organic aerosol formation from isoprene, *Proc. Natl. Acad. Sci. U. S. A.*, 107(15), 6640–6645, doi:10.1073/pnas.0911114107, 2010.
- Swindells, J. F. and States., U.: Viscosities of sucrose solutions at various temperatures: tables of recalculated values, , 7 [online] Available from: file://catalog.hathitrust.org/Record/007290919, 1958.
- Takegawa, N., Miyakawa, T., Kondo, Y., Jimenez, J. L., Zhang, Q., Worsnop, D. R. and Fukuda, M.: Seasonal and diurnal variations of submicron organic aerosol in Tokyo observed using the Aerodyne aerosol mass spectrometer, *J. Geophys. Res. Atmos.*, 111(11), 1–17, doi:10.1029/2005JD006515, 2006.
- Tasoglou, A. and Pandis, S. N.: Formation and chemical aging of secondary organic aerosol during the β -caryophyllene oxidation, *Atmos. Chem. Phys.*, 15, 6035–6046, doi:10.5194/acp-15-6035-2015, 2015.
- Telis, V. R. N., Telis-Romero, J., Mazzotti, H. B. and Gabas, a. L.: Viscosity of Aqueous Carbohydrate Solutions at Different Temperatures and Concentrations, *Int. J. Food Prop.*, 10(1), 185–195, doi:10.1080/10942910600673636, 2007.
- Tong, H. J., Reid, J. P., Bones, D. L., Luo, B. P. and Krieger, U. K.: Measurements of the timescales for the mass transfer of water in glassy aerosol at low relative humidity and ambient temperature, *Atmos. Chem. Phys.*, 11(10), 4739–4754, doi:10.5194/acp-11-4739-2011, 2011.
- Tretheway, D. C. and Meinhart, C. D.: Apparent fluid slip at hydrophobic microchannel walls, *Phys. Fluids*, 14(3), doi:10.1063/1.1432696, 2002.
- Tsimpidi, A. P., Karydis, V. A., Pandis, S. N. and Lelieveld, J.: Global combustion sources of organic aerosols: Model comparison with 84 AMS factor-analysis data sets, *Atmos. Chem. Phys.*, 16(14), 8939–8962, doi:10.5194/acp-16-8939-2016, 2016.
- Ullmann, D. A., Hinks, M. L., Maclean, A. M., Butenhoff, C. L., Grayson, J. W., Barsanti, K., Jimenez, J. L., Nizkorodov, S. A., Kamal, S. and Bertram, A. K.: Viscosities, diffusion coefficients, and mixing times of intrinsic fluorescent organic molecules in brown limonene secondary organic aerosol and tests of the Stokes–Einstein equation, *Atmos. Chem. Phys.*, 19(3), 1491–1503, doi:10.5194/acp-19-1491-2019, 2019.
- Vargaftik, N. B., Volkov, B. N. and Voljak, L. D.: International Tables of the Surface Tension of Water, *J. Phys. Chem. Ref. Data*, 12(3), 817–820, doi:10.1063/1.555688, 1983.
- Varutbangkul, V., Brechtel, F. J., Bahreini, R., Ng, N. L., Keywood, M. D., Kroll, J. H., Flagan, R. C., Seinfeld, J. H., Lee, A. and Goldstein, A. H.: Hygroscopicity of secondary organic aerosols formed by oxidation of cycloalkenes, monoterpenes, sesquiterpenes, and related compounds, *Atmos. Chem. Phys.*, 6(9), 2367–2388, doi:10.5194/acp-6-2367-2006, 2006.
- Virtanen, A., Joutsensaari, J., Koop, T., Kannosto, J., Yli-Pirilä, P., Leskinen, J., Mäkelä, J. M.,

- Holopainen, J. K., Pöschl, U., Kulmala, M., Worsnop, D. R. and Laaksonen, A.: An amorphous solid state of biogenic secondary organic aerosol particles, *Nature*, 467(7317), 824–827, doi:10.1038/nature09455, 2010.
- Viswanath, D. S., Ghosh, T. K., Prasad, D. H. L., Dutt, N. V. K. and Rani, K. Y.: *Viscosity of Liquids: Theory, Estimation, Experiment, and Data*, Springer, Dordrecht., 2007.
- Wagner, N. L., Brock, C. A., Angevine, W. M., Beyersdorf, A., Campuzano-Jost, P., Day, D., de Gouw, J. A., Diskin, G. S., Gordon, T. D., Graus, M. G., Holloway, J. S., Huey, G., Jimenez, J. L., Lack, D. A., Liao, J., Liu, X., Markovic, M. Z., Middlebrook, A. M., Mikoviny, T., Peischl, J., Perring, A. E., Richardson, M. S., Ryerson, T. B., Schwarz, J. P., Warneke, C., Welti, A., Wisthaler, A., Ziemba, L. D. and Murphy, D. M.: In situ vertical profiles of aerosol extinction, mass, and composition over the southeast United States during SENEX and SEAC 4 RS: observations of a modest aerosol enhancement aloft, *Atmos. Chem. Phys.*, 15, 7085–7102, doi:10.5194/acp-15-7085-2015, 2015.
- Wagner, R., Möhler, O., Saathoff, H., Schnaiter, M., Skrotzki, J., Leisner, T., Wilson, T. W., Malkin, T. L. and Murray, B. J.: Ice cloud processing of ultra-viscous/glassy aerosol particles leads to enhanced ice nucleation ability, *Atmos. Chem. Phys.*, 12(18), 8589–8610, doi:10.5194/acp-12-8589-2012, 2012.
- Wallace, J. M. and Hobbs, P. V.: *Atmospheric Science: An Introductory Survey*, Academic Press, Burlington, MA., 2006.
- Wang, B., Lambe, A. T., Massoli, P., Onasch, T. B., Davidovits, P., Worsnop, D. R. and Knopf, D. A.: The deposition ice nucleation and immersion freezing potential of amorphous secondary organic aerosol: Pathways for ice and mixed-phase cloud formation, *J. Geophys. Res.*, 117, doi:10.1029/2012jd018063, 2012.
- Watanabe, K. and Udagawa, H.: Drag reduction of polymer solutions in a pipe with a highly water-repellent wall, *J. Fluid Mech.*, 381, 225–238, 1999.
- Weinzierl, B., Ansmann, A., Prospero, J. M., Althausen, D., Benker, N., Chouza, F., Dollner, M., Farrell, D., Fomba, W. K., Freudenthaler, V., Gasteiger, J., Groß, S., Haorig, M., Heinold, B., Kandler, K., Kristensen, T. B., Mayol-Bracero, O. L., Müller, T., Reitebuch, O., Sauer, D., Schäfler, A., Schepanski, K., Spanu, A., Tegen, I., Toledano, C. and Walser, A.: The Saharan aerosol long-range transport and aerosol-cloud-interaction experiment: Overview and selected highlights, *Bull. Am. Meteorol. Soc.*, 98(7), 1427–1451, doi:10.1175/BAMS-D-15-00142.1, 2017.
- Wilson, J., Imre, D., Beránek, J., Shrivastava, M. and Zelenyuk, A.: Evaporation kinetics of laboratory-generated secondary organic aerosols at elevated relative humidity, *Environ. Sci. Technol.*, 49(1), 243–249, doi:10.1021/es505331d, 2015.
- Wolf, M. J., Coe, A., Dove, L. A., Zawadowicz, M. A., Dooley, K., Biller, S. J., Zhang, Y., Chisholm, S. W. and Cziczo, D. J.: Investigating the Heterogeneous Ice Nucleation of Sea Spray Aerosols Using *Prochlorococcus* as a Model Source of Marine Organic Matter, *Environ. Sci. Technol.*, 53(3), 1139–1149, doi:10.1021/acs.est.8b05150, 2019.
- Ye, Q., Robinson, E. S., Ding, X., Ye, P., Sullivan, R. C. and Donahue, N. M.: Mixing of secondary organic aerosols versus relative humidity, *Proc. Natl. Acad. Sci.*, 113(45), 12649–12654, doi:10.1073/pnas.1604536113, 2016.
- Ye, Q., Upshur, M. A., Robinson, S., Geiger, F. M., Sullivan, R. C., Regan, J., Donahue, N. M., Ye, Q., Upshur, M. A., Robinson, E. S., Geiger, F. M., Sullivan, R. C., Thomson, R. J. and Donahue, N. M.: Following Particle-Particle Mixing in Atmospheric Secondary Organic Aerosols by Using Isotopically Labeled Terpenes Following Particle-Particle Mixing in

- Atmospheric Secondary Organic Aerosols by Using Isotopically Labeled Terpenes, *Chem*, 4(2), 318–333, doi:10.1016/j.chempr.2017.12.008, 2018.
- Yee, L. D., Isaacman-VanWertz, G., Wernis, R. A., Meng, M., Rivera, V., Kreisberg, N. M., Hering, S. V., Bering, M. S., Glasius, M., Upshur, M. A., Gray Bé, A., Thomson, R. J., Geiger, F. M., Offenberg, J. H., Lewandowski, M., Kourtchev, I., Kalberer, M., de Sá, S., Martin, S. T., Alexander, M. L., Palm, B. B., Hu, W., Campuzano-Jost, P., Day, D. A., Jimenez, J. L., Liu, Y., McKinney, K. A., Artaxo, P., Viegas, J., Manzi, A., Oliveira, M. B., de Souza, R., Machado, L. A. T., Longo, K. and Goldstein, A. H.: Observations of sesquiterpenes and their oxidation products in central Amazonia during the wet and dry seasons, *Atmos. Chem. Phys.*, 18(14), 10433–10457, doi:10.5194/acp-18-10433-2018, 2018.
- Ying, Q., Li, J. and Kota, S. H.: Significant Contributions of Isoprene to Summertime Secondary Organic Aerosol in Eastern United States, *Environ. Sci. Technol.*, 49(13), 7834–7842, doi:10.1021/acs.est.5b02514, 2015.
- Yli-Juuti, T., Pajunoja, A., Tikkanen, O. P., Buchholz, A., Faiola, C., Väisänen, O., Hao, L., Kari, E., Peräkylä, O., Garmash, O., Shiraiwa, M., Ehn, M., Lehtinen, K. and Virtanen, A.: Factors controlling the evaporation of secondary organic aerosol from α -pinene ozonolysis, *Geophys. Res. Lett.*, 44(5), 2562–2570, doi:10.1002/2016GL072364, 2017.
- Yonghui Shu and Atkinson, R.: Atmospheric lifetimes and fates of a series of sesquiterpenes, *J. Geophys. Res.*, 100(D4), 7275–7281, doi:10.1029/95JD00368, 1995.
- Zaveri, R. A., Easter, R. C., Shilling, J. E. and Seinfeld, J. H.: Modeling kinetic partitioning of secondary organic aerosol and size distribution dynamics: representing effects of volatility, phase state, and particle-phase reaction, *Atmos. Chem. Phys.*, 14(10), 5153–5181, doi:10.5194/acp-14-5153-2014, 2014.
- Zelenyuk, A., Imre, D., Beránek, J., Abramson, E., Wilson, J. and Shrivastava, M.: Synergy between secondary organic aerosols and long-range transport of polycyclic aromatic hydrocarbons, *Environ. Sci. Technol.*, 46(22), 12459–12466, doi:10.1021/es302743z, 2012.
- Zhang, Y., Sanchez, M. S., Douet, C., Wang, Y., Bateman, A. P., Gong, Z., Kuwata, M., Renbaum-Wolff, L., Sato, B. B., Liu, P. F., Bertram, A. K., Geiger, F. M. and Martin, S. T.: Changing shapes and implied viscosities of suspended submicron particles, *Atmos. Chem. Phys.*, 15(14), 7819–7829, doi:10.5194/acp-15-7819-2015, 2015.
- Zhang, Y., Chen, Y., Lei, Z., Olson, N. E., Riva, M., Koss, A. R., Zhang, Z., Gold, A., Jayne, J. T., Worsnop, D. R., Onasch, T. B., Kroll, J. H., Turpin, B. J., Ault, A. P. and Surratt, J. D.: Joint Impacts of Acidity and Viscosity on the Formation of Secondary Organic Aerosol from Isoprene Epoxydiols (IEPOX) in Phase Separated Particles, *ACS Earth Sp. Chem.*, 3(12), 2646–2658, doi:10.1021/acsearthspacechem.9b00209, 2019a.
- Zhang, Y., Nichman, L., Spencer, P., Jung, J. I., Lee, A., Heffernan, B. K., Gold, A., Zhang, Z., Chen, Y., Canagaratna, M. R., Jayne, J. T., Worsnop, D. R., Onasch, T. B., Surratt, J. D., Chandler, D., Davidovits, P. and Kolb, C. E.: The Cooling Rate- And Volatility-Dependent Glass-Forming Properties of Organic Aerosols Measured by Broadband Dielectric Spectroscopy, *Environ. Sci. Technol.*, 53(21), 12366–12378, doi:10.1021/acs.est.9b03317, 2019b.
- Zhao, Y., Wingen, L. M., Perraud, V. and Finlayson-Pitts, B. J.: Phase, composition, and growth mechanism for secondary organic aerosol from the ozonolysis of α -cedrene, *Atmos. Chem. Phys.*, 16(5), 3245–3264, doi:10.5194/acp-16-3245-2016, 2016.
- Zhao, Z., Cao, J., Shen, Z., Xu, B., Zhu, C., Chen, L. W. A., Su, X., Liu, S., Han, Y., Wang, G.

- and Ho, K.: Aerosol particles at a high-altitude site on the Southeast Tibetan Plateau, China: Implications for pollution transport from South Asia, *J. Geophys. Res. Atmos.*, 118(19), 11,360–11,375, doi:10.1002/jgrd.50599, 2013.
- Zhmud, B.: Viscosity Blending Equations, *Lube Mag.*, (121), 22–27, 2014.
- Zhou, S., Shiraiwa, M., McWhinney, R. D., Pöschl, U. and Abbatt, J. P. D.: Kinetic limitations in gas-particle reactions arising from slow diffusion in secondary organic aerosol, *Faraday Discuss.*, 165, 391–406, doi:10.1039/c3fd00030c, 2013.
- Zhou, S., Hwang, B. C. H., Lakey, P. S. J., Zuend, A., Abbatt, J. P. D. and Shiraiwa, M.: Multiphase reactivity of polycyclic aromatic hydrocarbons is driven by phase separation and diffusion limitations, *Proc. Natl. Acad. Sci. U. S. A.*, 116(24), 11658–11663, doi:10.1073/pnas.1902517116, 2019.
- Zhu, L., Attard, P. and Neto, C.: Reconciling slip measurements in symmetric and asymmetric systems, *Langmuir*, 28(20), 7768–7774, doi:10.1021/la301040d, 2012.
- Zobrist, B., Marcolli, C., Pedernera, D. A. and Koop, T.: Do atmospheric aerosols form glasses?, *Atmos. Chem. Phys.*, 8(17), 5221–5244, doi:10.5194/acp-8-5221-2008, 2008.
- Zobrist, B., Soonsin, V., Luo, B. P., Krieger, U. K., Marcolli, C., Peter, T. and Koop, T.: Ultra-slow water diffusion in aqueous sucrose glasses, *Phys. Chem. Chem. Phys.*, 13(8), 3514–3526, doi:10.1039/c0cp01273d, 2011.

Appendices

Appendix A Appendix to Chapter 3

A.1 Calculations of vertical profiles of temperature and RH in the boundary layer above Hyytiälä (boreal forest) and the Amazon (rainforest)

The monthly average afternoon (13:00-15:00, local time) temperature and RH vertical profiles over Hyytiälä and an average of five different stations in the Amazon were calculated for the driest month of the year at these locations. For Hyytiälä, the average afternoon temperatures and RHs at the surface were obtained from the SMEAR II campaign data set for 2012, retrieved from Etsin Research data finder (<https://etsin.avointiede.fi/dataset>) (Aalto, 2012a, 2012b). For the Amazon, the temperature and RH at the surface were obtained from NOAA's National Climate Data Center (<http://www.ncdc.noaa.gov/>) from 2004 to 2014, and an average from five different stations was used (Alfredo Vasquez Cobo, Itaituba, Tabatinga, Monte Dourado and Iauarete).

The vertical profiles of temperature were calculated using a dry adiabatic lapse rate of 9.8 K km⁻¹ and the average afternoon surface temperatures mentioned above. The vertical profiles of RH were calculated using the average afternoon surface RHs mentioned above, the vertical profiles of temperature (calculated with the dry adiabatic lapse rate), and assuming the mixing ratio of water is independent of height in the PBL. For the calculations of RH as a function of altitude, the water vapor pressure and water saturated vapour pressure were needed as a function of altitude. The water vapor pressure as a function of altitude was determined by multiplying the mixing ratio of water by the atmospheric pressure, calculated using the following equation (Seinfeld and Pandis, 2006):

$$P(z) = P_0 \exp\left(-\frac{Mgz}{RT}\right) \quad (\text{Eq. A.1})$$

where P_0 is the standard pressure at sea level (101325 Pa), M is the molecular mass of the air (28.8 g/mol), g is the acceleration due to gravity (9.81 m s⁻²), z is the altitude in metres, R is the ideal gas constant and T is the temperature in Kelvin. The water saturated vapour pressure was calculated as a function of attitude using the Antoine equation (National Institute of Standards and Technology, 2016):

$$\log_{10}(P) = A - \left(\frac{B}{T+C}\right) \quad (\text{Eq. A.2})$$

where P is the pressure in bar, $A=4.6543$, $B=1435.264$, $C=-64.848$ and T is the temperature in Kelvin. The values for A, B and C were based on the NIST values for water, which are valid for temperatures between 256 and 373 K (National Insitute of Standards and Technology, 2016).

In Fig. 3.6, the temperature and RH were plotted until the RH reached 100 %. The height at which RH reached 100 % was only slightly lower than the average height of the planetary boundary layer predicted by GEOS-5 meteorology data for the driest month of the year and for the afternoon (13:00-15:00, local time) above Hyytiälä and the Amazon. For Hyytiälä, 100 % RH was reached at 1605 m, while GEOS-5 predicted an average height of the PBL of 1667 m for this location and time. For the Amazon, 100 % RH was reached at 882 m, while GEOS-5 predicted an average height of the PBL of 1249 m for this location and time. When predicting the height of the PBL using GEOS-5 meteorology, GEOS-Chem was run at a horizontal grid resolution of 2° latitude by 2.5° longitude rather 4° latitude by 5° longitude to provide a better approximation to these single locations.

A.2 Tables and figures

Table A.1: Room-temperature α -pinene SOA viscosity data from Grayson et al. (2016). Viscosity data corresponds to SOA generated with a mass concentration of 520 $\mu\text{g m}^{-3}$.

Reference	Viscosity (Pa s)	RH (%)	Temperature (K)
Grayson et al. (2016) (SOA generated with a mass concentration = 520 $\mu\text{g m}^{-3}$)	^a Range= 4.2×10^2 - 3.1×10^4 , midpoint= 3.6×10^3	50	^c Range=293-295 Midpoint=294
	^a Range= 9.7×10^2 - 7.9×10^4 , midpoint= 8.7×10^3	40	
	^a Range= 3.4×10^3 - 2.1×10^5 , midpoint= 2.6×10^4	30	
	^a Range= 3.5×10^5 - 1.8×10^7 , midpoint= 2.5×10^6	^b 0	

^a Grayson et al. (2016) reported upper and lower limits to the viscosity (i.e. range) at each specified RH. To simplify the fitting procedure, the midpoints of the viscosities from Grayson et al (2016) were used.

^b Grayson et al. (2016) measured the viscosity under dry conditions (RH of < 0.5 % based on measurements). When developing the parameterization, a value of 0 % RH was used.

^c Grayson et al. (2016) carried out experiments at room temperature (293 K-295 K). The midpoint of the temperature (294 K) was used when developing the viscosity parameterization for α -pinene SOA.

Table A.2: Low-temperature α -pinene SOA viscosity data from Järvinen et al. (2016). Viscosity data corresponds to SOA generated with a mass concentration of 707-1414 $\mu\text{g m}^{-3}$.

Reference	Viscosity (Pa s)	RH (%)	Temperature (K)
Järvinen et al. (2016)	1×10^7	^a Range=22.9-36.3, midpoint=29.6	263.3
		^a Range=30.5-37.3, midpoint=33.9	262.9
		^a Range=40.5-46.0, midpoint=43.3	253.3
		^a Range=44.0-49.8, midpoint=46.9	252.9
		^a Range=55.0-63.4, midpoint=59.2	243.3
		^a Range=68.6-80.1, midpoint=74.4	235.5

^a Järvinen et al (2016) reported upper and lower limits to the RH for a specific temperature and viscosity. To simplify fitting, the midpoint of the RH range was used.

Table A.3: Liquid water viscosity data from Crittenden et al. (2012).

Reference	Viscosity (Pa s)	RH (%)	Temperature (K)
Crittenden et al. (2012)	^a 1.002×10^{-3}	100	293
	^a 1.139×10^{-3}		288
	^a 1.307×10^{-3}		283
	^a 1.518×10^{-3}		278
	^a 1.781×10^{-3}		273

^a The viscosity values in Crittenden et al. (2012) were reported to 4 significant digits.

Table A.4: Initial guess parameters and fitting parameters used in Eq. 3.1 to predict the viscosity of α -pinene SOA as a function of temperature and RH. The fitting parameters were obtained by fitting Eq. 3.1 to the viscosity data listed in Tables A.1-A.3.

Parameter	Guess Value	Fitting Value
C_1	19	131
C_2	50 K	1165 K
k_{GT}	2.5	3.934
$T_{g,SOA}$	250 K	236.8 K

Table A.5: Literature viscosity data used to create a parameterization for the viscosity of sucrose particles as a function of temperature and RH.

System	Viscosity Range (Pa s)	RH (%)	Temperature (K)	Reference
Water	1.002×10^{-3} to 1.781×10^{-3}	100	275-293	Crittenden et al. (2012)
Sucrose-water	3.19×10^{-3} to 4.82×10^{-1}	96.2-80	293	Swindells et al. (1958)
	6.73×10^{-1} to 1.10×10^3	80-56.6		Quintas et al. (2006)
	1.97×10^{-3} to 5.67×10^{-2}	99.4-88		Perry and Green (2008)
	1.25×10^{-3} to 8.30×10^{-2}	99.99-87.96		Migliori et al. (2007)
	1.26×10^{-3} to 7.65×10^{-2}	99.89-87.98		Telis et al. (2007)
	1.03×10^{-3} to 5.81×10^{-2}	100-87.98		Forst et al. (2002)
	3×10^{-2} to 6.71×10^8	92-28		Power and Reid (2014)
	1×10^{12}	48.53-25.88	255-295 (5 degree increments) ^a	Zobrist et al. (2008)

^a Zobrist et al. (2008) reported glass transition temperatures as a function of water activity for the range of 160 K to 300 K. These glass transition temperatures were based on glass transition temperature measurements in the range of 180 K to 240 K, water activity measurements, and the Gordon-Taylor equation. To develop the parameterization, their glass transition temperatures over the range of 255 K to 295 K from their Fig. 5b were used, recorded in 5 K increments.

Table A.6: Parameters from Zobrist et al. (2011) used in Eq. 3.5 to predict the weight fractions of sucrose and water in particles as a function of relative humidity.

Parameter	Value	Parameter	Value
a	-1	e	-0.005151
b	-0.99721	f	0.009607
c	0.13599	g	-0.006142
d	0.001688	T°	298 K

Table A.7: Fitting parameters used in Eq. 3.1 to predict the viscosity of sucrose particles as a function of temperature and RH. These parameters were obtained by fitting Eq. 3.1 to the viscosity data listed in Table A.6 as well as the guess values in the table.

Parameter	Guess Value	Fitting Value
C_1	19	20.06
C_2	50 K	55.58 K
k_{GT}	4.74	4.531
$T_{g,SOA}$	336 K	324.5 K

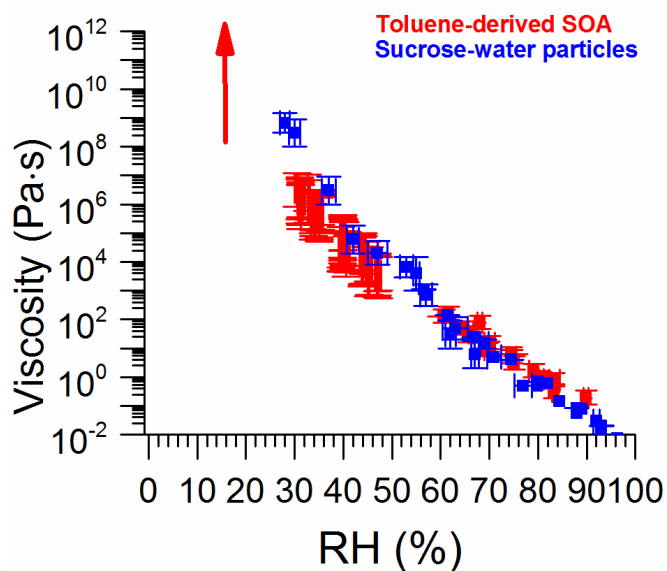


Figure A.1: Viscosities of different proxies of anthropogenic SOA as a function of RH. Data for toluene SOA taken from Song et al. (2016a). The data for sucrose-water mixtures was taken from Swindells (1958), Quintas et al. (2006), Telis et al. (2007), Forst et al. (2002), Migliori et al. (2007), Perry and Green (2008), and Power and Reid (2014).

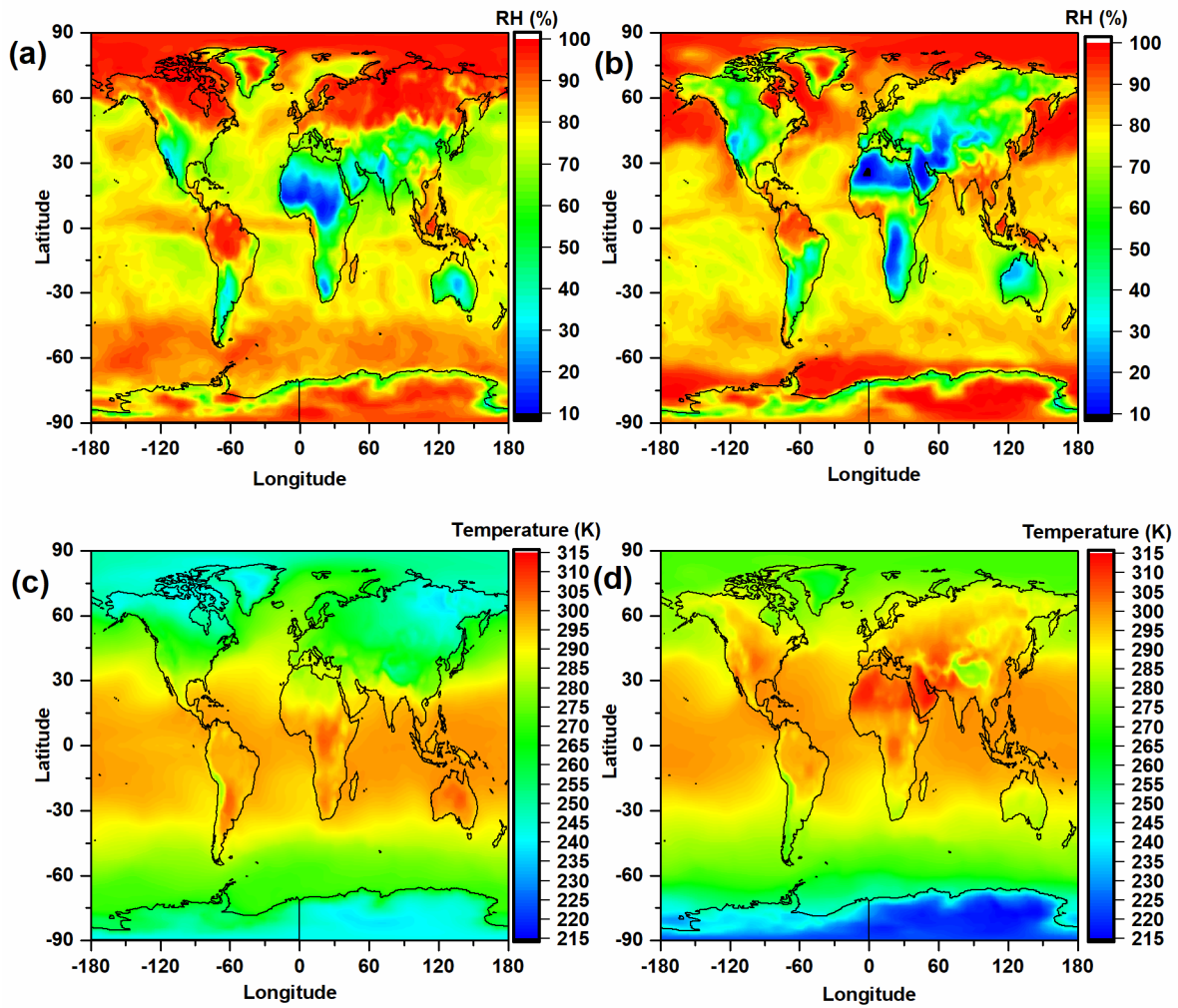


Figure A.2: Monthly average relative humidity and temperature at the surface. Panels A and C correspond to January and panels B and D correspond to July.

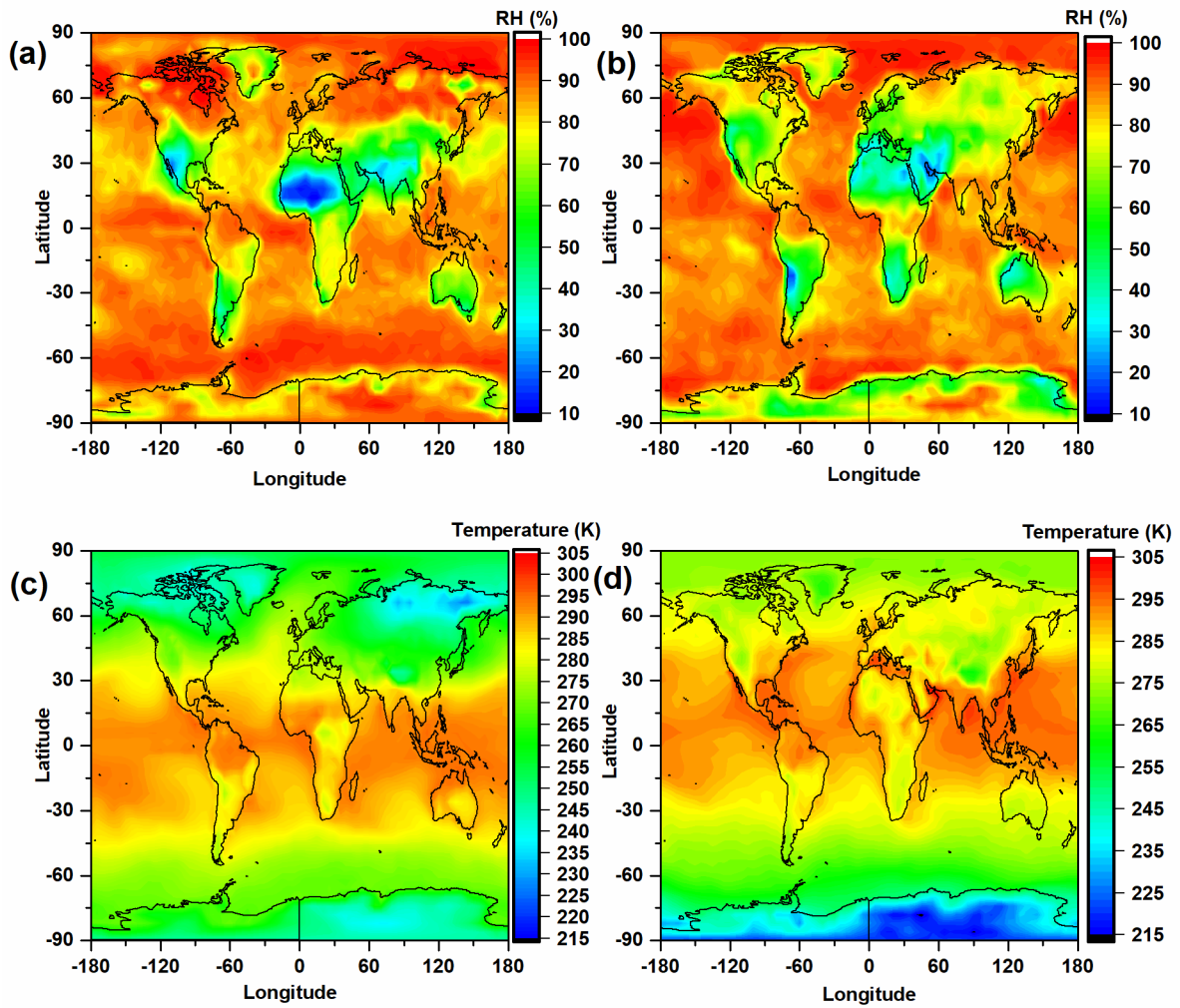


Figure A.3: Monthly average relative humidity and temperature at the top of the planetary boundary layer. Panels A and C correspond to January, and panels B and D correspond to July.

Appendix B Appendix to Chapter 4

B.1 OH reaction rates

Ozonolysis of olefins is known to produce OH as a product of Criegee intermediate decomposition. To minimize the role of OH in oxidizing β -caryophyllene, 2-butanol was used as an OH scavenger (Keywood et al., 2004). A ratio of the reaction rates of OH radicals with 2-butanol and β -caryophyllene were calculated to determine the scavenger efficiency using Eq. B.1:

$$\frac{R_{2-but}}{R_{\beta-car}} = \frac{k_{2-but}[OH][2-but]}{k_{\beta-car}[OH][\beta-car]} \quad (\text{Eq. B.1})$$

where R_{2-but} and $R_{\beta-car}$ are the reaction rates of 2-butanol and β -caryophyllene, respectively, k_{2-but} and $k_{\beta-car}$ are the rate constants for the reaction between OH and 2-butanol or β -caryophyllene, and $[OH]$, $[2-but]$, and $[\beta-car]$ are the concentrations of the OH radicals, 2-butanol and β -caryophyllene, respectively. This equation simplifies to Eq. B.2:

$$\frac{R_{2-but}}{R_{\beta-car}} = \frac{k_{2-but} [2-but]}{k_{\beta-car} [\beta-car]} \quad (\text{Eq. B.2})$$

A rate constant of $1.97 \times 10^{-10} \text{ cm}^3 \text{ molecule}^{-1} \text{ s}^{-1}$ was used for the reaction between β -caryophyllene and OH (Yonghui Shu and Atkinson, 1995). A rate constant of $8.1 \times 10^{-12} \text{ cm}^3 \text{ molecule}^{-1} \text{ s}^{-1}$ was used for the reaction between 2-butanol and OH (Baxley and Wells, 1998). Based on the ratio of 2-butanol to β -caryophyllene used in the environmental chamber experiments, $\frac{R_{2-but}}{R_{\beta-car}}$ is 5.6, indicating that the 2-butanol scavenged ~83% of the OH radicals.

B.2 Mixing times of water within SOA

Characteristic mixing times of water within the SOA (τ_{mix,H_2O}) were calculated using Eq. 1.2. To calculate τ_{mix,H_2O} at each RH, the diffusion coefficient of water in the SOA (D_{H_2O}) was assumed to be the same as D_{H_2O} in sucrose-water particles with an equivalent viscosity. For the viscosity of the SOA, the upper limit of the viscosity values reported in Fig. 4.5 was used. D_{H_2O} was then calculated for the upper limits of the viscosity using the relationship between D_{H_2O} and viscosity for sucrose-water particles developed by Price et al. (2016) (Fig. 7 in Price et al.):

$$D_{H_2O} = C\eta^{-\zeta} \quad (\text{Eq. B.3})$$

where C corresponds to 2×10^{-11} and ζ corresponds to 0.57. The values for $\tau_{mix,H2O}$ determined using this approach are listed in Table B.2.

B.3 Tables and figures

Table B.1: COMSOL parameters used when simulating the viscosity of β -caryophyllene SOA from poke-flow measurements

	Surface tension (mN m ⁻¹)	Slip length (m)	Density (kg m ⁻³)	Contact angle (°)
Range of values	29.7-72.75 ^a	5×10^{-9} - 1×10^{-5} ^b	990 ^c	30-100 ^d
Values for lower limit	29.7	5×10^{-9}	990	30-100
Values for upper limit	72.75	1×10^{-5}	990	30-100

^aLower limit of surface tension is the surface tension of liquid β -caryophyllene based on the model ACD/Labs Percepta Platform-PhysChem Module. Retrieved from Chemspider on May 15, 2019. Upper limit is the surface tension of pure water at 20 °C from Vargaftik et al. (1983). ^bRange is based on measurements of the slip length of organic compounds and water on hydrophobic surfaces.(Baudry et al., 2001; Cheng and Giordano, 2002; Choi and Kim, 2006; Churaev et al., 1984; Craig et al., 2001; Jin et al., 2004; Joly et al., 2006; Joseph and Tabeling, 2005; Li et al., 2014; Neto et al., 2005; Schnell, 1956; Tretheway and Meinhart, 2002; Watanabe and Udagawa, 1999; Zhu et al., 2012) ^cDensity is based on measurements from Tasoglou and Pandis. (2015) ^dContact angle range is based on ranges measured in other chamber generated SOA (Grayson et al., 2016; Song et al., 2015, 2016a). Note: the simulated viscosities depend only weakly on the contact angle. Changing the contact angle by $\pm 10\%$ changes the simulated viscosity on average by $\pm 15\%$, which is small compared to the overall uncertainties associated with the simulated viscosities.

Table B.2: Calculated mixing times of water within the SOA particles ($\tau_{\text{mix,H}_2\text{O}}$) and experimental conditioning time for water vapor ($t_{\text{exp,H}_2\text{O}}$), which corresponds to the time the SOA particles were exposed to a given relative humidity before the poke-flow experiments. Viscosities are based on the upper limits of viscosity shown in Fig. 4.5 of the main text. Diffusion coefficients were calculated using the relation between viscosity and diffusion coefficients in sucrose-water from Price et al. (2016) (Eq. B.3). The variable d_p corresponds to the diameter of the SOA used in the poke-flow experiments.

RH	Upper limit of viscosity (Pa s)	Diffusion coefficient of water ($\text{m}^2 \text{s}^{-1}$)	d_p (μm)	$\tau_{\text{mix,H}_2\text{O}}$ (hrs)	$t_{\text{exp,H}_2\text{O}}$ (hrs)	$t_{\text{exp,H}_2\text{O}}/\tau_{\text{mix,H}_2\text{O}}$
48	2.68×10^5	1.61×10^{-14}	61-91	1.6-3.6	3-5	0.96-2.7
28	1.80×10^6	5.44×10^{-15}	42-69	2.3-6.2	5-24.5	1-10
15	3.60×10^6	3.66×10^{-15}	45-78	3.9-11.8	20	1.8-5.3
0	9.60×10^7	5.64×10^{-16}	30-60	11.5-45	2-22	0.08-1

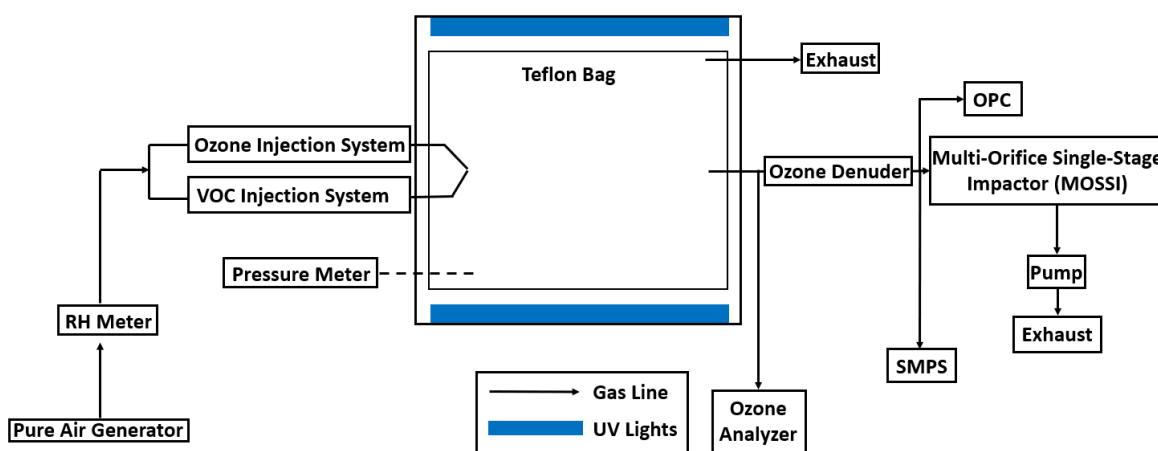


Figure B.1: Schematic diagram of the UBC Environmental Chamber. There are sampling and measurement systems for ozone, temperature, relative humidity, and particle size distribution (scanning mobility particle sizer (SMPS) & optical particle counter (OPC)).

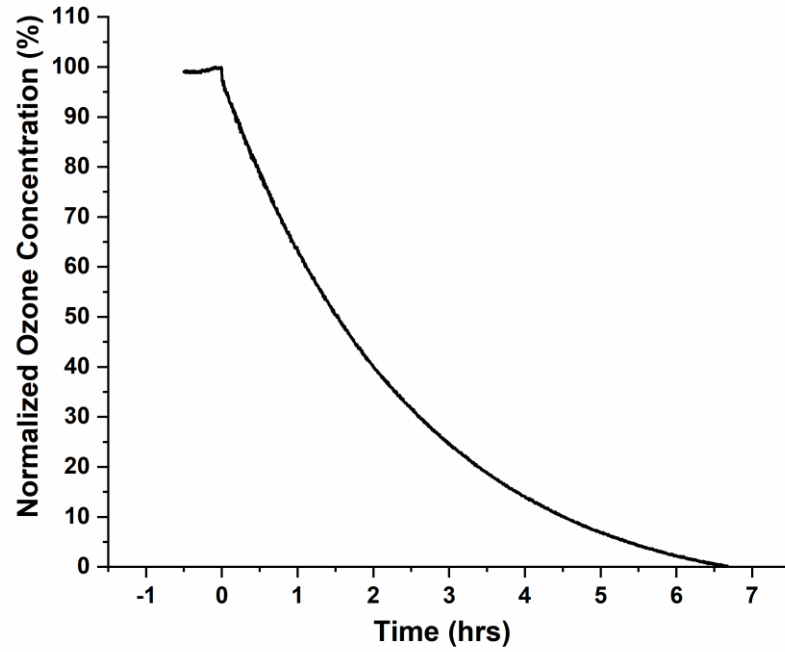


Figure B.2: The change of the ozone concentration inside the chamber with respect to time. Prior to a time of 0 h, the ozone concentration is at a steady state of approximately 325 ppb. At 0 h, the ozone injection is shut off, and the concentration of ozone starts to decrease afterwards. The ozone concentration drops to half of the initial value at approximately 1.5 h.

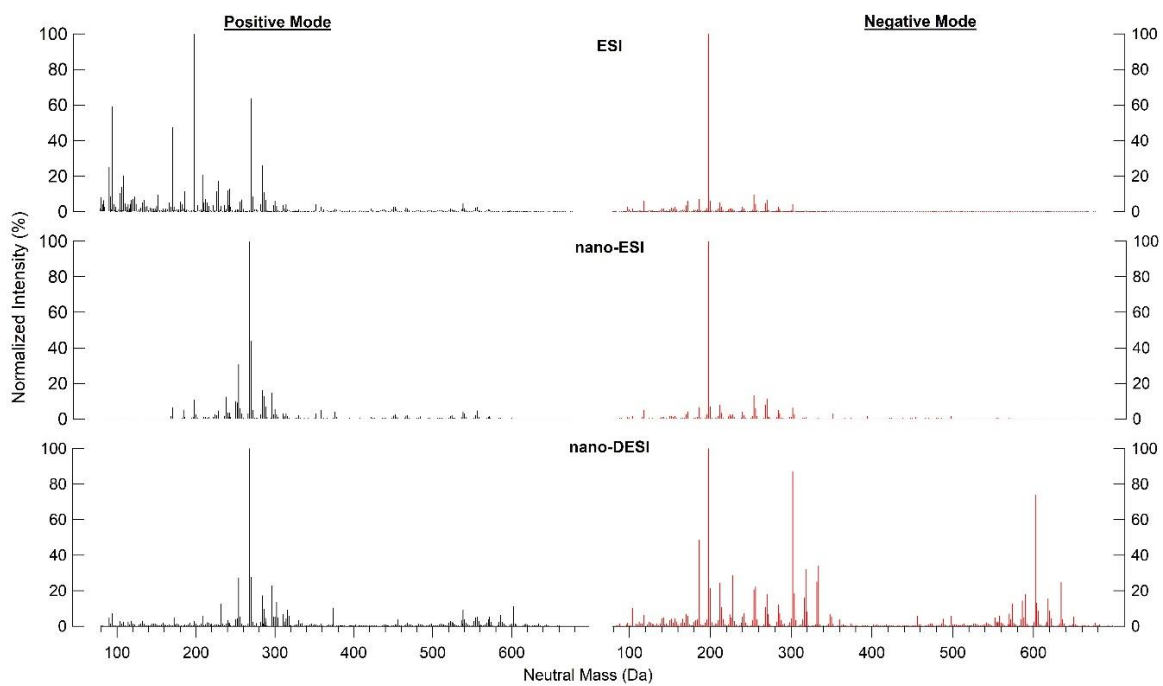


Figure B.3: High-resolution mass spectrometry data taken with ESI, nano-ESI, and nano-DESI ionization sources in both positive and negative mode. The intensities were normalized to the largest peak within each ionization mode.

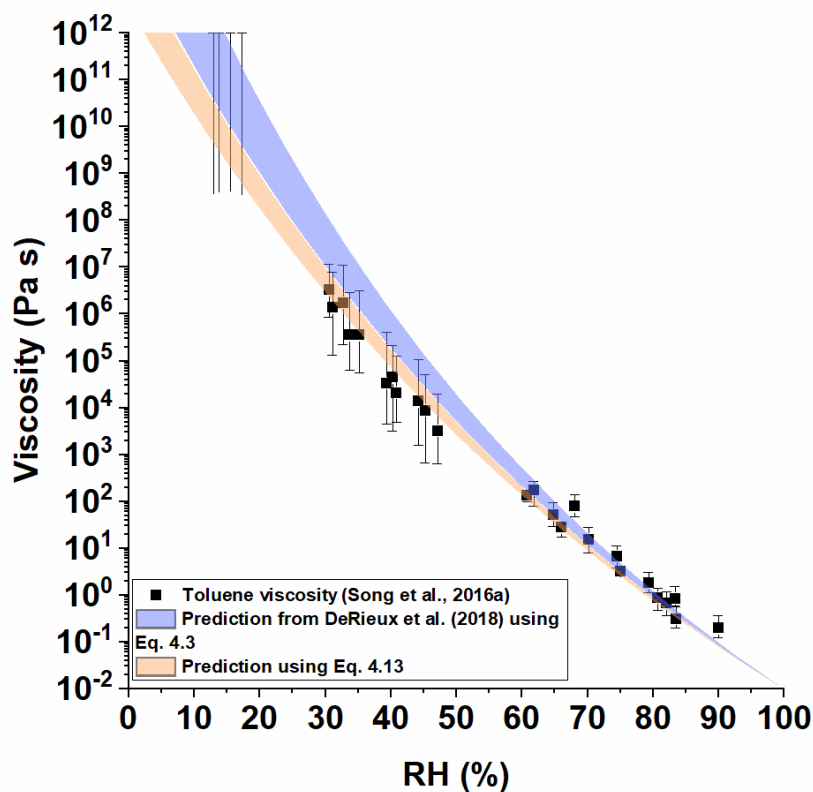


Figure B.4: Toluene SOA viscosity as a function of RH. The y-error bars correspond to the upper and lower limits of viscosity from the measurements. Shown in blue are the viscosity predictions based on nano-DESI positive mode mass spectrometry results from DeRieux et al. (2018) where it was assumed that the weight fraction of individual compounds was proportional to the mass spectrum signal intensity (Eq. 4.3). Shown in orange are the viscosity predictions from DeRieux et al. (2018) where a relation between weight fraction and intensity given in Eq. 4.13 of the main text was assumed. The shaded regions were calculated from nano-DESI mass spectrometry data collected at high and low RH separately (Hinks et al., 2018).

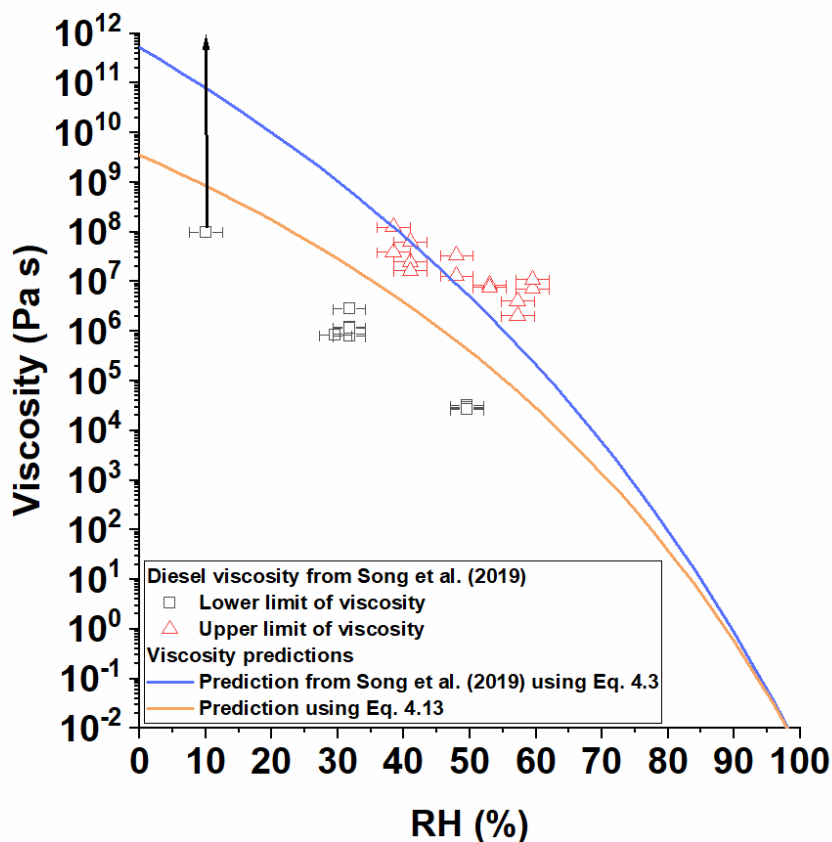


Figure B.5: Diesel fuel vapour SOA viscosities as a function of RH. The x-error bars correspond to uncertainties in the RH measurements and the y-error bars correspond to the upper and lower limits of viscosity at each RH from Song et al. (2019). Shown in blue are the viscosity predictions based on nano-DESI negative mode mass spectrometry results where it was assumed that the weight fraction of individual compounds was proportional to the mass spectrum signal intensity (Eq. 4.3). Shown in orange are the viscosity predictions where a relation between weight fraction and intensity given in Eq. 4.13 was assumed.

Appendix C Appendix to Chapter 5

C.1 Mole fraction-based viscosity mixing rule

The activity based mixing rule is based on the Arrhenius mixing rule:

$$\log(\eta_{mix}) = x_{SOA} \log(\eta_{SOA}) + x_{H_2O} \log(\eta_{H_2O}) \quad (\text{Eq. C.1})$$

where η_{mix} , η_{SOA} and η_{H_2O} are the viscosity of the mixture, SOA and water respectively and x_{SOA} and x_{H_2O} are the mole fraction of the SOA and water. The mole fraction of water and SOA can be calculated from the relative humidity (RH) using the following equation (Koop et al., 2011):

$$a_w = \frac{1}{(1 + i_{SOA} \frac{n_{SOA}}{n_{H_2O}})} \quad (\text{Eq. C.2})$$

where a_w is the activity of water, i is the dimensionless van't Hoff factor and n_{SOA} and n_{H_2O} are the moles of SOA and water, respectively. The mixture was assumed to be an ideal solution with a van't Hoff factor of 1. This allows the equation to be rearranged into the form:

$$a_w = \frac{n_{H_2O}}{(n_{H_2O} + n_{SOA})} \quad (\text{Eq. C.3})$$

The right-hand side of Eq. C.3 is the expression for the mole-fraction of water (x_{H_2O}). The activity of water is defined as $\frac{RH}{100}$, which can be combine with Eq. C.1 to give the final activity based mixing rule:

$$\log(\eta) = (1 - \frac{RH}{100}) \log(\eta_{SOA}) + \frac{RH}{100} \log(\eta_{H_2O}) \quad (\text{Eq. C.4})$$

C.2 Viscosity of water as a function of temperature

The viscosity of water as a function of temperature was determined based on the temperature-dependent viscosities between 311 K and 230 K from Hallett (1963) and Crittenden et al. (2012) (Fig. C.1). The data was fit to the VFT equation with the fragility parameter and Vogel temperature combined into a single constant (B):

$$\log(\eta) = A + \frac{B}{(T - T_0)} \quad (\text{Eq. C.5})$$

where A, B and C are fitting constants. The VFT equation is an empirical model that has been used to fit the temperature dependence of viscosity for a wide variety of compounds (Angell, 1991). The values of [A, B, and T_0] obtained from the fitting were $[-4.28 \pm 0.011, 152.87 \pm 2.21, 173.06 \pm 0.70]$. The fit to the data is shown in Fig. C.1 as a solid line.

C.3 Figures

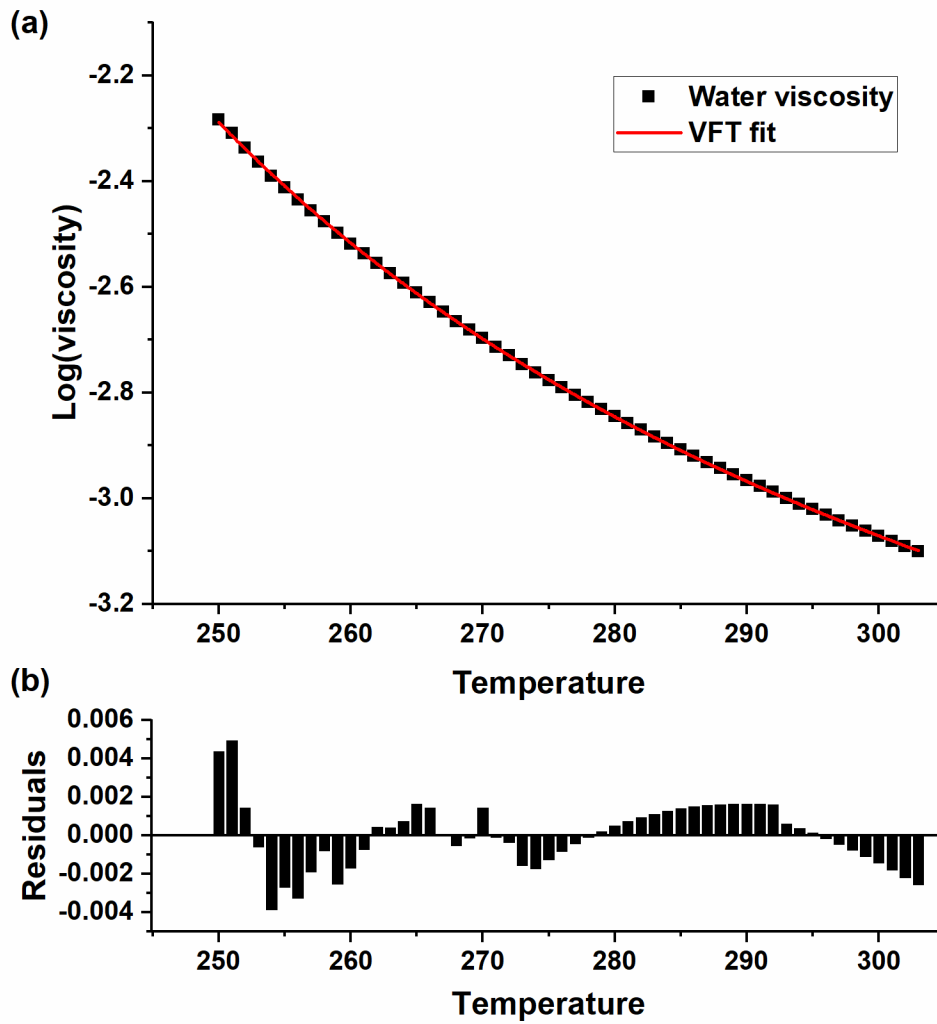


Figure C.1: Viscosity as a function of temperature for water fit using the VFT equation. Panel A shows the measured viscosities of water as a function of temperature from Hallett (1963) and Crittenden et al. (2012) and the red line is a fit to the data using Eq. C.5. Panel B shows the difference between the measured values of viscosity and the predicted values from the VFT equation (residuals).